

<https://doi.org/10.15388/vu.thesis.221>
<https://orcid.org/0000-0003-2418-1507>

VILNIUS UNIVERSITY

Rokas
ASTRAUSKAS

Computer Modelling of Reaction-Diffusion Processes in Scanning Electrochemical Microscopy and in Cell Spheroids

DOCTORAL DISSERTATION

Natural Sciences,
Informatics (N 009)

VILNIUS 2021

This dissertation was written between 2014 and 2018 during PhD studies at Vilnius University.

The dissertation is defended on an external basis.

Academic Consultant:

Prof. Habil. Dr. Feliksas Ivanauskas (Vilnius University, Natural Sciences, Informatics – N 009).

Dissertation Defence Panel:

Chair – **Prof. Dr. Olga Kurasova** (Vilnius University, Natural Sciences, Informatics – N 009).

Members:

Prof. Habil. Dr. Raimondas Čiegis (Vilnius Gediminas Technical University, Natural Sciences, Informatics – N 009).

Prof. Dr. Tadas Meškauskas (Vilnius University, Natural Sciences, Informatics – N 009).

Prof. Habil. Dr. Minvydas Ragulskis (Kaunas University of Technology, Natural Sciences, Informatics – N 009).

Dr. Vitali Sõritski (Tallinn University of Technology, Estonia, Natural Sciences, Chemistry – N 003).

The dissertation shall be defended at a public meeting of the Dissertation Defence Panel at 10 a.m. on 6th October 2021 at the Institute of Computer Science of Vilnius University. Address: Didlaukio str. 47, LT-08303, Vilnius, Lithuania, tel. +370 5 219 5000; e-mail: mif@mif.vu.lt

The text of this dissertation can be accessed at the Library of Vilnius University and on the website of Vilnius University:

www.vu.lt/lt/naujienos/ivykiu-kalendorius.

<https://doi.org/10.15388/vu.thesis.221>
<https://orcid.org/0000-0003-2418-1507>

VILNIAUS UNIVERSITETAS

Rokas
ASTRAUSKAS

Reakcijos-difuzijos procesų
kompiuterinis modeliavimas
elektrocheminėje mikroskopijoje ir
ląstelių sferoiduose

DAKTARO DISERTACIJA

Gamtos mokslai,
informatika (N 009)

VILNIUS 2021

Disertacija rengta 2014 – 2018 metais studijuojant doktorantūroje Vilniaus universitete.

Disertacija ginama eksternu.

Mokslinis konsultantas:

prof. habil. dr. Feliksas Ivanauskas (Vilniaus universitetas, gamtos mokslai, informatika – N 009).

Gynimo taryba:

Pirmininkė – **prof. dr. Olga Kurasova** (Vilniaus universitetas, gamtos mokslai, informatika – N 009).

Nariai:

prof. habil. dr. Raimondas Čiegis (Vilniaus Gedimino technikos universitetas, gamtos mokslai, informatika – N 009).

prof. dr. Tadas Meškauskas (Vilniaus universitetas, gamtos mokslai, informatika – N 009.)

prof. habil. dr. Minvydas Ragulskis (Kauno technologijos universitetas, gamtos mokslai, informatika - N 009).

dr. Vitali Sōritski (Talino technikos universitetas, Estija, gamtos mokslai, chemija – N 003).

Disertacija ginama viešame Gynimo tarybos posėdyje 2021 m. spalio 6 d. 10 val. Vilniaus universiteto Matematikos ir informatikos fakulteto Informatikos instituto 211 auditorijoje. Adresas: Didlaučio g. 47, LT-08303, Vilnius, Lietuva, tel. +370 5 219 5000; el. paštas: mif@mif.vu.lt.

Disertaciją galima peržiūrėti Vilniaus universiteto bibliotekoje ir Vilniaus universiteto interneto svetainėje adresu: www.vu.lt/lt/naujienos/ivykiu-kalendorius.

Table of Contents

Introduction	1
Research area	1
Actuality	2
Aim	3
Methodology	4
Scientific novelty	4
Defended propositions	5
Approbation	6
Structure of Thesis	7
1 Modelling of Scanning Electrochemical Microscopy at Redox Competition Mode Using Diffusion and Reaction Equations	8
1.1 Introduction	8
1.2 Physical model	12
1.3 Mathematical model	15
1.4 Numerical solution	19
1.4.1 Discrete grid and notations	19
1.4.2 ADI Finite difference schemes	24
1.4.3 Numerical algorithms	29
1.4.4 Computation of SECM response	32
1.4.5 Implementation details and algorithm analysis	34
1.5 Modelling and experimental results	35
1.5.1 Comparison of computer simulations and experimental results	35
1.5.2 Calculation of oxygen diffusion coefficient	36
1.6 Summary and conclusions	39
2 Mathematical Modelling of the Influence of Ultramicroelectrode Geometry on Approach Curves Registered by Scanning Electrochemical Microscopy	41
2.1 Introduction	41
2.2 Experimental details	44

2.3	Description of UME geometries and mathematical models	45
2.3.1	Mathematical model for standard-UME	45
2.3.2	Mathematical model for the UME with a recessed conducting part	47
2.3.3	Mathematical model for the UME with an outward-conducting part	47
2.3.4	Mathematical model for the UME with an outward-cone-shaped conducting part	48
2.4	Numerical solution	49
2.4.1	Discrete grid	49
2.4.2	Approximation of the boundary condition on the cone	52
2.4.3	Finite difference schemes	54
2.4.4	Implementation details	57
2.5	Results and Discussion	58
2.5.1	Comparison of experimental data and mathematical modelling results	58
2.5.2	Influence of UME geometry on approach curves	59
2.5.3	Influence of the RG factor on approach curves	64
2.5.4	Analysis of isolines	69
2.5.5	Comparison with data of other studies	70
2.6	Conclusions	72
3	Modelling of Fluorescence Dyes Uptake into 3D Cellular Spheroids	73
3.1	Introduction	73
3.2	Mathematical models	75
3.2.1	WGA migration modelled with reaction-diffusion equations	75
3.2.2	Rhodamine migration modelled with diffusion equation	77
3.2.3	Rhodamine migration using the rings of cells and matrix layers model	78
3.2.4	Calculation of coefficients	78
3.2.5	Numerical solution	80
3.3	Results	82
3.3.1	Analysis of experimental results	82
3.3.2	Comparison between experimental and simulations data for R6G accumulation models	84
3.3.3	Nonlinear WGA model analysis	87
3.4	Conclusions	90
4	Verification of Model Implementation	91

4.1	Theoretical properties of solutions of differential equations	92
4.2	Convergence of numerical solution	96
4.3	Method of a test solution	99
General conclusions		102
Bibliography		104
Santrauka (Summary in Lithuanian)		117
	Tyrimų sritis	117
	Tikslas	118
	Metodai	118
	Naujumas	119
	Ginami teiginiai	120
	Disertacijos struktūra	120
S.1	SECM modeliavimas oksidacijos-redukcijos konkurencijos režime naudojant reakcijos-difuzijos lygtis	120
S.1.1	Fizinis modelis	120
S.1.2	Matematinis modelis	122
S.1.3	Skaitinis sprendimas ir SECM atsakas	124
S.1.4	Modeliavimo ir eksperimento rezultatai	125
S.1.5	Išvados	126
S.2	Elektrodo geometrijos įtakos su SECM matuojamai srovei matematinis modeliavimas	126
S.2.1	Įžanga	126
S.2.2	Elektrodo geometrijos ir jų matematiniai modeliai	127
S.2.3	Skaitinis sprendimas	130
S.2.4	Modeliavimo rezultatai	130
S.2.5	Išvados	133
S.3	Fluorescencinių dažų prasiskverbimo į ląstelių sferoidus modeliavimas	133
S.3.1	Modelių taikymai fiziniuose eksperimentuose	134
S.3.2	Matematiniai modeliai	134
S.3.3	Modeliavimo rezultatai	137
S.3.4	Išvados	139
	Bendros disertacijos išvados	140
Acknowledgements		142
Publications by the Author		143
	Modelling of scanning electrochemical microscopy at redox competition mode using diffusion and reaction equations	143

Mathematical Modelling of the Influence of Ultra-micro Electrode Geometry on Approach Curves Registered by Scanning Electrochemical Microscopy	144
Modeling the uptake of fluorescent molecules into 3D cellular spheroids	145

Introduction

Research area

The study is focused on computer modelling of complex chemical and biophysical systems, which are described by partial differential equations (PDEs) with nonlinear boundary conditions and PDEs in various complex (non-rectangular) domains. These differential problems are solved using numerical methods.

Problems of solving PDEs with nonlinear boundary conditions arise from mathematical modelling of complex chemical and biological processes in scanning electrochemical microscopy (SECM). The study of PDE in non-rectangular domains is motivated by the demand to estimate measurement errors due to deviations of SECM equipment geometry from the standard. Nonlinear systems of PDE are applied in the study of chemotherapeutic drugs uptake into tissues.

Actuality

Scanning electrochemical microscopy is an emerging sensing technique, proposed by Bard et al. in 1989 [12]. SECM is based on electrochemical measurements with the ultramicroelectrode (UME), which is scanning 3D space close to catalytic or electrochemically active surfaces. SECM is applied for high-resolution imaging of the chemical reactivity [144], investigation of electron transfer kinetics [110], biosensors and biochips surfaces [149], etc.

Despite wide and varied applications, practical and theoretical difficulties of SECM-based experiments persist. Common problems are a deviation from idealized geometries of real equipment, poor spatial

resolution, the uncontrolled distance between the UME and surface of interest, expensive experiments, difficulties in manufacturing of equipment, etc. SECM theory such as analytical tools and mathematical modelling methods is applied for dealing with or at least reducing these problems. Computer simulations of SECM are also used for the determination of reaction kinetics [13] and the improvement of experiment techniques [40].

The SECM technique is applied in several modes such as feedback [13] and substrate generation [117], which have also been extensively analyzed by mathematical modelling methods [37, 94]. The novel redox-competition (RC-SECM) mode, which has been proposed by the Schuhmann group in 2006 [45], has been used for the evaluation of enzymatic kinetics in several research papers [82, 99] or combined with other modes [64]. However, the theory of the RC-SECM mode has not been thoroughly investigated. A mathematical model, which simulates both enzymatic reactions on active surface and diffusion processes in the solution, is presented for the first time in this research.

The second part of the thesis is committed to the study of UME geometry and, in particular, the kind of UMEs with non-ideal (non-standard) geometries. The importance of UME geometry has been reported from the early days of SECM research. In one of the earliest paper concerning geometry analysis, published by Kwak and Bard in 1989, the ratio between diameters of an electrode and insulator has been studied and the influence on electric signal has been established using computer simulations [86]. In later studies, various cases of non-ideal electrodes have been modelled: recessed-UME [20], conical UME [150], off-centered-UME [39], nonsymmetrical UME [123]. However, the general method to determine the measurement errors of most frequent non-ideal UMEs is still not well established and will be the focus of this research.

In the third Chapter of the thesis, mathematical models of the reaction-diffusion process of fluorescent dyes are presented. These models are applied in the study of chemotherapeutic drugs uptake into 3D cellular spheroids [46], which has important applications in cancer treatment research. Some authors have published their attempts to simulate how various nanoparticles accumulate and distribute in cellular spheroids [58, 66]. Analytical methods have been applied to analyze fluorescent dye uptake in 3D spheroids [1] and 2D cell cultures [115]. Mathematical models, which would predict diffusion and accumulation of organic molecules (e.g. drugs or dyes) in 3D cell cultures, are presented in this study for the first time.

Aim

The aim of the research falls into two main categories. The first goal was to develop mathematical models of scanning electrochemical microscope and software tools necessary to model reaction-diffusion processes and SECM geometric properties. The second aim was to provide a computational model for the analysis of fluorescent dyes uptake into the spheroidal cell structure. The following tasks were identified:

1. Develop mathematical and numerical models of i) SECM, working in redox-competition mode, ii) SECM with various non-standard ultramicroelectrodes (UME) and iii) fluorescent dye uptake into cell spheroids.
2. Create efficient computer programs for high-precision computations.
3. Achieve the agreement between model and experimental data by calculating model parameters.
4. Calculate reaction kinetic constants and oxygen diffusion coefficients for SECM experiments
5. Develop algorithms to evaluate difference (measurement error) in electric current measured by a standard perfect electrode and by nonideal shaped UMEs.
6. Investigate the properties of fluorescent dyes penetration into cell spheroids depending on cell concentration, the number of binding sites and others.

Methodology

SECM in the redox-competition (RC-SECM) mode is modelled by a system of non-stationary reaction-diffusion equations with nonlinear third type boundary conditions related to the kinetics of enzymatic reactions. SECM geometry is modelled by diffusion equation in non-rectangular geometries. Cellular spheroids are modelled by non-stationary reaction-diffusion equations containing nonlinear terms responsible for reactions between cells and fluorescent dyes.

PDEs in analysed models were solved using numerical methods. Implicit methods were applied in order to achieve lower computational error and higher stability. Alternating direction implicit finite difference method (ADIFDM) was the key algorithm in solving diffusion equations.

Several computer experiments were carried out to achieve goals and compared with real physical experiments. Computer models were developed in Python and MATLAB by the author. Computations were performed using a supercomputer.

Scientific novelty

The main novelties of the thesis are formulated:

1. A novel mathematical model is proposed for SECM acting in the redox-competition mode. The main originality of this model is the combination of diffusion-based models of SECM with reaction equations using nonlinear third type boundary conditions.
2. The study of nonstandard electrodes in SECM-based experiments has allowed to evaluate measurement errors between experiments performed by nonideal UMEs compared to standard perfect UME. Research into the impact of equipment for SECM measurements is an emerging field, but for the first time a comprehensive study of the effects of most common geometry deviations has been provided.
3. The efficient non-uniform meshing method is proposed for SECM models in rectangular and non-rectangular geometries.
4. The uptake of fluorescent dyes into cellular spheroids is modelled for the first time. The main novelties are computation of unknown dye parameters and successful validation of models by physical experiment.

Defended propositions

1. Proposed computer models are effective tools for simulating the behaviour of analyzed systems, i.e. RC-SECM mode, SECM with different UME geometries and the uptake of fluorescent dyes.

2. The correctness of each model is confirmed by
 - (a) achieving high correspondence between modelling and experimental data;
 - (b) verifying implementations of numerical algorithms, which are used for solving models, by various verification methods.
3. Implemented numerical algorithms are highly accurate (2nd order), unconditionally stable and reduce the problem into linear systems, which is solved by efficient linear time solver (Thomas algorithm).
4. In the RC-SECM mode oxygen diffusion coefficient is inversely proportional to the concentration of medium components such as glucose.
5. The largest measurement errors compared to standard UME are made by an outwarded electrode and the difference is lower for recessed and cone-shaped electrodes. Additionally, these errors decrease as the ratio between isolator and electrode radiuses increases.

Approbation

Periodic Publications

The results were published in periodic journals with a citation index. The contribution of the author of the thesis is the development of numerical models and the software for the modelling task, calculations for the models, a validation, analysis and written description of the results.

1. Ivanauskas, F., Morkvenaite-Vilkonciene, I., Astrauskas, R. and Ramanavicius, A. (2016). Modelling of scanning electrochemical microscopy at redox competition mode using diffusion and reaction equations. *Electrochimica Acta*, 222, p. 347-354. DOI: 10.1016/j.electacta.2016.10.179.
2. Astrauskas, R., Ivanauskas, F., Morkvenaite-Vilkonciene, I., and Ramanavicius, A. (2019). Mathematical Modelling of the Influence of Ultra-micro Electrode Geometry on Approach Curves Registered by Scanning Electrochemical Microscopy. *Electroanalysis*, 31(11), p. 2214-2223. DOI: 10.1002/elan.201900313.

3. Astrauskas, R., Ivanauskas, F., Jarockytė, G., Karabanovas, V., and Rotomskis, R. (2019). Modeling the uptake of fluorescent molecules into 3D cellular spheroids. *Nonlinear Analysis: Modelling and Control*, 24(5), p. 838-852. DOI: 10.15388/NA.2019.5.9.

Conferences

1. 22nd International Conference Mathematical Modelling and Analysis (MMA2017), 30 May – 2 June 2017, Druskininkai, Lithuania: Modelling of Scanning Electrochemical Microscopy Using Diffusion and Reaction Equations.
2. 10th Conference on Applied Mathematics and Scientific Computing (ApplMath20), 14 – 18 September 2020, Brijuni, Croatia (online): Modelling of Scanning Electrochemical Microscope and the Influence of Electrode Geometry.
3. Lietuvos matematikų draugijos 57-oji konferencija, 2016 m. birželio mėn. 20–21 d., Vilnius: Mathematical Modelling of Diffusion and Reaction Processes in Scanning Electrochemical Microscopy.
4. Lietuvos matematikų draugijos 59-oji konferencija, 2018 m. birželio mėn. 18–19 d., Kaunas: Analysis of Electrode Geometry effects on Approach Curves Registered by Scanning Electrochemical Microscopy.
5. Lietuvos matematikų draugijos 60-oji konferencija, 2019 m. birželio mėn. 19–20 d., Vilnius: Modelling of Fluorescence Dyes Uptake into Cellular Spheroids.
6. 6-oji LMA jaunųjų mokslininkų konferencija „Fizinių ir technologijos mokslų tarpdalykiniai tyrimai“, 2016 m. vasario mėn. 10 d., Vilnius: Mathematical Modelling of Diffusion-Reaction Equations in Scanning Electrochemical Microscopy.

Structure of Thesis

The thesis consists of the following parts: general introduction, four chapters, conclusions and a list of references.

In Chapter 1, the SECM model, governed by the system of 8 nonlinear reaction-diffusion equations, is presented. The system is solved by

implicit finite difference methods. The numerical solution is compared with the results of a physical experiment, and by fitting modelling data to the experiment, reaction coefficients and diffusion parameters are calculated.

SECM models in 4 geometries (1 standard from Chapter 1 and 3 non-standard) are proposed in Chapter 2. PDEs, representing UMEs in these geometries, are solved and numerical experiment results of one non-standard geometry are compared with a physical experiment to show good correspondence. Then, the difference between standard geometry and non-standard geometries is calculated and the influence of other SECM geometry parameters on approach curves is investigated.

In Chapter 3, the uptake of fluorescent dyes into 3D cell cultures is modelled by reaction-diffusion equations which are solved numerically. Models are applied to analyse two types of dyes and geometrical properties of cell spheroids. Comparison between a numerical and biological experiment is provided. The diffusion coefficient in intercellular medium and time of saturation by dyes are calculated using provided models.

Various methods of model verification are analyzed in the final Chapter 4 in order to test the implementation of numerical algorithms.

Chapter 1

Modelling of Scanning Electrochemical Microscopy at Redox Competition Mode Using Diffusion and Reaction Equations

1.1 Introduction

In the first chapter, the mathematical model of scanning electrochemical microscopy (SECM) redox-competition (RC-SECM) mode is presented for the first time in scientific research. The study is focused on solving systems of partial differential equations (PDEs) with nonlinear boundary conditions using numerical methods. Using this model, it is possible to calculate oxygen consumption rate, evaluate enzymatic reaction kinetics and determine oxygen diffusion coefficients in the medium of varying composition. Oxygen concentration measurement, which is important for SECM-based investigations of all biological systems, was successfully applied for the evaluation of enzymatic reaction performed by an immobilized enzyme.

Scanning electrochemical microscopy

Scanning electrochemical microscopy is an advanced electrochemical method, which is based on electrochemical measurements with the scanning ultramicroelectrode (UME). In this approach, the UME, which has the diameter of conducting part in the range of several tenths of micrometres and insulator part of few hundreds of micrometres, is scanning 3D space close to catalytic or electrochemically active surfaces [12]. In such an experiment the UME is connected as a working electrode in an electrochemical cell, and the current, which is measured by the UME, depends on the local concentration of electroactive species. Electron transfer kinetics of surfaces modified by enzymes is mostly investigated using feedback (FB) or generation-collection modes of SECM [49, 100, 110, 143]. In addition, SECM was applied for high-resolution imaging of the chemical reactivity [131, 144], electrocatalytic activity [54, 68, 147], and topography of enzyme-based interfaces formed in enzyme immunoassays [146], biosensors and biochips [149].

The redox-competition (RC-SECM) mode, which has been developed by the Schuhmann group [45], has been used for the evaluation of enzymatic kinetics in several studies. According to the described mode, dissolved oxygen is consumed in two competing ways: one is based on the electrochemical reaction running on the UME and the other on the reaction catalyzed by an immobilized enzyme, e.g. glucose oxidase (GOx), which is utilizing O₂ as an electron acceptor. In this mode, both (i) GOx immobilized on the non-conducting surface and (ii) the UME acting at a negative potential are competing for dissolved oxygen [99], differently to the previously addressed bi-potentiostatic RC-SECM mode, in which conductive surface has been connected as a second working electrode [68, 82]. At higher glucose concentrations low oxygen concentration region was formed close to the enzyme-modified surface due to the fast enzymatic reaction. Additionally to RC-SECM-based 3D visualization of concentrations of redox-active materials, which are close to the electroactive surface, in the RC-SECM mode current vs distance dependencies can be used to determine enzymatic kinetics [99].

However, according to the of best of our knowledge, analytical expressions for the determination of enzymatic kinetics in the RC-SECM mode are still not well established.

Modelling of biosensors

SECM is a versatile technique, which can be used as a tool in the broader area of biosensor research and development. Mathematical modelling of biosensors is motivated by the complexity of physical, chemical or biological experiments, high measurement errors of these experiments, theoretical interests, etc. Various types of biosensors was modelled in recent scientific literature: amperometric [7, 16, 17, 92, 119, 148], magnetic [97, 102, 103], electrochemical [24, 41, 80, 111], bioluminescent bacteria-based [114, 122], etc. In the majority of those studies, models were described by PDEs or systems of PDEs, which were typically solved numerically by finite difference methods [7, 122] or finite element methods with specialized software such as COMSOL [80, 129]. Extensive studies of biosensors and their computer simulations were presented in monographs/books by Baronas et al. [19], Bartlett et al. [21].

Mathematical models of biosensors, in which the enzyme had been immobilized on the electrode, was widely investigated in various studies. A 2D mathematical model of amperometric biosensors with perforated and selective membranes, based on the diffusion equations containing a nonlinear case of the Michaelis–Menten enzymatic reaction was developed [14, 15, 18, 28]. The numerical simulations were carried out by solving PDEs using finite difference methods [19]. It was also determined, that the modelling of a reaction-diffusion system within a thin layer of an enzyme and containing a nonlinear term of the Michaelis–Menten enzymatic reaction, requires iterative methods such as Newton iteration to solve nonlinear PDEs [28].

Mathematical modelling of SECM

Computer simulations were performed for different modes of SECM: (i) negative/positive feedback [3, 13, 86, 120], (ii) substrate generation/tip collection [93, 117], (iii) disk generation/ring collection [90]. Different purposes can be identified: (i) the determination of reaction kinetics, such as reaction rate constants [13, 110, 123], (ii) the investigation of the influence of UME geometry to the SECM response [3], (iii) the improvement of experiment techniques [40]. Furthermore, simulations can solve important problems, such as poor spatial resolution, the negative effect of uncontrolled distance between the UME and surface of interest during SECM investigations, and the effects of deviations from mathematically idealized SECM geometries [123, 125]. An in-depth overview of SECM

experimental and theoretical topics, including models and numerical solutions, was provided in the book by Bard and Mirkin [11].

Mathematical models of SECM were calculated by: (i) the finite difference method (FDM) [3, 13, 93]; (ii) the finite element method, which was used by [105, 106]; (iii) the boundary element method (BEM) [112, 124, 125]. The influence of electrode geometry for SECM simulations was shown by various authors [3, 37, 124]. The first comprehensive paper concerning the application of the alternating-direction implicit (ADI) FDM (the main method used in the Thesis) to microelectrodes was published by Heinze et al. [70].

Comparison with other studies of reaction kinetics

The first research paper concerning the modelling of SECM reaction kinetics was published by Bard et al. [13]. The SECM feedback mode and finite electron-transfer kinetics with a single reaction, which occurred at the conducting surface, was used in simulations. In another study by Bard et al. [110] a full reaction system was considered, but the model was reduced to a single dimension and the mechanism of reactions was simplified by employing Michaelis–Mentens kinetics. However, both these papers established methods for the calculation of reaction kinetics in the SECM feedback mode.

In more recent papers by Cornut and Lefrou [37, 38] reactions kinetics in the SECM feedback mode were modelled using simplified single reaction based on irreversible or Michaelis–Mentens kinetics mechanism. Analytical expressions for electric current i_T was established depending on UME parameters and reactions kinetics, but the kinetics was simplified and rather theoretical.

However, none of these research papers has taken into account the full reaction-diffusion system, which consists of at least 8 equations in oxygen and glucose oxidase-based experiments. Moreover, these studies deal with the modelling of the type of biosensors in which the enzyme is immobilized on the electrode surface, and the response of the biosensor has been measured by registration of amperometric response with the same electrode. Unlike all mentioned studies, in this research, the enzyme is immobilized on a non-conducting surface in the RC-SECM mode evaluation, and the SECM electrode is always at a distance from an immobilized enzyme-based layer. Therefore, diffusion in confined space, which is limited by edges of the insulating part of the UME, has

to be modelled and a new model is proposed in this research to take into account these conditions.

Outline of the chapter

In section 1.2, a physical model is presented including chemical reactions on enzyme-modified surface and determination of coefficients. A mathematical model is provided in section 1.3 and a numerical algorithm is presented in section 1.4. The results of the research are analysed in section 1.5 and the chapter is summarized in section 1.6.

1.2 Physical model

SECM in redox-competition mode

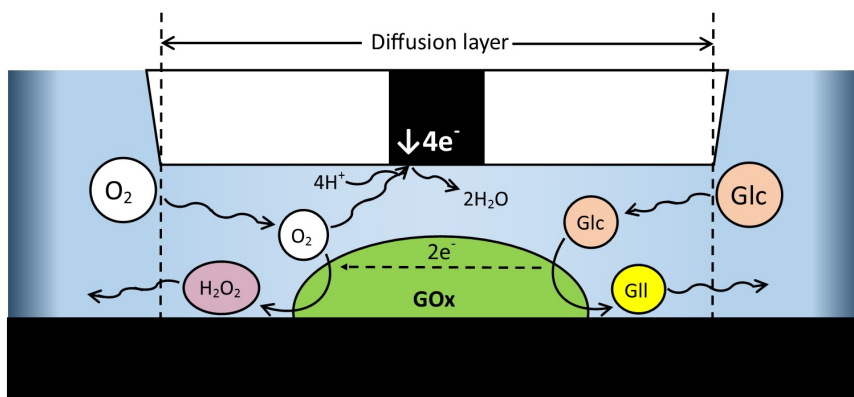
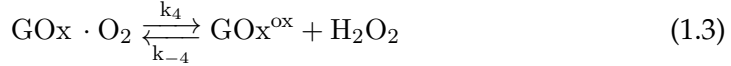
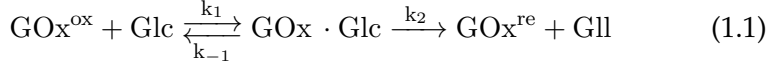


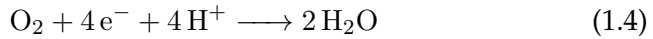
Figure 1.1: Schematics of SECM measurement in reduction-oxidation (redox) competition mode. Oxygen is consumed in two ways: (i) by glucose oxidase (GOx) catalyzed reaction and (ii) in electrochemical reaction on the UME surface as the oxygen in the presence of H^+ is converted to H_2O_2 . Glc — glucose, Gll — gluconolactone.

During a SECM-based experiment, Oxygen (O_2) and glucose (Glc) are dissolved in water solution (Fig. 1.1). Fixed concentrations of O_2 and Glc are provided from external solution, called the bulk, which is usually a petri plate. The process of Glc oxidation starts in the presence

of dissolved O_2 then catalyzed by glucose oxidase (GOx), which is immobilized on the surface. During this process O_2 and Glc are consumed, hydrogen peroxide (H_2O_2) and gluconolactone (Gll) are produced according to equations



The value of UME current depends on the concentration of dissolved oxygen and presence of all other electrochemically active species in the close proximity to the UME surface and on the electric potential applied to the UME. In the evaluated RC-SECM measurement system (Fig. 1.1), oxygen is consumed in two ways: (i) in the redox reaction occurring on the UME surface



and (ii) in enzymatic reaction, where oxygen serves as an electron acceptor, which is taking electrons from GOx in the way presented by (1.1) and is passing them to oxygen in (1.2)–(1.3).

The redox-competition mode was used in order to register O_2 reduction current at negative UME potential. Under such conditions O_2 is reduced into the water on the UME surface according to the reaction (1.4). The mathematical model, which describes the SECM acting in redox-competition mode, was created taking into account conditions presented in Fig. 1.1. The diffusion layer was formed in a confined space between the UME and the surface with immobilized GOx. Both oxygen and glucose diffuse from the bulk to the diffusion layer, as it is shown in Fig. 1.1. Reaction products H_2O_2 and gluconolactone (Gll), formed during catalytic action of GOx, diffuse from the diffusion layer to the external solution.

At the UME surface electrons are transferred to oxygen, which is reduced in the presence of H^+ . Oxygen is also consumed on the surface modified by GOx. Electric current, registered by SECM, decreases due to the competing consumption of oxygen by both UME and GOx-modified surface. Oxygen concentration in the bulk, i.e. external solution, of the electrochemical cell is $253 \mu\text{mol/L}$ and it is considered that this amount does not change during the experiment due to the large size of the bulk.

Reaction rate constants

Proper selection of reaction rate constants is an important issue for the modelling of enzymatic reactions-based processes. Mathematical models of bioreactors, where reactions kinetics had to be calculated, were presented in 1D [42, 81] and 2D [79, 133] geometries. Mathematical models in 3D, which are incorporating convection, diffusion and enzymatic reactions were developed to simulate the concentration of dissolved oxygen inside the microchannels [137].

In this research, the kinetic constants for reactions (1.1)–(1.3) were gathered from references [27, 61, 89] and adjusted to better fit experimental results (Table 1.1). Kinetic constants k_{-1} , k_{-3} , k_{-4} for reactions (1.1)–(1.3) were determined from the model and were set to the following values: $k_{-1} = 10 \text{ s}^{-1}$, $k_{-3} = 2000 \text{ M}^{-1}\text{s}^{-1}$. The constant k_{-4} was set to zero, because the backward reaction (1.3) is much slower than other reactions in diffusion-related processes.

Table 1.1: Kinetic constants and thermodynamic parameters for the GOx catalyzed reaction with β -D-glucose and oxygen at pH 5.5.

Sugar substrate or thermodynamic parameter	k_1 , $\text{M}^{-1}\text{s}^{-1}$	k_2 , s^{-1}	k_3 , $\text{M}^{-1}\text{s}^{-1}$	k_4 , s^{-1}	ref.
β -D-glucose-1- ¹ H at 25 °C	~200	~6000	1.8×10^6	1440	[89]
β -D-glucose-1- ¹ H at 25 °C	13 158		1.8×10^6	1440	[27]
β -D-glucose-1- ¹ H at 27 °C	10 000		2.1×10^6	1150	[61]
Used in the model	3000	6000	1.5×10^6	1500	

Diffusion coefficients

The determination of O_2 diffusion coefficient is especially important in SECM-based physical experiments and mathematical modelling of SECM, because electric current, formed by O_2 reduction process in (1.4), is used as a measurement for SECM experiment and many analytical formulas, applied for SECM response calculations by researchers, depend on O_2 diffusion coefficient. It was shown that O_2 diffusion is strongly

influenced by the presence of salts, glucose, etc. in solution [75]. This dependency for SECM experiments was established in this research (see section 1.5).

Table 1.2: Diffusion coefficients in water at 25 °C.

Diffusing reagent	$D, \text{m}^2\text{s}^{-1}$	ref.
Oxygen	Calculated experimentally	
Glucose	5×10^{-10}	[127]
Hydrogen peroxide	2.1×10^{-9}	[134, 139]
Gluconolactone	5×10^{-10}	[127]

Other diffusion coefficients were taken from scientific literature (Table 1.2). Diffusivity rates of Glc and Gll were considered the same due to very similar physico-chemical properties.

1.3 Mathematical model

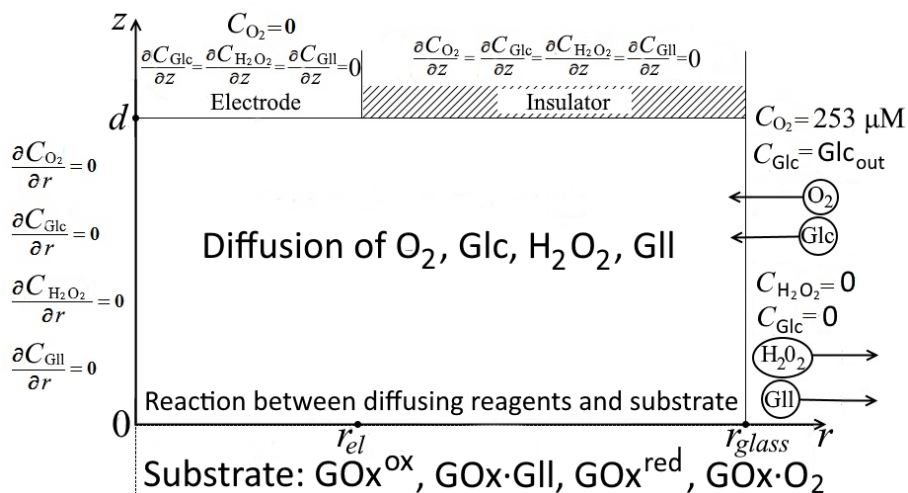


Figure 1.2: Scheme of simulation domain. All 8 reagents, boundary conditions for C_{diff} and the direction of outside flux are displayed.

Measurements of SECM acting in the redox-competition mode (Fig. 1.1) are changed into the scheme (1.2) due to the radial symmetry around the central axis of the electrode. Radial symmetry is a standard assumption in SECM modelling, though the case of off-centered UME was also investigated [39].

According to the second Fick's law [87], diffusion processes are expressed by the system of partial differential equations (PDE):

$$\begin{aligned}
 \frac{\partial C_{O_2}}{\partial t} &= D_{O_2} \Delta C_{O_2}, \\
 \frac{\partial C_{Glc}}{\partial t} &= D_{Glc} \Delta C_{Glc}, \\
 \frac{\partial C_{H_2O_2}}{\partial t} &= D_{H_2O_2} \Delta C_{H_2O_2}, \\
 \frac{\partial C_{Gll}}{\partial t} &= D_{Gll} \Delta C_{Gll}, \quad \text{for } 0 < t \leq T, \quad 0 < z < d, \quad 0 < r < r_{glass},
 \end{aligned} \tag{1.5}$$

where:

C_{O_2} , C_{Glc} , $C_{H_2O_2}$ and C_{Gll} are concentrations of diffusing reagents and expressed as functions of time t and spatial coordinates z and r . Notation $C_{diff} = C_{diff}(t, z, r) = (C_{O_2}, C_{Glc}, C_{H_2O_2}, C_{Gll})$ was used when 4 diffusing reagents were considered together.

D_{O_2} , D_{Glc} , $D_{H_2O_2}$ and D_{Gll} are diffusion coefficients of O_2 , Glc, H_2O_2 and Gll.

d is the distance between the enzyme-modified surface and the electrode, which is varying from 1 μm to 120 μm as shown in Fig. 1.2.

$r_{glass} = 80 \mu\text{m}$ is the radius of insulated area, $r_{el} = 5 \mu\text{m}$ is the radius of electrode.

T is the duration of a computational experiment measured in seconds (the evaluation of this parameter is further explained in the next section).

The Laplace operator Δ for concentration function C in cylindrical coordinates with radial symmetry is

$$\Delta C = \frac{1}{r} \frac{\partial}{\partial r} \left(r \frac{\partial C}{\partial r} \right) + \frac{\partial^2 C}{\partial z^2}.$$

Chemical reactions, which are represented by chemical equations (1.1)–(1.3), for non-diffusing reagents on the surface $z = 0$ are expressed by the system of ordinary differential equations (ODE):

$$\begin{aligned}
\frac{\partial C_{GOx^{ox}}}{\partial t} &= -k_1 C_{GOx^{ox}} C_{Glc} + k_{-1} C_{GOx \cdot Glc} + k_4 C_{GOx \cdot O_2} - \\
&\quad - k_{-4} C_{GOx^{ox}} C_{H_2O_2}, \\
\frac{\partial C_{GOx \cdot Glc}}{\partial t} &= k_1 C_{GOx^{ox}} C_{Glc} - (k_{-1} + k_2) C_{GOx \cdot Glc}, \\
\frac{\partial C_{GOx^{re}}}{\partial t} &= k_2 C_{GOx \cdot Glc} - k_3 C_{GOx^{re}} C_{O_2} + k_{-3} C_{GOx \cdot O_2}, \\
\frac{\partial C_{GOx \cdot O_2}}{\partial t} &= k_3 C_{GOx^{re}} C_{O_2} - k_{-3} C_{GOx \cdot O_2} - k_4 C_{GOx \cdot O_2} + \\
&\quad + k_{-4} C_{GOx^{ox}} C_{H_2O_2},
\end{aligned} \tag{1.6}$$

for $0 < t \leq T$, $0 \leq r \leq r_{glass}$,

where $C_{GOx^{ox}}$, $C_{GOx \cdot Glc}$, $C_{GOx^{re}}$ and $C_{GOx \cdot O_2}$ are concentrations of surface-immobilized reagents depending on time t and radius r . Notation $C_{surf} = C_{surf}(t, r) = (C_{GOx^{ox}}, C_{GOx \cdot Glc}, C_{GOx^{re}}, C_{GOx \cdot O_2})$ was used when all 4 surface reagents were considered.

Rate laws for diffusing substances on the base $z = 0$ are also deduced from chemical equations (1.1)–(1.3) and are used as the boundary conditions of third type on $z = 0$:

$$\begin{aligned}
D_{O_2} \frac{\partial C_{O_2}}{\partial z} &= k_3 C_{GOx^{re}} C_{O_2} - k_{-3} C_{GOx \cdot O_2}, \\
D_{Glc} \frac{\partial C_{Glc}}{\partial z} &= k_1 C_{GOx^{ox}} C_{Glc} - k_{-1} C_{GOx \cdot Glc}, \\
D_{H_2O_2} \frac{\partial C_{H_2O_2}}{\partial z} &= -k_4 C_{GOx \cdot O_2} + k_{-4} C_{GOx^{ox}} C_{H_2O_2}, \\
D_{Glu} \frac{\partial C_{Glu}}{\partial z} &= k_2 C_{GOx \cdot Glc}, \text{ for } 0 < t \leq T, z = 0, 0 \leq r < r_{glass}.
\end{aligned} \tag{1.7}$$

At the start of an enzymatic reaction oxygen concentration in the diffusion layer is $253 \mu\text{M}$ ($\text{M} = \text{mol/L}$ is a unit of molar concentration), surface concentration of active glucose oxidase GOx is $2.114 \times 10^{-8} \text{ mol/m}^2$ and all other reagents are considered absent. Therefore, initial conditions

for (1.5)–(1.6):

$$\begin{aligned}
C_{O_2} = 253 \mu\text{M}, \quad C_{Glc} = C_{H_2O_2} = C_{Gll} = 0, \\
\text{for } t = 0, \quad 0 \leq z \leq d, \quad 0 \leq r \leq r_{glass}, \\
C_{GOx^{ox}} = 2.114 \times 10^{-8} \text{ mol/m}^2, \\
C_{GOx \cdot Glc} = C_{GOx^{re}} = C_{GOx \cdot O_2} = 0, \quad \text{for } t = 0, \quad 0 \leq r \leq r_{glass}.
\end{aligned} \tag{1.8}$$

Boundary conditions have to be provided for diffusing materials in the system of equations (1.5). The Boundary condition on $z = 0$ is already given by (1.7) and others are formulated as follows. Due to the symmetry, in the center $r = 0$ there is no flow:

$$\begin{aligned}
\frac{\partial C_{O_2}}{\partial r} = \frac{\partial C_{Glc}}{\partial r} = \frac{\partial C_{H_2O_2}}{\partial r} = \frac{\partial C_{Gll}}{\partial r} = 0, \\
\text{for } 0 < t \leq T, \quad 0 \leq z \leq d, \quad r = 0.
\end{aligned} \tag{1.9}$$

On the border $r = r_{glass}$, i.e. on the edge of the insulating surface, there is fixed concentration of O_2 and Glc

$$\begin{aligned}
C_{O_2} = 253 \mu\text{M}, \quad C_{Glc} = Glc_{out}, \\
\text{for } 0 < t \leq T, \quad 0 \leq z \leq d, \quad r = r_{glass}.
\end{aligned} \tag{1.10}$$

The amount does not change during a single experiment as there is an unlimited source of O_2 and Glc outside of the modelled area in other parts of a Petri plate or air. However, an exterior glucose concentration Glc_{out} is varying from 0 mM to 0.6 mM in different experiments, where the value of 0 means that no glucose is present in the solution and surface reactions do not start.

All H_2O_2 and Gll are considered to be diffusing away on the border $r = r_{glass}$, hence

$$C_{H_2O_2} = C_{Gll} = 0, \quad \text{for } 0 < t \leq T, \quad 0 \leq z \leq d, \quad r = r_{glass}. \tag{1.11}$$

Finally, for the border $z = d$ on the insulator $r > r_{el}$ ($r_{el} = 5 \mu\text{m}$ is the radius of electrode) there is no flow:

$$\frac{\partial C_{O_2}}{\partial z} = \frac{\partial C_{Glc}}{\partial z} = \frac{\partial C_{H_2O_2}}{\partial z} = \frac{\partial C_{Glu}}{\partial z} = 0, \\ \text{for } 0 < t \leq T, z = d, r_{el} < r < r_{glass}. \quad (1.12)$$

On the electrode ($r < r_{el}$) all O_2 is consumed due to the speed of the chemical reaction (1.4):

$$C_{O_2} = 0, \quad \text{for } 0 < t \leq T, z = d, 0 \leq r \leq r_{el}. \quad (1.13)$$

The other 3 materials are blocked by electrode, therefore:

$$\frac{\partial C_{Glc}}{\partial z} = \frac{\partial C_{H_2O_2}}{\partial z} = \frac{\partial C_{Glu}}{\partial z} = 0, \\ \text{for } 0 < t \leq T, z = d, 0 \leq r \leq r_{el}. \quad (1.14)$$

1.4 Numerical solution

1.4.1 Discrete grid and notations

Non-uniform mesh

In order to solve initial-boundary value problem (1.5)–(1.14), first of all, a rectangular domain $\Omega_T = \{(t, z, r) \in \mathbb{R}^3 : 0 < t \leq T, 0 < z < d, 0 < r < r_{glass}\}$ had to be discretised.

Non-uniform meshing techniques are commonly employed for a numerical solution of ODEs and PDE and is motivated by: (i) higher accuracy [136], (ii) reduction of computation time [22, 76], (iii) dealing with infinities [52, 62], etc. Non-uniform meshes are used with finite difference schemes ([2, 53, 56, 78]), but mesh generation techniques are essential for finite element methods, where a domain is typically discretised by triangles, tetrahedrons, etc. [8, 30, 60, 63].

Another method is adaptive meshing, which allows dynamical mesh refinement during calculations according to the behaviour of the solution, i.e. some a posteriori error estimator like the gradient. This method has been used in research [25, 76, 140] and detailed in textbooks [10, 113].

The non-uniform mesh was used in SECM modelling for several reasons:

1. Area around the UME (ultramicroelectrode) provides essential information about the system but is also much smaller (by a factor $R_g \simeq 10$) than the rest of the system so naturally more mesh points have to be assigned there.
2. Special care must be taken around junction point between the UME and insulator as both the largest flow of oxygen, i.e. $\partial C_{O_2}/\partial z$, and the largest computational errors are registered there.
3. At the start of the process gradients are very sharp and a very small timestep τ is necessary, but as the solutions come closer to steady-state, much larger τ is sufficient.

Methods of mesh generation

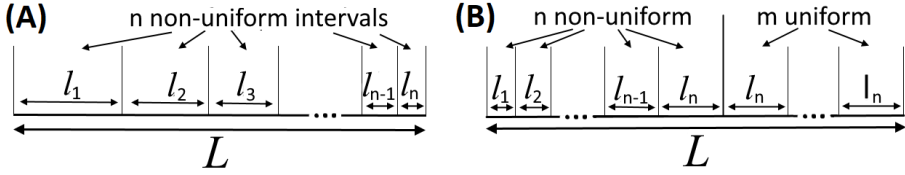


Figure 1.3: (A) Distance of length L is divided into n non-uniform intervals of lengths l_1, \dots, l_n . (B) Distance is divided into n non-uniform intervals and m uniform intervals of length l_n .

Non-uniform mesh is generated by exponential method, which is defined by the ratio q between lengths of two adjacent intervals

$$l_i = ql_{i-1}, q < 1 \text{ – mesh with decreasing lengths,}$$

$$q > 1 \text{ – increasing lengths.}$$

Two methods have been proposed and used for spatial grid generation as shown in Fig. 1.3.

Method 1. The distance L has to be divided into n decreasing (if necessary, increasing) intervals, where l_1 and q are unknown (Fig. 1.3A). An additional condition is necessary and $l_n = l_1^\alpha$, $\alpha > 1$ ($0 < \alpha < 1$) has been used, which guarantees that for $l_1 \ll 1$ (which is the case in SECM model) l_n is several orders of magnitude smaller (larger) than l_1 . Consequently, the grid is strongly contracted at the end of full interval L , which is what is required for the grid at $r = r_{el}$. The rate of contraction is determined by parameter α .

By adding lengths l_i , the following system is provided for l_1 and q :

$$\begin{cases} l_1 + ql_1 + q^2l_1 + \dots + q^{n-1}l_1 = L, \\ q^{n-1}l_1 = l_1^\alpha. \end{cases} \quad (1.15)$$

The sum of geometric series is applied to derive nonlinear equation from (1.15)

$$\begin{cases} l_1 = \frac{1-q}{1-q^n}L, \\ q = l_1^{\frac{\alpha-1}{n-1}}, \end{cases} \quad (1.16)$$

which has been solved by fixed point iterations, which converge for (1.16) [113]. Approximately 10 – 20 iterations are enough to reach computer precision.

Method 2. The distance L is divided into 2 types of intervals: n intervals are of decreasing (increasing) length and m intervals are of the fixed length according to Fig. 1.3B. This mixed method is employed then very large (compared to l_1) distance L has to be discretised and it becomes undesirable to have a too narrow (too wide) interval.

In this case, l_1 is known i.e. given as a parameter or calculated by method 1, q is unknown. By using the exponential growth condition $l_n = q^{n-1}l_1$, series have been derived

$$l_1 + ql_1 + q^2l_1 + \dots + q^{n-1}l_1 + mq^{n-1}l_1 = L.$$

As in the case of (1.16), the sum of series is calculated and fixed point iterations for unknown q are obtained

$$q = \sqrt[n-1]{\frac{1}{m} \left(\frac{L}{l_1} - \frac{1-q^n}{1-q} \right)}. \quad (1.17)$$

Iterations (1.17) converge for both $q > 1$ and $q < 1$ with all realistic values of parameters.

Grid construction

The mesh $\bar{\omega}$ (Fig. 1.4) was defined with non-uniform steps:

$$\begin{aligned} \bar{\omega}_h &= \{z_i : z_i = z_{i-1} + h_i, i = 1, \dots, N_1, z_0 = 0, z_{N_1} = d\}, \\ \bar{\omega}_l &= \{r_j : r_j = r_{j-1} + l_j, j = 1, \dots, j_{\text{junc}}, \dots, N_2, \\ &\quad r_0 = 0, r_{j_{\text{junc}}} = r_{el}, r_{N_2} = r_{glass}\}, \\ \bar{\omega}^\tau &= \{t^k : t^k = t^{k-1} + \tau_k, k = 1, \dots, K, t^0 = 0, t^K = T\}, \\ \bar{\omega} &= \bar{\omega}^\tau \times \bar{\omega}_h \times \bar{\omega}_l. \end{aligned}$$

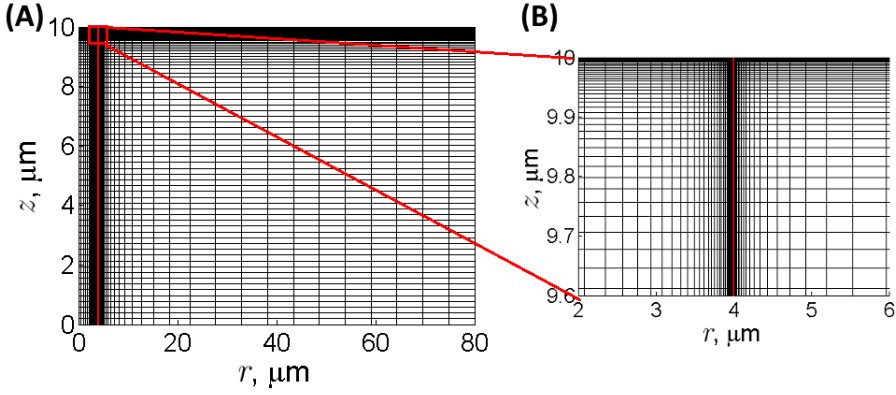


Figure 1.4: Mesh $\bar{\omega}_h \times \bar{\omega}_l$ of size 100×100 . The majority of mesh points cannot be seen as they are too close to the domains of compression. The red line shows the junction between the electrode and isolator at $4 \mu\text{m}$. (A) full mesh, (B) Part of mesh zoomed near the electrode.

The junction point between the UME and insulator, i.e. $r = r_{el}$, was always at fixed index $j_{\text{junc}} = 0.5N_2$. 50% of mesh $\bar{\omega}_l$ points were allocated for computations at the electrode, because this part of domain was used for calculation of SECM response and high accuracy was necessary.

The spatial grid was constructed in 3 steps:

1. $\bar{\omega}_h$ was discretised by method 2 starting from the last interval h_{N_1} and calculating backwards. Parameters were set: $n = 0.6N_1$, $m = 0.4N_1$, $h_{N_1} = 10^{-8}/N_1$, and $q > 1$ was calculated by (1.17). Method 2 was chosen, because the length h_{N_1} , which is the interval near the electrode, had to be fixed in order to prevent additional errors in SECM response curve, then the full distance d was changed.
2. $\bar{\omega}_l$ with $r \leq r_{el}$, i.e. indexes $j \leq j_{\text{junc}}$, was discretised into decreasing intervals using method 1, parameters $n = 0.5N_2$, $\alpha = 1.5$ and $q < 1$ calculated by (1.16).
3. The rest of r_{glass} was divided into increasing intervals by method 2 with parameters $n = 0.6N_2$, $m = 0.4N_2$. The starting length l_1 was taken from division of interval r_{el} .

An advantage of non-uniform mesh was demonstrated in Fig. 1.5A, where electric current i was plotted depending on the mesh size. Even

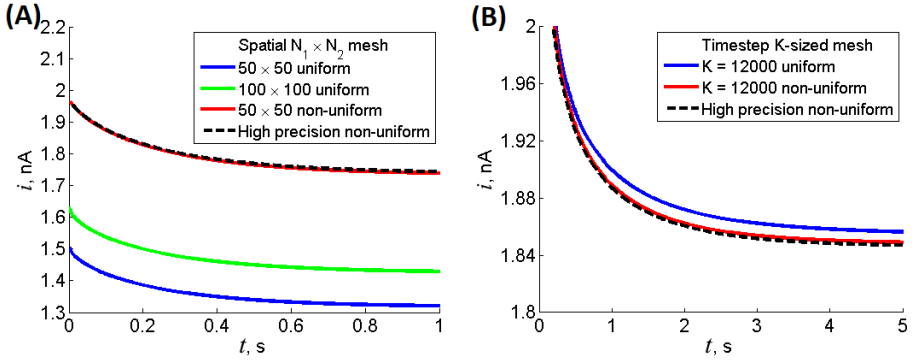


Figure 1.5: Advantages of non-uniform vs uniform mesh (A) Size of spatial mesh was analysed, (B) Size of timestep mesh.

small 50×50 non-uniform mesh performed better than the uniform grid of the same size and was already comparatively close to the result computed with much more dense mesh ($N = 400$). A high precision result can still be reached with uniform mesh as current curves converge, but the computing power requirement would be very large.

For the purpose of model testing, $\bar{\omega}_h \times \bar{\omega}_l$ mesh size $N_1 = 100$, $N_2 = 100$ was sufficient, but final computations were carried with 400×400 grid. The size was set after carefully examining the errors between calculations with chosen mesh and one 2 times larger and evaluating that the error is not larger than 1.0%, which was considered sufficient.

For the construction of timestep grid, parameter T had to be determined, where T is the time necessary to reach steady-state. It was estimated experimentally (see section 1.4.4) that $T = \sim 6 - 8$ s. Timestep size τ_k was set to

$$\begin{aligned} \tau_k &= 0.0001, & \text{for } t < 1 \text{ s,} \\ \tau_k &= 0.001, & \text{for } 1 \text{ s} \leq t < 2 \text{ s,} \\ \tau_k &= 0.01, & \text{for } 2 \text{ s} \leq t < T \end{aligned}$$

and the derived size of timestep grid $\bar{\omega}^\tau$ was approximately 12000 depending on T . At the beginning of process, a very small value of τ_k was chosen, because concentrations altered very rapidly. Afterwards, the process levelled off and τ_k was gradually decreased.

Computational tests were provided in Fig. 1.5B, which demonstrate, that current I calculated by 12000-sized mesh is reasonably close to

high precision calculations ($K \approx 100\,000$). Besides, it is evident that the construction of timestep mesh has less influence on the error compared to spatial mesh.

Notations for numerical solution

Equations for concentrations C_{diff} of diffusing reagents differ by initial-boundary conditions (1.7)–(1.14) and diffusion coefficient D . In order to prevent repetition of difference formulas, the notation

$$U_{i,j}^k \approx C_{\text{diff}}(t^k, z_i, r_j)$$

will be applied to indicate that all four C_{diff} are approximated by the same formula and the appropriate diffusion coefficient D . In case the concentration of particular reagent is necessary, then notation

$$\begin{aligned} \mathbf{U} &= (U_{O_2}, U_{Glc}, U_{H_2O_2}, U_{Glu}), \\ U_{O_2,i,j}^k &\approx C_{O_2}(t^k, z_i, r_j), \dots \end{aligned} \quad (1.18)$$

will be used. The similar notation is used for surface-bound reagents

$$\begin{aligned} V_j^k &\approx C_{\text{surf}}(t^k, r_j), \\ \mathbf{V} &= (V_{GOx^{ox}}, V_{GOx \cdot Glc}, V_{GOx^{re}}, V_{GOx \cdot O_2}), \\ V_{GOx^{ox},j}^k &\approx C_{GOx^{ox}}(t^k, r_j), \dots \end{aligned} \quad (1.19)$$

1.4.2 ADI Finite difference schemes

The system of 8 differential equations (1.5)–(1.6) with initial conditions (1.8) and boundary conditions (1.7), (1.9)–(1.14) has to be solved. The alternating-direction implicit finite difference method (ADIFDM) was used for 4 diffusion equations (1.5).

ADIFDM is a classical method for solving diffusion equations in 2D space. The effectiveness of this method was shown by various research groups [19, 94, 116, 120]. There are significant advantages of ADIFDM over a simpler explicit FDM scheme. First of all, approximation error for the ADI scheme is $\mathcal{O}(\tau^2 + h^2)$, where $\tau = \max_k(\tau_k)$ and $h = \max_{i,j}(h_i, l_j)$, i.e. it is second order for all variables with an assumption that sufficient continuity conditions are satisfied:

$$\left| \frac{\partial^3 C_{\text{diff}}}{\partial t^3} \right| < M, \quad \left| \frac{\partial^4 C_{\text{diff}}}{\partial r^4} \right| < M, \quad \left| \frac{\partial^4 C_{\text{diff}}}{\partial z^4} \right| < M, \quad \left| \frac{\partial^5 C_{\text{diff}}}{\partial r^2 \partial z^2 \partial t} \right| < M$$

for some constant M . In addition, it is unconditionally stable, which is an important feature, because h_i and l_j are very small. Moreover, a tridiagonal system of linear equations is constructed, which is solved very efficiently with Thomas algorithm. Additional details and proofs of these properties are presented in Samarskii [116], Morton et al. [101] or original paper by Peaceman and Rachford [108].

r -direction finite difference schemes

At each timestep t^k and fixed $i = 1, \dots, N_1 - 1$, equations (1.5) were solved in the direction of r axis using a scheme:

$$\begin{aligned} \frac{\bar{U}_{i,j} - U_{i,j}^k}{0.5\tau_k} &= \frac{D}{r_j l_{j+0.5}} \left(r_{j+0.5} \frac{\bar{U}_{i,j+1} - \bar{U}_{i,j}}{l_{j+1}} - r_{j-0.5} \frac{\bar{U}_{i,j} - \bar{U}_{i,j-1}}{l_j} \right) \\ &+ \frac{D}{h_{i+0.5}} \left(\frac{U_{i+1,j}^k - U_{i,j}^k}{h_{i+1}} - \frac{U_{i,j}^k - U_{i-1,j}^k}{h_i} \right), \\ &j = 1, \dots, N_2 - 1, \end{aligned} \quad (1.20)$$

where

$$\begin{aligned} r_{j+0.5} &= \frac{r_j + r_{j+1}}{2}, & r_{j-0.5} &= \frac{r_{j-1} + r_j}{2}, \\ h_{i+0.5} &= \frac{h_i + h_{i+1}}{2}, & l_{j+0.5} &= \frac{l_j + l_{j+1}}{2}, \\ \bar{U}_{i,j} &\approx C_{\text{diff}}(t^k + 0.5\tau_k, z_i, r_j). \end{aligned}$$

$\bar{U}_{i,j}$ is an unknown value in the middle of timestep, which has to be computed while solving in the r -direction.

Boundary value \bar{U}_{i,N_2} was simply taken from boundary condition (1.9):

$$\bar{U}_{i,N_2} = C_{\text{diff}}|_{r=r_{el}}, \quad i = 0, \dots, N_1. \quad (1.21)$$

but to keep second order of approximation special care was taken for axis symmetry $r = 0$. Equations (1.5), written in their general form $C_t = D(C_{rr} + \frac{1}{r}C_r + C_{zz})$, were transformed at point $r = 0$ into

$$C_t = 2D C_{rr} + D C_{zz}. \quad (1.22)$$

Here, Taylor series expansion $C_r = C_r|_{r=0} + rC_{rr}|_{r=0} + \mathcal{O}(l_j^2)$ and boundary condition $C_r|_{r=0} = 0$ (1.9) were used to get rid of division by 0 in $\frac{1}{r}$.

Afterwards, the so-called ghost point $\bar{U}_{i,-1}$ was introduced to approximate derivative (1.9) with the symmetric second order difference scheme $(\bar{U}_{i,1} - \bar{U}_{i,-1})/2l_1 = 0$. Using equation (1.22), approximation at $j = 0$ was obtained

$$\begin{aligned} \frac{\bar{U}_{i,0} - U_{i,0}^k}{0.5\tau_k} &= 4D \left(\frac{\bar{U}_{i,1} - \bar{U}_{i,0}}{l_1^2} \right) + \\ &+ \frac{D}{h_{i+0.5}} \left(\frac{U_{i+1,0}^k - U_{i,0}^k}{h_{i+1}} - \frac{U_{i,0}^k - U_{i-1,0}^k}{h_i} \right), \quad i = 1, \dots, N_1 - 1. \end{aligned} \quad (1.23)$$

The boundary layer $z = h$, i.e. the layer at the electrode and fixed index $i = N_1$, was approximated using differential equations (1.5) and boundary conditions (1.12)–(1.14). Diffusion of reagents Glc, H_2O_2 , Gll is not interfered by the electrode so the same scheme could be used for all $j = 1, \dots, N_2 - 1$. Equations for functions C_{Glc} , $C_{H_2O_2}$ and C_{Gll} were approximated with the ghost point $U_{N_1+1,j}^k$ technique as in (1.23) and difference equation was calculated for $i = N_1$:

$$\begin{aligned} \frac{\bar{U}_{N_1,j} - U_{N_1,j}^k}{0.5\tau_k} &= \\ &= \frac{D}{r_j l_{j+0.5}} \left(r_{j+0.5} \frac{\bar{U}_{N_1,j+1} - \bar{U}_{N_1,j}}{l_{j+1}} - r_{j-0.5} \frac{\bar{U}_{N_1,j} - \bar{U}_{N_1,j-1}}{l_j} \right) + \\ &\quad + 2D \frac{U_{N_1-1,j}^k - U_{N_1,j}^k}{h_{N_1}^2}, \quad j = 1, \dots, N_2 - 1. \end{aligned} \quad (1.24)$$

Considering O_2 , distinct boundary condition (1.13) was provided for $r \leq r_{el}$, i.e. until the junction between the electrode and isolator, so the boundary value for function C_{O_2} was set to

$$\bar{U}_{N_1,j} = 0, \quad j = 0, \dots, j_{\text{junc}}, \quad (1.25)$$

where j_{junc} is the index at $r = r_{el}$. For points $r > r_{el}$, the same difference equation (1.24) was used with the exception that indexes $j = j_{\text{junc}} + 1, \dots, N_2 - 1$ were provided.

The boundary layer $z = 0$, i.e. layer at the substrate, fixed index $i = 0$, was approximated using differential equations (1.5) and non-linear boundary conditions (1.7). In order to simplify the approximation formula, conditions (1.7) were rewritten in general form

$$D \frac{\partial C_{\text{diff}}}{\partial z} = F_{\text{boundary}}(C_{\text{diff}}, C_{\text{surf}}),$$

for $0 < t \leq T, z = 0, 0 < r < r_{\text{glass}},$ (1.26)

where F_{boundary} are nonlinear functions from the right-hand side of boundary condition (1.7). Using notations (1.18) and (1.19), functions F_{boundary} were expressed in numerical values:

$$F_{\text{boundary}}(C_{\text{diff}}, C_{\text{surf}}) \approx F_{\text{boundary}}(\mathbf{U}_{0,j}^k, \mathbf{V}_j^k) =$$

$$= \begin{pmatrix} k_3 V_{GOx^{re},j}^k U_{O_2,0,j}^k - k_{-3} V_{GOx \cdot O_2,j}^k \\ k_1 V_{GOx^{ox},j}^k U_{Glc,0,j} - k_{-1} V_{GOx \cdot Glc,j}^k \\ -k_4 V_{GOx \cdot O_2,j}^k + k_{-4} V_{GOx^{ox},j}^k U_{H_2O_2,0,j}^k \\ k_2 V_{GOx \cdot Glc,j}^k \end{pmatrix}.$$

Approximations of boundary conditions (1.26) were calculated using ghost point for value $U_{-1,j}^k$ technique:

$$\frac{\bar{U}_{0,j} - U_{0,j}^k}{0.5\tau_k} = \frac{D}{r_j l_{j+0.5}} \left(r_{j+0.5} \frac{\bar{U}_{0,j+1} - \bar{U}_{0,j}}{l_{j+1}} - r_{j-0.5} \frac{\bar{U}_{0,j} - \bar{U}_{0,j-1}}{l_j} \right)$$

$$+ 2D \frac{U_{1,j}^k - U_{0,j}^k}{h_1^2} - \frac{2}{h_1} F_{\text{boundary}}(\mathbf{U}_{0,j}^k, \mathbf{V}_j^k), \quad j = 1, \dots, N_2 - 1. \quad (1.27)$$

Finally, it must be noted that for corner value $\bar{U}_{0,0}$ both methods (1.23) and (1.27) were applied. Methods (1.23) and (1.24) were used to approximate $\bar{U}_{N_1,0}$ for all diffusing materials except O_2 , because $\bar{U}_{O_2,N_1,0} = 0$ according to (1.13).

z-direction finite difference schemes

Approximation formulas in the direction of z-axis were calculated using the same methods as in (1.20)–(1.27). At each fixed $j = 1, \dots, N_2 - 1$, equations (1.5) were solved in z-direction:

$$\frac{U_{i,j}^{k+1} - \bar{U}_{i,j}}{0.5\tau_k} = \frac{D}{r_j l_{j+0.5}} \left(r_{j+0.5} \frac{\bar{U}_{i,j+1} - \bar{U}_{i,j}}{l_{j+1}} - r_{j-0.5} \frac{\bar{U}_{i,j} - \bar{U}_{i,j-1}}{l_j} \right)$$

$$+ \frac{D}{h_{i+0.5}} \left(\frac{U_{i+1,j}^{k+1} - U_{i,j}^{k+1}}{h_{i+1}} - \frac{U_{i,j}^{k+1} - U_{i-1,j}^{k+1}}{h_i} \right),$$

$i = 1, \dots, N_1 - 1, \quad (1.28)$

where $U_{i,j}^{k+1}$ is an unknown value for z -direction.

The boundary layer $z = h$ (i.e. $i = N_1$) for fixed index j was approximated by:

$$\begin{aligned} \frac{U_{N_1,j}^{k+1} - \bar{U}_{N_1,j}}{0.5\tau_k} &= \\ &= \frac{D}{r_j l_{j+0.5}} \left(r_{j+0.5} \frac{\bar{U}_{N_1,j+1} - \bar{U}_{N_1,j}}{l_{j+1}} - r_{j-0.5} \frac{\bar{U}_{N_1,j} - \bar{U}_{N_1,j-1}}{l_j} \right) + \\ &+ 2D \frac{U_{N_1-1,j}^{k+1} - U_{N_1,j}^{k+1}}{h_{N_1}^2}, \quad j = 1, \dots, N_2 - 1 \text{ considering Glc, H}_2\text{O}_2, \text{Gll,} \\ &\quad j = j_{\text{junc}} + 1, \dots, N_2 - 1 \text{ considering O}_2, \end{aligned} \quad (1.29)$$

where j_{junc} is the index of the junction between the electrode and isolator. The values of O_2 at the UME, i.e. $r \leq r_{el}$, were set to

$$U_{N_1,j}^{k+1} = 0, \quad j = 0, \dots, j_{\text{junc}}. \quad (1.30)$$

The boundary layer $z = 0$ (i.e. $i = 0$) for fixed index $j = 1, \dots, N_2 - 1$ was approximated by the same method as in (1.26)–(1.27). Values of $\mathbf{U}_{0,j}^k$ and \mathbf{V}_j^k from the previous timestep were taken for the purpose of linearization:

$$\begin{aligned} \frac{U_{0,j}^{k+1} - \bar{U}_{0,j}}{0.5\tau_k} &= \frac{D}{r_j l_{j+0.5}} \left(r_{j+0.5} \frac{\bar{U}_{0,j+1} - \bar{U}_{0,j}}{l_{j+1}} - r_{j-0.5} \frac{\bar{U}_{0,j} - \bar{U}_{0,j-1}}{l_j} \right) \\ &+ 2D \frac{U_{1,j}^{k+1} - U_{0,j}^{k+1}}{h_1^2} - \frac{2}{h_1} F_{\text{boundary}}(\mathbf{U}_{0,j}^k, \mathbf{V}_j^k). \end{aligned} \quad (1.31)$$

It should be noted, that the expression $F_{\text{boundary}}(\mathbf{U}_{0,j}^{k+1}, \mathbf{V}_j^{k+1})$ had to be chosen according to the method used. The system of nonlinear algebraic equations would be formulated, which could be solved by some iterative method. However, according to a couple of performed testing computer simulations, the second iteration was already very close to the first one and running the iteration process was determined unnecessary.

Special approximation of equations (1.5) was used at the boundary $r = 0$ as explained in (1.22)–(1.23). For fixed index $j = 0$

$$\begin{aligned} \frac{U_{i,0}^{k+1} - \bar{U}_{i,0}}{0.5\tau_k} &= 4D \left(\frac{\bar{U}_{i,1} - \bar{U}_{i,0}}{l_1^2} \right) + \\ &+ \frac{D}{h_{i+0.5}} \left(\frac{U_{i+1,0}^{k+1} - U_{i,0}^{k+1}}{h_{i+1}} - \frac{U_{i,0}^{k+1} - U_{i-1,0}^{k+1}}{h_i} \right), \quad i = 1, \dots, N_1 - 1. \end{aligned} \quad (1.32)$$

Value for $j = N_2$ was taken from boundary condition at $r = r_{el}$ (1.9)

$$U_{i,N_2}^{k+1} = C_{\text{diff}}|_{r=r_{el}}, \quad i = 0, \dots, N_1.$$

Approximation at corners $U_{0,0}^{k+1}$ and $U_{N_1,0}^{k+1}$ were set in the same manner as with r -direction.

1.4.3 Numerical algorithms

Reduction of schemes to systems of linear equations

In this section, matrices of systems of linear equations are calculated from finite difference schemes. It is shown that these systems are tridiagonal and their right-hand sides are also derived.

First of all, matrices were calculated for each fixed row $i = 1, \dots, N_1 - 1$ ($i = 0$ and $i = N_1$ are separate cases) in order to find unknown middle-step values $\bar{U}_{i,j}$. Schemes (1.20) were converted into $N_2 - 2$ equations for $j = 1, \dots, N_2 - 2$

$$a_j \bar{U}_{i,j-1} + b_j \bar{U}_{i,j} + c_j \bar{U}_{i,j+1} = R_{i,j}, \quad (1.33)$$

where

$$a_j = \frac{D r_{j-0.5}}{l_j l_{j-0.5} r_j}, \quad c_j = \frac{D r_{j+0.5}}{l_{j+1} l_{j-0.5} r_j},$$

$$b_j = -\frac{2}{\tau_k} - a_j - c_j, \quad j = 1, \dots, N_2 - 2.$$

The right-hand side $R_{i,j}$ in (1.33) was calculated by

$$R_{i,j} = \alpha_i U_{i-1,j}^k + \beta_i U_{i,j}^k + \gamma_i U_{i+1,j}^k, \quad j = 1, \dots, N_2 - 2, \quad (1.34)$$

where

$$\alpha_i = -\frac{D}{h_{i+0.5} h_i}, \quad \beta_i = -\frac{2}{\tau_k} + \frac{2D}{h_i h_{i+1}},$$

$$\gamma_i = -\frac{D}{h_{i+0.5} h_{i+1}}.$$

In the case of $j = 0$, the equation was derived from the scheme (1.23):

$$b_0 \bar{U}_{i,0} + c_0 \bar{U}_{i,1} = R_{i,0}, \quad (1.35)$$

where

$$b_0 = -\frac{2}{\tau_k} - c_0, \quad c_0 = \frac{4D}{l_1^2},$$

$$R_{i,0} = \alpha_i U_{i-1,0}^k + \beta_i U_{i,0}^k + \gamma_i U_{i+1,0}^k.$$

The final equation was obtained from (1.20) and the boundary value (1.21) for $j = N_2 - 1$:

$$a_j \bar{U}_{i,j-1} + b_j \bar{U}_{i,j} = R_{i,j},$$

$$R_{i,j} = -c_j C_{\text{diff}} \Big|_{r=r_{el}} + \alpha_i U_{i-1,j}^k + \beta_i U_{i,j}^k + \gamma_i U_{i+1,j}^k, \quad (1.36)$$

where a_j , b_j and other coefficients are the same as in (1.33)–(1.34) with $j = N_2 - 1$.

Finally, tridiagonal N_2 -sized matrix was formed from (1.33)–(1.36)

$$\begin{pmatrix} b_0 & c_0 & 0 & \dots & 0 & 0 \\ a_1 & b_1 & c_1 & \dots & 0 & 0 \\ 0 & a_2 & b_2 & \dots & 0 & 0 \\ \vdots & & & & & \\ 0 & 0 & 0 & \dots & a_{N_2-1} & b_{N_2-1} \end{pmatrix}$$

and the right-hand side of the system of linear equations was set to

$$\mathbf{R}_i = (R_{i,0}, R_{i,1}, \dots, R_{i,N_2-1}).$$

Two more systems were derived for special cases of boundary rows. For the case of $i = N_1$, i.e. for values at the UME, schemes (1.24) were used for C_{Gl_c} , $C_{H_2O_2}$ and C_{Gl} to form N_2 -sized matrix and (1.24)–(1.25) were reduced to smaller $(N_2 - j_{\text{junc}})$ -sized system for C_{O_2} which was due to its special boundary condition.

For the solution in z -direction, i.e. the calculation of $U_{0,j}^{k+1}$, schemes (1.28)–(1.32) were reduced into linear systems in the same manner as previously explained. It is easy to observe that these systems have tridiagonal matrices of size $N_1 + 1$ or N_1 in the case of C_{O_2} at $j \leq j_{\text{junc}}$.

Solution of a linear system

$N_2 - 1$ tridiagonal systems of linear equations were obtained for each 4 diffusing reagents, i.e. $4N_2 + 4$ systems in total, while solving in the direction of r axis. Additionally, $4N_1$ tridiagonal systems were constructed for z -direction. All these tridiagonal systems were solved

using the Thomas algorithm (Tridiagonal matrix algorithm, TDMA) [113] which is known to be highly efficient for this type of systems as it requires only $\mathcal{O}(N)$ operations.

The stability of TDMA is not always guaranteed as it may become unstable in case, for example, of singular matrix. Several conditions of the stability exist and can be referred to numerical methods textbooks such as Quarteroni et al. [113] and Higham [71]. In the case of matrices presented in the Thesis, diagonal dominance is sufficient criteria:

$$|b_j| > |a_j| + |c_j| \quad j = 1, \dots, N,$$

where b_j is the element in j -th row of the main diagonal, a_j and c_j – in the other diagonals.

It is evident that the matrix formed from (1.33), (1.35) and (1.36) is diagonally dominant and straightforward to prove that all other matrices are as well.

Algorithm for the system of ordinary differential equations

The system of ODEs (1.6) for non-diffusing reagents was solved by the trapezoidal (also known as symmetrical Euler or Crank-Nicolson) method, which has $\mathcal{O}(\tau^2)$ truncation error with the assumption that $C_{\text{surf}} \in C^3(0, T)$ [113]. Inserting already calculated $U_{0,j}^{k+1}$, the formula was derived:

$$\begin{aligned} \frac{V_{GOx^{ox},j}^{k+1} - V_{GOx^{ox},j}^k}{\tau} &= -k_1 \widehat{V}_{GOx^{ox},j} \widehat{U}_{Glc,0,j} + k_{-1} \widehat{V}_{GOx \cdot Glc,j} + \\ &\quad + k_4 \widehat{V}_{GOx \cdot O_2} - k_{-4} \widehat{V}_{GOx^{ox},j} \widehat{U}_{H_2O_2,0,j}, \\ \frac{V_{GOx \cdot Glc,j}^{k+1} - V_{GOx \cdot Glc,j}^k}{\tau} &= k_1 \widehat{V}_{GOx^{ox},j} \widehat{U}_{Glc,0,j} - (k_{-1} + k_2) \widehat{V}_{GOx \cdot Glc,j}, \\ \frac{V_{GOx^{re},j}^{k+1} - V_{GOx^{re},j}^k}{\tau} &= k_2 \widehat{V}_{GOx \cdot Glc,j} - k_3 \widehat{V}_{GOx^{re},j} \widehat{U}_{O_2,0,j} + \\ &\quad + k_{-3} \widehat{V}_{GOx \cdot O_2,j}, \\ \frac{V_{GOx \cdot O_2,j}^{k+1} - V_{GOx \cdot O_2,j}^k}{\tau} &= k_3 \widehat{V}_{GOx^{re},j} \widehat{U}_{O_2,0,j} - k_{-3} \widehat{V}_{GOx \cdot O_2,j} - \\ &\quad - k_4 \widehat{V}_{GOx \cdot O_2,j} + k_{-4} \widehat{V}_{GOx^{ox},j} \widehat{U}_{H_2O_2,0,j}, \\ &\quad j = 0, \dots, N_2 - 1, \end{aligned} \tag{1.37}$$

where

$$\widehat{U}_{0,j} = \frac{U_{0,j}^k + U_{0,j}^{k+1}}{2} \text{ and } \widehat{V}_j = \frac{V_j^k + V_j^{k+1}}{2}.$$

(1.37) was then rewritten in an easily solvable system of 4 linear equations

$$A\mathbf{V}_j^{k+1} = B,$$

as A and B depends only on V_j^k , $\widehat{U}_{0,j}$ and coefficients.

The trapezoid method can become unstable if the derivatives of right-hand side functions are too large, which is caused by too large reactions rate constants compared to timestep τ . It was necessary to have varying reactions coefficients to able to model their influence on SECM response (electric current) and for fine-tuning them (see subsection 1.2).

In order to solve this problem, the algorithm was adjusted by dividing current time interval (t^k, t^{k+1}) into n parts so timestep in (1.37) was reduced to $\tau_n = \tau/n$. $\widehat{U}_{0,j}$ was changed into $\widehat{U}_{0,j}^{(p)}$, $p = 1, \dots, n$ by linear interpolation at timestep $k + p\tau_n$ between $U_{0,j}^k$ and $U_{0,j}^{k+1}$, and V_j^k was changed

$$\begin{aligned} V_j^{k,(1)} &= V_j^k, \\ V_j^{k,(p)} &= V_j^{k+1,(p-1)}, \quad p = 2, \dots, n. \end{aligned}$$

1.4.4 Computation of SECM response

The model allows to calculate the concentration of diffusing materials O_2 , Glc, H_2O_2 , Gll and non-diffusing reagents GOx^{ox} , $GOx \cdot Gll$, GOx^{red} , $GOx \cdot O_2$ at any time t and position z and r . The main parameter, known as the response of ultramicroelectrode (SECM response), is an electric current, which is measured by an electrode at position $z = 0$, $0 < r < r_{el}$ and formed by the flux of O_2 . The graph of SECM response (electric current, measured by SECM) is also called the approach curve, because physical experiments are conducted by moving the UME closer to the enzyme-modified surface, i.e. approaching the surface, and registering electric signal at each stop.

The current through the electrode is calculated as a function of time [11, 13, 138]:

$$i(t) = 2\pi nFD_{O_2} \int_0^{r_{el}} \left. \frac{\partial C_{O_2}}{\partial z} \right|_{z=d} r dr, \quad (1.38)$$

where $n = 4$ is number of electrons exchanged and the Faraday constant $F = 9.6485 \times 10^4 \text{ A s mol}^{-1}$.

In order to calculate derivative $\left. \frac{\partial C_{O_2}}{\partial z} \right|_{z=d}$ in (1.38), C_{O_2} was approximated by fourth order Newton interpolating polynomial [113] at each node t_k , $i = N_1, j = 0, \dots, j_{\text{junc}}$

$$P(t_k, z, r_j) = U_{N_1, j}^{k+1} + f[z_{N_1}, z_{N_1-1}](z - z_{N_1}) + \dots + f[z_{N_1}, z_{N_1-1}, \dots, z_{N_1-4}](z - z_{N_1}) \cdot \dots \cdot (z - z_{N_1-4}), \quad j = 1, \dots, j_{\text{junc}}. \quad (1.39)$$

Divided differences $f[z_{N_1}, \dots]$ were calculated by iterative formulas

$$f[z_{N_1}, z_{N_1-1}] = \frac{U_{N_1, j}^{k+1} - U_{N_1-1, j}^{k+1}}{z_{N_1} - z_{N_1-1}},$$

$$\dots$$

$$f[z_{N_1}, z_{N_1-1}, \dots, z_{N_1-4}] = \frac{f[z_{N_1-1}, \dots, z_{N_1-4}] - f[z_{N_1}, \dots, z_{N_1-3}]}{z_{N_1} - z_{N_1-4}}. \quad (1.40)$$

Using (1.39), derivative was approximated $\left. \frac{\partial C_{O_2}}{\partial z} \right|_{z=d} \approx \left. \frac{\partial P(t_k, z, r_j)}{\partial z} \right|_{z=d}$ with error $\mathcal{O}(h^4)$. Such high accuracy was necessary, because the gradient of C_{O_2} at the UME is large and it guaranteed that error was minimized even for small N_1 .

The integral (1.38) was approximated by second order Newton-Cotes quadrature formulae (trapezoid rule, [113]):

$$i(t) \Big|_{t=t_k} \approx 2\pi n F D_{O_2} \left(\sum_{j=1}^{j_{\text{junc}}-1} l_{j+0.5} r_j \left. \frac{\partial P(t_k, z, r_j)}{\partial z} \right|_{z=d} + 0.5 l_{j_{\text{junc}}} r_{j_{\text{junc}}} \left. \frac{\partial P(t_k, z, r_{j_{\text{junc}}})}{\partial z} \right|_{z=d} \right). \quad (1.41)$$

For comparison with experimental data, steady-state current

$$i = \lim_{t \rightarrow \infty} i(t)$$

was calculated. Because of computational reasons, it was enough to take modelling parameter T large enough to ensure that relative error for current i is smaller than 0.001 % between two following timesteps. Modelling results show that depending on the model parameters (distance d and Glc concentration) it takes $T = \sim 6-8 \text{ s}$ to achieve necessary accuracy.

1.4.5 Implementation details and algorithm analysis

The program code including mesh generation, finite difference schemes, linear solver and other numerical methods was implemented by the author using Python (Anaconda distribution). Additional libraries were employed:

- NumPy – efficient calculations of operations with vectors and matrices. Inner loops were vectorised according to NumPy standard.
- Numba – @jit decorator for optimized compiler, which greatly increases execution time.

MATLAB was also used for:

- The prototype of the program,
- Data analysis and plotting.

A single iteration of the ADI algorithm takes $\mathcal{O}(N_1N_2)$ operations or simple $\mathcal{O}(N^2)$ by taking $N = N_1 = N_2$. A single iteration of the algorithm for the system of ODE takes $\mathcal{O}(N_2)$ operations as the number of calculations at each $j = 0, \dots, N_2 - 1$ is independent on N . Therefore, the complexity of the full algorithm is $\mathcal{O}(KN^2)$.

Table 1.3: Execution time of the full algorithm depending on the size of spatial mesh $N = N_1 = N_2$ and timestep mesh K . θ is the ratio between time of different grids. Tests were run on Intel Core i5-5200U CPU @ 2.20 GHz (2 cores), 8 GB RAM, 64-bit Windows OS machine.

Spatial mesh test			Timestep mesh test		
N	CPU time, min	θ_N	K	CPU time, min	θ_K
50	3.67		3500	3.85	
100	7.20	1.96	7000	7.44	1.93
200	14.93	2.07	14 000	15.16	2.04
400	33.64	2.25	28 000	29.75	1.96
800	78.49	2.33	56 000	59.96	2.02

However, computer simulations had shown, that actual computation time was almost linear according to N . According to Table 1.3, execution time increased only about 2 times ($\theta_N \approx 2$) while doubling the size of spatial grid in each simulation. It can be explained by efficient vector operations in NumPy, which may no longer work for some unrealistically large N . As expected, calculation time was linear according to K as $\theta_K \approx 2$.

1.5 Modelling and experimental results

1.5.1 Comparison of computer simulations and experimental results

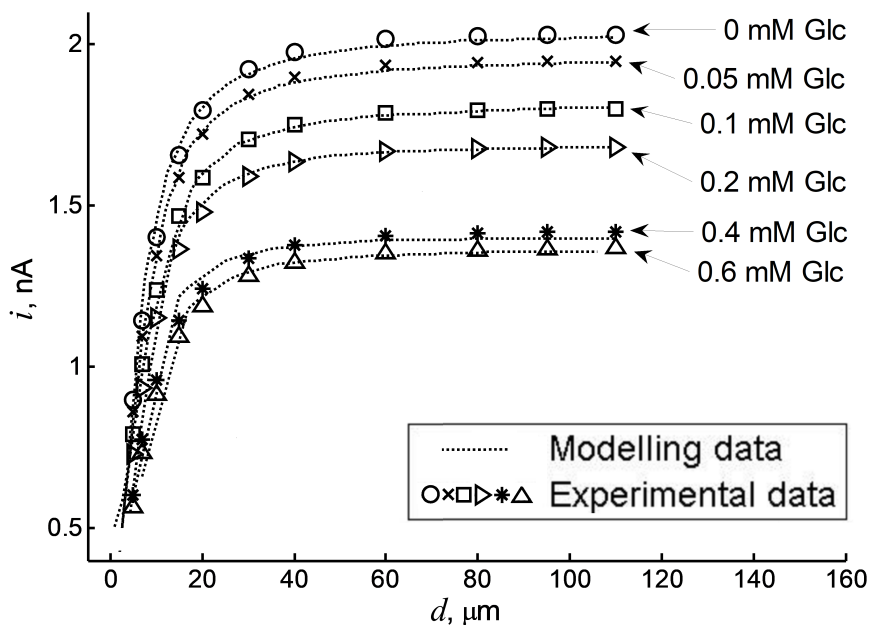


Figure 1.6: Current vs. distance dependencies, when different concentrations of glucose were added to the buffer solution.

The results of computer simulations were compared with real RC-SECM experiments (Fig. 1.6), which were conducted with 6 fixed values of glucose concentration: 0 mM (no enzymatic reaction), 0.05 mM,

0.1 mM, 0.2 mM, 0.4 mM and 0.6 mM. As expected, approach curves for higher concentrations of Glc were below curves of lower concentrations. This feature is the essence of the RC-SECM mode as O_2 consumption at the UME is slowed due to competition with O_2 consumption during the enzymatic reaction, which is faster for higher concentrations of Glc. Moreover, the adjustment of O_2 diffusion coefficient D_{O_2} also influenced the positions of approach curves and, in particular, the positioning of steady-state currents, i.e. the current, which is registered at the greatest distances from an active surface ($d \gtrsim 80 \mu\text{m}$). Because D_{O_2} decreased in the presence of a higher amount of Glc, the steady-state current, computed both by simulations and the experiment, was also lower.

As presented in Fig. 1.6, the modelling data coincided very well with the real physical experiment at steady-state distances, which was due to the calibration of experimental curves using the diffusion coefficient, adjusted to Glc concentration. It should be mentioned, that the calibration of experimental results is the typical procedure in post-experimental calculations because of high measurement errors and overall volatility of SECM experiments. However, the distance, at which steady-state current was reached in the model, was consistent with experimental data, which is attributed solely to good correspondence between the model and experiment.

At smaller distances d , where a sharp upturn of the electric signal is observed, the correspondence between the model and experimental data was slightly lower. It can be explained by measurement errors, the dependence on successful calibration for experimental results and the deviation of model assumptions at smallest distances ($d \lesssim 1 \mu\text{m}$) as new physical factors had to be contributed. In fact, the perfect electrode is represented by the mathematical model and the current would reach 0 at $d = 0$ (the UME touching the enzyme-modified surface), but that would not be the case with the imperfect real UME.

Overall, the results of computer and chemical experiments were considered coinciding very well.

1.5.2 Calculation of oxygen diffusion coefficient

According to the experimental data, displayed in Fig. 1.6, the diffusion-limiting current changed together with varying glucose concentrations. The concentration of oxygen (and UME current) in a zone, which was not affected by diffusion, was considered to be the same at all evaluated

glucose concentrations. However, the current is proportional not only to oxygen concentration but also significantly depends on the diffusion rate of oxygen through the solution. The oxygen diffusion coefficient depends on the presence and concentration of compounds, which are present in a buffer solution: salts (e.g. NaCl, KH₂PO₄, K₂HPO₄), glucose, etc. as demonstrated by Hébrard et al. [75]. Additionally, the same research has shown that the diffusion coefficient significantly depends on the glucose concentration in the solution, and it decreases at lower glucose concentration. Therefore, during the comparison of real experimental data with that generated using the proposed mathematical model, the diffusion coefficient was adapted for each evaluated glucose concentration.

We have tested the influence of diffusion on the current of the UME by the SECM experiment, which was performed on a bare surface without any immobilized enzyme at different glucose concentrations in the buffer solutions. The steady-state diffusion-controlled current is related to oxygen concentration when the UME-based probe is far from the surface [11], therefore the diffusion coefficient was calculated using the following formula:

$$D = \frac{i_{\text{exp}}}{4nFO_{2,\text{out}}r_{el}},$$

where i_{exp} is an experimentally measured steady-state current, $O_{2,\text{out}} = 253 \mu\text{M}$ – O₂ concentration in an exterior solution.

This experiment showed a noticeable decrease in observed diffusion coefficients compared to that observed in a buffer solution (Fig. 1.7A). The diffusion coefficient is one of the most significant parameters which is affecting UME current and the effect has to be taken into account in order to appropriately fit absolute current values, which were registered during the experiment. In the experiments, the buffer solution with 0.1 M of KCl with a particular concentration of glucose was used. $D_{O_2} = 2.29 \times 10^{-9} \text{ m}^2 \text{ s}^{-1}$ is the oxygen diffusion coefficient [126]. Other researchers found that the diffusion coefficient of oxygen separately depends on the concentration of glucose and NaCl in water [75]. Therefore, in this case, when glucose was added to a buffer solution containing several salts, it is obvious, that in this solution the diffusion coefficient of oxygen is more significantly affected by the composition of the solution. To determine the influence of glucose concentration on the diffusion coefficient in a buffer solution, the experiment was performed under the same conditions, but on the surface where the GOx was inactivated and oxygen was not consumed (Fig. 1.7A).

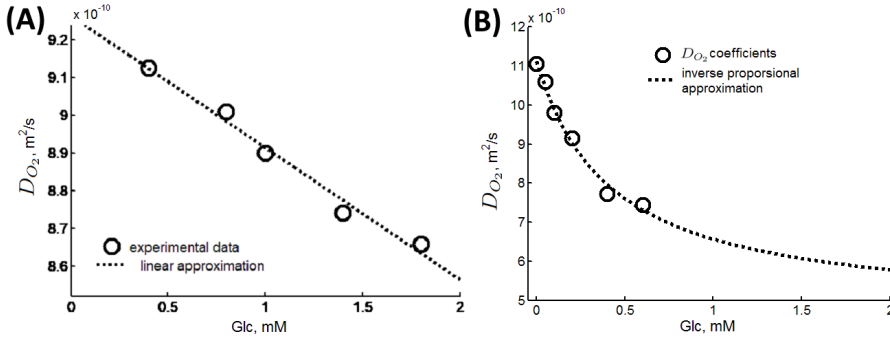


Figure 1.7: (A) Diffusion rate dependence on the concentration of glucose, which was added to the buffer solution. Measurements were performed at 0.5 cm distance from non-modified surface, i.e. without enzymatic reaction. (B) Diffusion rate dependence on the concentration of glucose, when chemical reactions on enzyme-modified surface happen. The oxygen diffusion coefficient D_{O_2} was calculated by fitting modelling results to the experiment.

The SECM-based evaluation of O_2 diffusion coefficient was performed on an enzyme-modified surface when enzymatic reaction was taking place. This experiment demonstrated that the diffusion coefficient of oxygen is almost the same in glucose concentration range of 0.4 – 0.6 mM (Fig. 1.7B), while measurements without enzymatic reaction show linear dependence of diffusion coefficient on glucose concentration in the range of 0.4 – 1.8 mM in Fig. 1.7A. According to the data, provided in Fig. 1.7B, it was determined that the O_2 diffusion coefficient is inversely proportional to the glucose concentration in the exterior solution, denoted Glc_{out} . The following formula was derived by fitting simulations data to the physical experiment and then by using the least-squares method to calculate coefficients:

$$D_{O_2} = 4.7 \times 10^{-10} + \frac{2.7 \times 10^{-10}}{Glc_{out} + 0.4}, \quad (1.42)$$

when the glucose concentration is measured in mM. Formula (1.42) was used in computer simulations of SECM, which were given in Fig. 1.6.

Mathematical models usually are fitted to experimental curves, which are representing normalized current vs. normalized distance. However, the diffusion of measured materials is not evaluated in such a case. The diffusion coefficients could be measured using the SECM

technique, therefore, in the mathematical model, different diffusion coefficients could be applied for different glucose concentrations using (1.42). Additionally, the research of different redox couples, such as oxidized/reduced ferrocene (Fc^+/Fc) or benzoquinone ($\text{BQ}/\text{BQ}^{\bullet-}$), and ferrocyanide/ferricyanide, showed that the UME current response in the SECM generation-collection mode is particularly sensitive to subtle differences in the diffusion coefficients of a redox couple [94]. In particular, the diffusion coefficient ratio of the oxidized and reduced forms of a couple can readily be determined by three methods: (i) by fitting the chronoamperometric UME current at a known distance between the UME and substrate; (ii) by combining measurements of the steady-state UME amperometric response at a known distance between the UME and substrate with that registered when the UME is positioned far from the substrate; (iii) by measuring the ratio of the steady-state feedback and UME current response at the generation-collection mode registered at the same distance between the UME and substrate [94]. Therefore, fitting unnormalized data to the model using different oxygen diffusion coefficient are also meaningful, because they demonstrated real UME currents.

1.6 Summary and conclusions

The mathematical model of SECM acting in the reduction-oxidation competition mode was presented for the first time in the literature. Using this model, it is possible to calculate oxygen consumption rate, evaluate enzymatic reaction kinetics, and determine oxygen diffusion coefficients in the medium of varying composition. It was shown that the data of computer simulations and real physical experiment agreed well after adjusting these parameters according to the model.

The modelling of the RC-SECM mode by taking into account diffusion-reaction kinetics showed that the main parameter influencing a steady-state diffusion-limited current signal is the diffusion coefficient. The diffusion coefficient is known to be different in solutions of different composition. Therefore, in biological systems varying salt and glucose concentrations are significantly affecting the diffusion coefficient of oxygen and other materials. For this reason, the UME signal can be significantly decreased due to this effect. The influence of varying diffusion coefficient could be evaluated by the proposed mathematical model.

SECM-based evaluations of enzyme-modified surfaces are very valuable for the development of enzymatic biosensors and biofuel cells. For example, the developed mathematical model can be further applied for the evaluation of the Michaelis constant calculated when the UME is located at different distances from the surface modified by an immobilised enzyme.

Chapter 2

Mathematical Modelling of the Influence of Ultramicroelectrode Geometry on Approach Curves Registered by Scanning Electrochemical Microscopy

2.1 Introduction

The goal of this research is to develop computational models to study the precision of SECM measurements with three different and most frequent types of defected UMEs: (i) recessed-UME, (ii) outwarded-UME, (iii) cone-UME. These electrodes are mathematically modelled by diffusion equation in various non-standard (non-rectangular) domains. Computer simulations of defected UMEs are compared with data obtained with not defected standard-UME to calculate measurement errors of SECM experiments performed with non-standard UMEs.

Measurement errors in SECM-based experiments

Scanning electrochemical microscopy (SECM) is a powerful tool for localized investigations and mapping of electrochemically active surfaces by scanning them with the ultramicroelectrode (UME) [74]. Electric signal (current), measured by SECM, is registered by an approach curve, which is obtained by the downward placement of the UME towards a substrate, i.e. by approaching a substrate.

However, SECM-based experiments are prone to high measurement errors. Approach curves should be adjusted because of the background current [44, 47, 54], electrode positioning challenges [96], variations in electrode geometry [3, 39], etc. UME should be carefully prepared and the geometry of the electrode should be determined before the measurement.

Variations in UME geometry, which is the main focus of the chapter, are caused by 2 major factors. Firstly, the fabrication of UMEs is still a very sophisticated and hand-crafted procedure, therefore, it is very hard to avoid significant deviation from an ideal shape of the UME. Secondly, the geometry of the UME changes every time, when the UME is polished or accidentally damaged by touching the surface of interest. These changes in UME geometry induce significant variations in electric current, measured by the UME. The simple and time-saving procedure to determine UME geometry and its deviation from the standard would be the comparison of experimental data with curves of a current, generated using a particular mathematical model.

Modelling the influence of UME geometry

Digital simulations were performed [3, 13, 86, 90, 98, 105, 120, 123, 138] to evaluate the influence of UME geometry on experimental results. Such simulations can solve some SECM measurement-related problems such as poor spatial resolution, the uncontrolled distance between the UME and surface of interest during SECM investigations and the effects of deviations from mathematically idealized SECM geometries on experimental data [123, 125].

The influence of UME geometry was theoretically investigated assuming that approach curves are registered in electrolyte with redox-mediators [3, 20, 39, 123, 124]. Simulations were performed for recessed-UME, which showed that the deviation of the amperometric response

can be significant depending on the recess depth [20]. Responses of both recessed and protruding (outwarded) electrodes were evaluated demonstrating especially for outwarded-UME that even small protrusion height can lead to a substantial deviation from a standard inlaid electrode [55]. The influence of tip geometry defects for steady-state currents at conical nanoelectrodes was investigated [88]. Approach curves were analysed over both electrically conducting and insulating substrates for conical electrodes [150, 151].

Some less frequent types of UME geometries were analyzed. Spherically-capped SECM tip formed by electrodepositing mercury drop onto UMEs were modelled and compared with experimental data [91]. It was determined that the diffusion around the edge of the insulating layer has a pronounced effect on the approach curves if SECM is acting in hindered diffusion or the positive feedback mode [3]. The positive feedback mode is mostly used for the calculation of kinetics by fitting mathematical models to experimentally obtained approach curves. The experiments have to be performed with electrodes with ideal geometry, otherwise, the fitting parameters, such as reaction rate constant, is not accurate.

Nonsymmetrical UMEs were simulated using the finite boundary method and the effects on approach curves in negative and positive feedback SECM were investigated [123]. The same authors investigated the multi-electrode based UME and simulations were performed in various generation-collection modes of SECM [124]. Several types of UME geometries, such as tilting, recessed-UME, off-centered UME and the UME with an elliptical conducting part were investigated [39]. In the same research, the influence of some UME parameters such as the radius of the conducting part of the probe and the relative size of the insulator surrounding the conducting part have been evaluated. During the monitoring of electrochemical activity of surfaces modified by biological materials the determination of consumed oxygen is often applied [47]. Therefore, for the investigation of biological materials, a general model that will improve the determination of UME geometry is required. This model should account for various unevenness of the conducting part of the UME and calculate the difference in measured approach curves from the ideal electrode.

Outline of the chapter

In this chapter, a mathematical model is developed to investigate several UME geometries: standard-UME, recessed-UME with a conducting part

recessed into the isolator, outwarded-UME with a sticking out conducting part and cone-UME with an outwarded cone-shaped conducting part. This research is targeted towards the study of biological systems without redox mediators and the advantage of the method is that it allows the simple detection of the geometry of the UME by registering oxygen in buffer solution by the negative feedback mode SECM.

In section 2.2, a short summary of an electrochemical experiment, which is used for validation of numerical experiments in section 2.5, is provided. Details of mathematical models are given in section 2.3 and their numerical solutions are explained in section 2.4. In section 2.5, results of numerical experiments are discussed. Conclusions of the chapter are made in section 2.6.

2.2 Experimental details

SECM and the disk-shaped Pt UME-based probe with radius $r_{el} = 114 \mu\text{m}$ from Sensolytics Ltd (Bochum, Germany) were used for experiments. The RG factor, which represents the ratio of the insulating part radius with the conducting part radius, i.e. $RG = r_{glass}/r_{el}$, was measured by an optical microscope and it was determined as 5.35 indicating that the radius of an insulator is $r_{glass} = 610 \mu\text{m}$. The active part of the UME is drawn inside by depth $H_{in} = 165 \mu\text{m}$ and this probe will be referred to as real recessed-UME used for SECM experiments in future references.

Before all measurements, the real recessed-UME was washed with 95 % ethanol solution and it was polished with polishing paper with a grain size of $0.3 \mu\text{m}$ and then the real recessed-UME was washed with buffer. The real recessed-UME quality was checked by cyclic voltammograms. A three electrode electrochemical setup was applied and, in this setup, the UME-based scanning probe was switched as a working electrode, Pt wire as a counter electrode and Ag/AgCl in 3M KCl (Ag/AgCl(3M KCl)) – as a reference electrode. Approach curves (Current vs distance dependencies) were registered at potential of -500 mV vs Ag/AgCl(3M KCl). The registration of approach curves was performed by moving the UME at $1 \mu\text{m/s}$ speed in a vertical direction. Then the UME-based probe was retracted to the distance, where the steady-state current is achieved. Approach curves were registered from that point while approaching the insulating surface in the negative feedback mode. Measurements were performed in phosphate-acetate buffer

with pH 6.6 and repeated three times. The mean value was used for further calculations.

2.3 Description of UME geometries and mathematical models

In subsequent sections, four different UME geometries are analysed: ideal standard plane UME which will be referred to as standard-UME; UME with a recessed conducting part (ref. as recessed-UME); UME with an outwarded conducting part (ref. as outwarded-UME); and UME with an outwarded cone-shaped conducting part (ref. as cone-UME). Mathematical models are provided for each type of the UME in separate sections alongside necessary formulas for the current computation.

2.3.1 Mathematical model for standard-UME

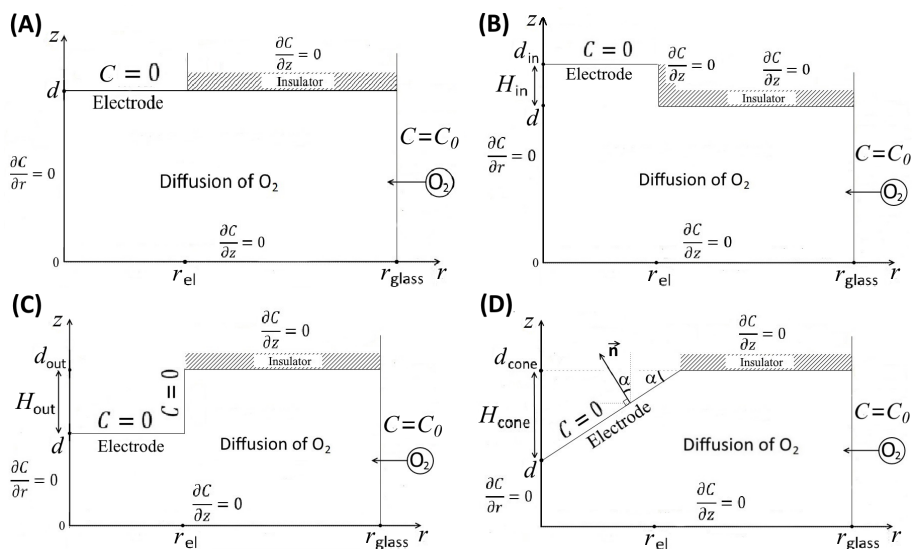


Figure 2.1: Schematic representations of simulation domains considered with boundary conditions, important parameters of UME geometry, etc. are given. (A) standard-UME, (B) recessed-UME with insertion depth H_{in} , (C) outwarded-UME with protrusion height H_{out} , (D) cone-UME with side angle α and normal direction derivative \vec{n} .

A simple rectangular domain in Fig. 2.1A is used to represent the geometry of standard-UME. Diffusion of oxygen is expressed by the second Fick's law in cylindrical coordinates system:

$$\frac{\partial C}{\partial t} = D_{O_2} \left(\frac{\partial^2 C}{\partial r^2} + \frac{1}{r} \frac{\partial C}{\partial r} + \frac{\partial^2 C}{\partial z^2} \right),$$

for $0 < t \leq T, 0 < z < d, 0 < r < r_{glass},$ (2.1)

where C is the O_2 concentration expressed as a function of time t and 2 spatial coordinates r and z . T is the duration of a computational experiment, d – distance from the surface to the tip, $r_{el} = 5 \mu\text{m}$ is the radius of the conducting part and $r_{glass} = 80 \mu\text{m}$ is the radius of the insulated part of the UME. The diffusion coefficient of oxygen in water D_{O_2} is $1.105 \times 10^{-9} \text{ m}^2/\text{s}$ [74].

At the beginning of the process the diffusion layer is fully saturated with oxygen and initial condition is

$$C = C_0 = 253 \mu\text{M} \quad \text{for } t = 0, 0 \leq z \leq d, 0 \leq r \leq r_{glass}. \quad (2.2)$$

All necessary boundary conditions are shown in Fig. 2.1A and are explained below. We consider the case without substrate hence there is no flow of oxygen on the surface $z = 0$:

$$\frac{\partial C}{\partial z} = 0, \quad \text{for } t > 0, z = 0, 0 \leq r < r_{glass}. \quad (2.3)$$

(2.4) is due to the assumption of radial symmetry to the central axis.

$$\frac{\partial C}{\partial r} = 0, \quad \text{for } t > 0, 0 \leq z \leq d, r = 0. \quad (2.4)$$

Constant intake of oxygen is assumed at the outer side of domain:

$$C = 253 \mu\text{M}, \quad \text{for } t > 0, 0 \leq z \leq d, r = r_{glass}. \quad (2.5)$$

There is no current flow on the insulator:

$$\frac{\partial C}{\partial z} = 0, \quad \text{for } t > 0, z = d, r_{el} < r < r_{glass}. \quad (2.6)$$

According to the applied model, all oxygen, which is reaches the interphase between the solution and conducting part is reduced:

$$C = 0, \quad \text{for } t > 0, z = d, 0 \leq r \leq r_{el}. \quad (2.7)$$

Finally, the current through the standard-UME is calculated using the formula

$$i(t) = 2\pi n F D_{O_2} \int_0^{r_{el}} \left. \frac{\partial C}{\partial z} \right|_{z=d} r dr, \quad (2.8)$$

where $n = 4$ is the number of electrons exchanged and the Faraday constant $F = 9.648 \times 10^4 \text{ A s mol}^{-1}$.

2.3.2 Mathematical model for the UME with a recessed conducting part

We have analysed the situation when the active (conducting) part is recessed by depth H_{in} into the insulating part of the electrode. The distance from the surface to the insulating part of recessed-UME is still d , but the distance between the surface of interest and the conducting part is $d_{in} = d + H_{in}$. This distance is always larger than d and thus in this situation the conducting part of recessed-UME is further away from the surface comparing to that when the conducting part and insulating part form an ideally shaped plane. The simulation domain in Fig. 2.1B consists of 2 connected rectangles: a larger one of height d is the same as for standard-UME in Fig. 2.1A and a smaller one of height H_{in} corresponds to the recessed part.

The diffusion equation (2.1), initial condition and boundary conditions (2.2)–(2.6) remain the same, but they are presented in the new domain as shown in Fig. 2.1B. The boundary condition for recessed-UME is

$$C = 0, \quad \text{for } t > 0, \quad z = d_{in}, \quad 0 \leq r \leq r_{el}. \quad (2.9)$$

On the recessed part at the insulator there is new no-flow condition:

$$\frac{\partial C}{\partial r} = 0, \quad \text{for } t > 0, \quad d \leq z \leq d_{in}, \quad r = r_{el}. \quad (2.10)$$

In order to compute the current, the equation similar to (2.8) is used

$$i(t) = 2\pi nFD_{O_2} \int_0^{r_{el}} \left. \frac{\partial C}{\partial z} \right|_{z=d_{in}} r dr. \quad (2.11)$$

2.3.3 Mathematical model for the UME with an outwarded conducting part

Outwarded-UME is modelled as conducting cylinder bulging out of the insulating part of the UME into the diffusion layer. There are 2 active parts of the conducting cylinder of outwarded-UME: the disc at the UME tip and the side of the cylinder, which is also in contact with the diffusion layer. It means that the active part of outwarded-UME has a larger surface area in comparison to the standard-UME, and this area depends on protrusion height H_{out} . In this situation, the distance between the surface of interest and outwarded-UME active surface remains d as for the standard-UME, but the distance from the surface to the insulating

part of outwarded-UME is increased to $d_{out} = d + H_{out}$. Again, it is always larger than d and even when d approaches 0 the diffusion to the outwarded-UME is not blocked because there is a flow of oxygen through the sides of outwarded-UME cylinder. The simulation domain is represented in Fig. 2.1C and consists of 2 connected rectangles.

Diffusion equation (2.1) and initial-boundary conditions (2.2)–(2.4), (2.6) remain the same as in the standard-UME with exceptions of new boundary condition for the side of the conducting part of outwarded-UME cylinder:

$$C = 0, \quad \text{for } t > 0, \quad d \leq z \leq d_{out}, \quad r = r_{el} \quad (2.12)$$

and for the insulator and outer side of domain which are by distance d_{out} from the surface

$$\begin{aligned} \frac{\partial C}{\partial z} &= 0, \quad \text{for } t > 0, \quad z = d_{out}, \quad r_{el} < r < r_{glass}, \\ C &= C_0 = 253 \mu\text{M}, \quad \text{for } t > 0, \quad 0 \leq z \leq d_{out}, \quad r = r_{glass}. \end{aligned} \quad (2.13)$$

The sum of two integrals is used for calculation of the tip current

$$i(t) = 2\pi nFD_{O_2} \int_0^{r_{el}} \left. \frac{\partial C}{\partial z} \right|_{z=d} r dr + 2\pi nFD_{O_2} r_{el} \int_d^{d_{out}} \left. \frac{\partial C}{\partial r} \right|_{r=r_{el}} dz. \quad (2.14)$$

The first integral represents the current flowing through the disc of the outwarded-UME tip, the same as in (2.8), while the second part is the current flowing through the side of the conducting cylinder and thus the integral is calculated as the current flow through the side area. It should be noted that even if the distance d approaches 0, the diffusion is still not blocked, and the current has a non-zero value close to the surface because the side of the conducting part is still contacting with the diffusion layer.

2.3.4 Mathematical model for the UME with an outwarded cone-shaped conducting part

The cone shape represents the situation when the UME is damaged and the conducting part of the electrode is brushing out. The UME containing sharp sticking parts is modelled by a single outwarded cone with one sharp tip, i.e. the apex of the cone. This single sticking part gives an idea about the properties of UMEs with a rough conducting

surface. This model is more complicated than the outwarded-UME model because an outwarded part is no longer rectangular.

The simulation domain in Fig. 2.1D is a rectangle with one cut-out corner representing the conducting part of the cone-UME. The side of the cone-UME makes angle α with its base. The distance between the surface and the apex of the cone is d and the distance from the surface to the insulator is $d_{cone} = d + H_{cone}$, where the height of the cone is $H_{cone} = r_{el}/\tan(\alpha)$. Clearly, an area of the conducting part is larger than for standard-UME and the surface does not reach the isolator even for $d = 0$, thus the cone-UME is expected to behave similarly to the outwarded-UME.

The same diffusion equation (2.1) and similar initial-boundary conditions (2.2)–(2.6) have been used as for the standard-UME. The boundary condition on the side of the conducting cone is

$$C = 0, \quad \text{for } t > 0, 0 \leq r \leq r_{el}, z = r \tan \alpha + d. \quad (2.15)$$

The direction of the current through the cone-UME is perpendicular to the side of the cone and thus normal direction derivative \vec{n} making angle α with r axis is used to compute direction of the current flow as shown in Fig. 2.1D. In this case, the current of cone-UME response is calculated by

$$i(t) = \frac{2\pi n F D_{O_2}}{\cos \alpha} \int_0^{r_{el}} \frac{\partial C}{\partial \vec{n}} r dr, \quad (2.16)$$

where division by $\cos \alpha$ is necessary, because $\frac{\pi r_{el}^2}{\cos \alpha}$ is the lateral area (i.e. side area) of the UME cone.

2.4 Numerical solution

2.4.1 Discrete grid

The boundary value problem, which describes the standard-UME model, had to be solved in a rectangular domain (Fig. 2.1A)

$$\Omega_{std} = \{(z, r) \in \mathbb{R}^2 : 0 < r < r_{glass}, 0 < z < d\}.$$

The differential equation, governing cone-UME, had to be solved in a trapezoid-shaped domain (Fig. 2.1D)

$$\begin{aligned} \Omega_{cone} = \{(z, r) : 0 < r \leq r_{el}, 0 < z < r \tan \alpha + d\} \cup \\ \cup \{(z, r) : r_{el} \leq r < r_{glass}, 0 < z < d_{cone}\}. \end{aligned}$$

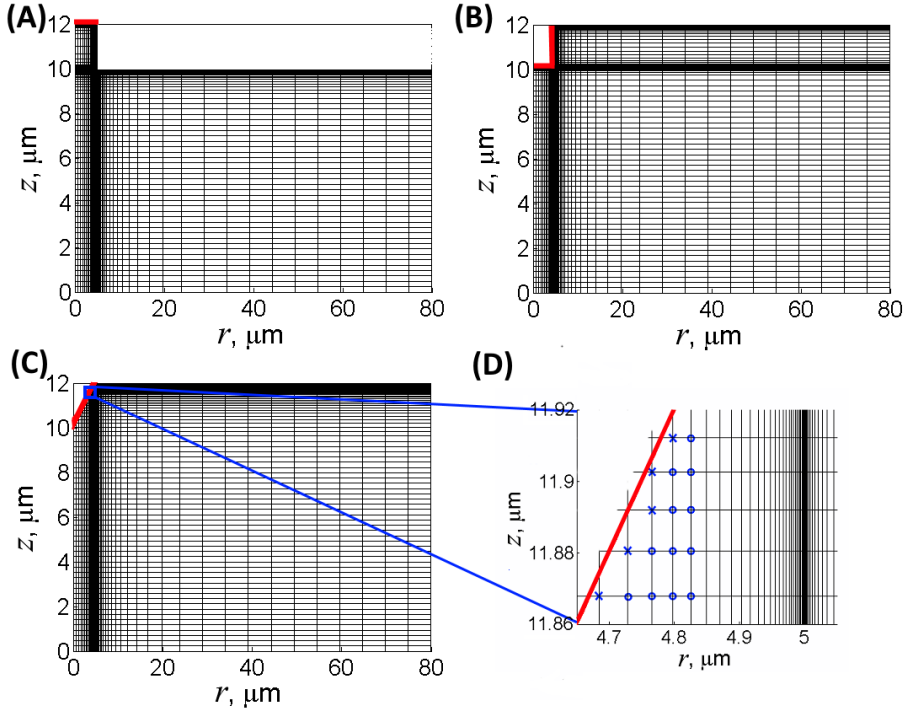


Figure 2.2: Mesh $\bar{\omega}_h \times \bar{\omega}_l$ of size 100×100 . The majority of mesh points cannot be seen as they are too close to the domains of compression. The red lines shows the electrode. (A) recessed-UME, (B) outwarded-UME, (C) cone-UME, (D) zoomed in part of cone-UME mesh. Inner points of the mesh are marked by blue circles, boundary points by blue crosses.

Both domains Ω_{std} and Ω_{cone} were discretised using non-uniform spatial mesh (Fig. 1.4 for standard-UME mesh, Fig. 2.2C for cone-UME) of size $N_1 \times N_2$:

$$\begin{aligned} \bar{\omega}_h &= \{z_i : z_i = z_{i-1} + h_i, i = 1, \dots, N_1, z_0 = 0, z_{N_1} = d\}, \\ \bar{\omega}_l &= \{r_j : r_j = r_{j-1} + l_j, j = 1, \dots, j_{\text{junc}}, \dots, N_2, \\ &\quad r_0 = 0, r_{j_{\text{junc}}} = r_{el}, r_{N_2} = r_{glass}\}, \\ \bar{\omega} &= \bar{\omega}_h \times \bar{\omega}_l, \end{aligned}$$

where h_i is a step size in z -direction, l_j – in r -direction, h_i and r_j – spatial coordinates at indexes i and j . In order to achieve higher accuracy at the UME, 50% of mesh points were allocated at the area below the

electrode, i.e. $r < r_{el}$, and, thus, junction point between the UME and insulator was always at fixed index $j_{\text{junc}} = 0.5N_2$. As shown in Fig. 2.2C, the mesh was exponentially compressed around the point $z = d_{\text{cone}}$ ($z = d$ for standard-UME) in z -direction and around the point $r = r_{el}$ in r -direction. Parameters of mesh growth/contraction were calculated by (1.16) and (1.17).

It should be noted that the precise location of boundary points of cone-UME mesh depends on UME geometry and mesh parameters (Fig. 2.2D) and had to be determined for each separate case.

In the case of recessed-UME, the boundary value problem had to be solved in cutout rectangular domain (Fig. 2.1B)

$$\Omega_{\text{rec}} = \{(z, r) : 0 < r \leq r_{el}, 0 < z < d_{in}\} \cup \{(z, r) : r_{el} \leq r < r_{\text{glass}}, 0 < z < d\}.$$

The mesh of domain Ω_{rec} was constructed using a similar method as in the previous case. It was assured that mesh point was placed at the height $z = d$ and index $i = i_{\text{in}}$ with the same goal as it was done at radius $r = r_{el}$ and index j_{junc} . The main difference from standard-UME was that the mesh $\bar{\omega}_h$ was exponentially compressed around 2 points (Fig. 2.2A): $z = d_{in}$ for greater accuracy at the UME and $z = d$ for greater accuracy at the bending point of domain Ω_{rec} , where larger flux (i.e. gradient) of oxygen was administered by SECM. Thirty percent of mesh points were allocated between d and d_{in} for robust calculations at the UME. $\bar{\omega}_h$ mesh was generated using method 2 (1.16) three times: (i) by growing mesh from d_{in} with parameters $n = 0.15N_1$, $m = 0$; (ii) then by contracting from the middle line between d_{in} and d and (iii) growing again from d down to 0 with parameters $n = 0.35N_1$, $m = 0.35N_1$.

In the case of outwarded-UME, the differential equation has to be solved in different cutout domain (Fig. 2.1C)

$$\Omega_{\text{out}} = \{(z, r) : 0 < r \leq r_{el}, 0 < z < d\} \cup \{(z, r) : r_{el} \leq r < r_{\text{glass}}, 0 < z < d_{out}\}.$$

The mesh of domain Ω_{out} (Fig. 2.2B) was chosen like in the case of recessed-UME by compressing the mesh around 2 points in z -direction. The mesh point was always assigned at the height $z = d$ with index $i = i_{\text{out}}$ and 50% of mesh points were allocated between d and d_{out} so that always $i_{\text{out}} = 0.5N_1$. Such a large number of points was necessary because in this case part of the UME was placed at the vertical border at $r = r_{el}$ and higher accuracy was required compared to recessed-UME

(the isolator was located there in the case of recessed-UME). Similarly to the case of recessed-UME, $\bar{\omega}_h$ mesh was generated using (1.16) three times with appropriate parameters n and m .

The initial-boundary value problem (2.1) had to be solved in domain $\Omega_T = [0, T] \times \Omega$, where T is modelling time, Ω is spatial domain in analysed geometries. It was determined that $T = 6$ s was enough to reach stable state in all geometries with observed parameters. Time interval $[0, T]$ was discretised by non-uniform time mesh

$$\bar{\omega}^\tau = \left\{ t^k : t^k = t^{k-1} + \tau_k, k = 1, \dots, K, t^0 = 0, t^K = T \right\}$$

and full mesh $\bar{\omega}^\tau \times \bar{\omega}$ was constructed. In the case of standard-UME and cone-UME, timestep parameter τ was set to 0.0001 for some starting points and later gradually increased to create time mesh of size $\sim 1.3 \times 10^4$. In the case of recessed-UME and outwarded-UME models, the size of $\bar{\omega}^\tau$ had to be substantially increased up to $\sim 2.6 \times 10^5$, because the stability of the solution was much lower. Spatial mesh of size 200×200 was used for all models.

The approximate solution at a mesh point (t^k, z_i, r_j) was denoted by $U_{i,j}^k$. The approximation of (2.1) and initial-boundary conditions will be detailed in the following sections.

2.4.2 Approximation of the boundary condition on the cone

The boundary condition (2.15) on the electrode of cone-UME has to be dealt with separately due to cone-UME difference from other geometries.

The cone-UME is represented by irregular curved domain Fig. 2.1D, which has to be approximated because the boundary line does not intersect with mesh points as shown in Fig. 2.2D. Inner points of the mesh (blue circles in Fig. 2.2D) are calculated by the regular formula. Boundary points (blue crosses in Fig. 2.2D), which are defined as having in their neighbourhood at least one point outside the mesh, have to be approximated using the boundary condition. While it is evidently possible to construct non-uniform mesh so all mesh points lie on the boundary line for fixed UME geometry, it is not preferable due to a couple of reasons:

1. Cone-UME geometry and notably its base angle α is the characteristic to be tested in this research. Different meshes for each

geometry would provide an additional computational error and potentially increase computational time.

2. Very small or large angles α may be tested by the model and automatically generated meshes would produce too small or too large space step.

The finite difference approximation of curved boundary condition is studied in literature for the Dirichlet type condition [50, 69, 73, 101] and Neumann type [107]. It should be noted that FD methods with irregular domains can still be used and stability properties persist, but the finite volume and finite element methods are necessary and more efficient when the domain becomes even more complex [84].

Value $U_{i,j}^{k+1}$ at boundary point (i, j) was calculated by the linear interpolation formula. When solving in z -direction, the following formula was used for each boundary points (i_0, j) (index i_0 is distinct for each column j):

$$\frac{U_{i,j}^{k+1} - U_{i-1,j}^{k+1}}{h_{i-1}} = \frac{\mu_{i,j} - U_{i,j}^{k+1}}{\sigma_j}, \quad i = i_0, \quad j = 0, \dots, j_{\text{junc}}. \quad (2.17)$$

Here, $\sigma_j \in [0, h_i]$ is vertical distance between boundary point (i, j) and boundary line $z = r \tan \alpha + d$ and is calculated for each column j . Boundary condition $\mu_{i,j}$ is always equal to 0 according to (2.16). More than one boundary point is included into some columns (see the middle column in Fig. 2.2D). In this case the first point (i_0, j) above inner points is approximated by (2.17) and interpolation in r -direction is applied for the rest of them:

$$\frac{U_{i,j+1}^{k+1} - U_{i,j}^{k+1}}{l_j} = \frac{U_{i,j}^{k+1} - \mu_{i,j}}{\sigma_{i,j}}, \quad i = i_1, \dots, i_m, \quad j = 0, \dots, j_{\text{junc}}, \quad (2.18)$$

where i_0, i_1, \dots, i_m are indexes of boundary points in a single column with fixed j , $(m + 1)$ is the number of boundary points in column j , and $\sigma_{i,j} \in [0, l_{j-1}]$ is the distance to the boundary line and boundary point (i, j) .

Formulas in r -direction are very similar:

$$\frac{U_{i,j+1}^{k+1} - U_{i,j}^{k+1}}{l_j} = \frac{U_{i,j}^{k+1} - \mu_{i,j}}{\sigma_i}, \quad i = i_{\text{cone}}, \dots, N_1 - 1, \quad j = j_0, \quad (2.19)$$

where j_0 is the index of the first boundary point in each line, $\sigma_i \in [0, l_{j-1}]$ is horizontal distance (distinct for each column i) between boundary point (i, j) and boundary line. In the case of multiple boundary points in the line, formulas similar to (2.18) are used.

2.4.3 Finite difference schemes

The initial-boundary value problem in all 4 different geometries was solved numerically using ADIFDM and similar techniques regarding discretization of the differential equation (2.1) and boundary conditions were used as in Chapter 1. The major difference is that non-standard geometries must be taken into account for models of recessed-UME, outwards-UME and cone-UME.

Schemes of the standard-UME model

In the case of standard geometry, equation (2.1) and boundary conditions (2.3)–(2.7) are the same as analysed in Chapter 1 with C_{Glc} set to 0, i.e. without reaction processes. Approximation formulas (1.20), (1.21), (1.23)–(1.25), (1.28)–(1.32) were used to solve equations in the standard-UME model. Specifically, (2.1) was approximated in the direction of r -axis at each fixed $i = 1, \dots, N_1 - 1$ by:

$$\begin{aligned} \frac{\bar{U}_{i,j} - U_{i,j}^k}{0.5\tau_k} &= \frac{D}{r_j l_{j+0.5}} \left(r_{j+0.5} \frac{\bar{U}_{i,j+1} - \bar{U}_{i,j}}{l_{j+1}} - r_{j-0.5} \frac{\bar{U}_{i,j} - \bar{U}_{i,j-1}}{l_j} \right) + \\ &+ \frac{D}{h_{i+0.5}} \left(\frac{U_{i+1,j}^k - U_{i,j}^k}{h_{i+1}} - \frac{U_{i,j}^k - U_{i-1,j}^k}{h_i} \right), \\ & j = 1, \dots, N_2 - 1, \quad (2.20) \end{aligned}$$

where

$$\begin{aligned} r_{j+0.5} &= \frac{r_j + r_{j+1}}{2}, & r_{j-0.5} &= \frac{r_{j-1} + r_j}{2}, \\ h_{i+0.5} &= \frac{h_i + h_{i+1}}{2}, & l_{j+0.5} &= \frac{l_j + l_{j+1}}{2}. \end{aligned}$$

Unknown value is $\bar{U}_{i,j}$ in (2.20) for r -direction. In the direction of z -axis at each fixed $j = 1, \dots, N_2 - 1$ equations were used:

$$\begin{aligned} \frac{U_{i,j}^{k+1} - \bar{U}_{i,j}}{0.5\tau_k} &= \frac{D}{r_j l_{j+0.5}} \left(r_{j+0.5} \frac{\bar{U}_{i,j+1} - \bar{U}_{i,j}}{l_{j+1}} - r_{j-0.5} \frac{\bar{U}_{i,j} - \bar{U}_{i,j-1}}{l_j} \right) + \\ &+ \frac{D}{h_{i+0.5}} \left(\frac{U_{i+1,j}^{k+1} - U_{i,j}^{k+1}}{h_{i+1}} - \frac{U_{i,j}^{k+1} - U_{i-1,j}^{k+1}}{h_i} \right), \\ & i = 1, \dots, N_1 - 1, \quad (2.21) \end{aligned}$$

where $U_{i,j}^{k+1}$ is an unknown value for z -direction.

Boundary conditions were approximated by separately devised methods as explained in (1.21)–(1.25), (1.32). At each timestep t^{k+1} difference equations were first solved in r -direction and then in z -direction using the Thomas algorithm [113].

Schemes of the recessed-UME model

Considering the recessed-UME model, the upper-right part of analyzed rectangular domain (Fig. 2.1B) does not belong to the domain of solution. The cutout rectangle starts at height $z = d$, index i_{in} and radius $r = r_{el}$, index j_{junc} . Approximation formulas had to adjusted as explained in this subsection.

While solving in the direction of r -axis, (2.1) was approximated at each fixed $i = 1, \dots, i_{\text{in}} - 1$ by (2.20) and at each $i = i_{\text{in}} + 1, \dots, N_1 - 1$ by

$$\begin{aligned} \frac{\bar{U}_{i,j} - U_{i,j}^k}{0.5\tau_k} &= \frac{D}{r_j l_{j+0.5}} \left(r_{j+0.5} \frac{\bar{U}_{i,j+1} - \bar{U}_{i,j}}{l_{j+1}} - r_{j-0.5} \frac{\bar{U}_{i,j} - \bar{U}_{i,j-1}}{l_j} \right) + \\ &+ \frac{D}{h_{i+0.5}} \left(\frac{U_{i+1,j}^k - U_{i,j}^k}{h_{i+1}} - \frac{U_{i,j}^k - U_{i-1,j}^k}{h_i} \right), \\ & j = 1, \dots, j_{\text{junc}} - 1. \end{aligned} \quad (2.22)$$

Additionally, the boundary condition (2.10) was approximated by formula similar to (1.23) in order to derive difference equation at each here considered i and $j = j_{\text{junc}}$. Finally, at index $i = i_{\text{in}}$, i.e. at the junction point between the main domain and the recessed part of the UME, approximation (2.22) was used until $j = j_{\text{junc}}$ and from index j_{junc} boundary condition (2.6) had to be incorporated using (1.24).

While solving in the direction of z -axis, (2.1) was approximated at each fixed $j = i, \dots, j_{\text{junc}} - 1$ by (2.21) and at each $j = j_{\text{junc}} + 1, \dots, N_2 - 1$ by

$$\begin{aligned} \frac{U_{i,j}^{k+1} - \bar{U}_{i,j}}{0.5\tau_k} &= \frac{D}{r_j l_{j+0.5}} \left(r_{j+0.5} \frac{\bar{U}_{i,j+1} - \bar{U}_{i,j}}{l_{j+1}} - r_{j-0.5} \frac{\bar{U}_{i,j} - \bar{U}_{i,j-1}}{l_j} \right) \\ &+ \frac{D}{h_{i+0.5}} \left(\frac{U_{i+1,j}^{k+1} - U_{i,j}^{k+1}}{h_{i+1}} - \frac{U_{i,j}^{k+1} - U_{i-1,j}^{k+1}}{h_i} \right), \\ & i = 1, \dots, i_{\text{in}} - 1. \end{aligned} \quad (2.23)$$

At index $j = j_{\text{junc}}$, i.e. at the junction of the UME and the insulator, approximation (2.22) was used until $i = i_{\text{in}}$ and approximation of boundary condition (2.10) was used from $i = i_{\text{in}}$ upwards. All other boundary-initial conditions were approximated as usual.

Schemes of the outwarded-UME model

In the case of outwarded-UME, the upper-left corner is removed from the modelled domain (2.1C). The additional rectangular domain is added from height $z = d$, index i_{out} and radius $r = r_{\text{el}}$, index j_{junc} . Approximation formulas had to be adjusted in the similar manner as in the case of recessed-UME.

In the direction of r -axis, (2.20) was applied at each fixed $i = 1, \dots, i_{\text{out}} - 1$. Meanwhile, at each fixed $i = i_{\text{out}}, \dots, N_1 - 1$, (2.20) was adjusted to calculate unknown $\bar{U}_{i,j}$ from index $j = j_{\text{junc}} + 1$ to $j = N_2 - 1$, i.e. only for necessary indexes, and boundary condition (2.12) was used to set $\bar{U}_{i,j_{\text{junc}}} = 0$.

In the direction of z -axis, at each fixed $j = 1, \dots, j_{\text{junc}}$, (2.21) was adjusted to calculate unknown $U_{i,j}^{k+1}$ for indexes $i = 1, \dots, i_{\text{out}} - 1$ and at index $j = 0$ approximation (1.32) of boundary condition (2.4) was adjusted accordingly. Finally, at each fixed $j = j_{\text{junc}} + 1, \dots, N_2 - 1$, (2.21) was used.

Schemes of the cone-UME model

After approximating the boundary condition on the electrode (2.15) in section (2.4.2), deriving finite difference schemes for cone-UME is relatively straightforward and similar to the case of outwarded-UME. An additional trapezoid-shaped domain is added from height $z = d$, index i_{cone} and diagonal side of trapezoid is described by line $z = r \tan \alpha + d$.

While solving in the direction of r -axis, (2.20) was applied at each fixed $i = 1, \dots, i_{\text{cone}}$ and (2.20) was adjusted to start calculations from $j = j_n + 1$ at each row $i = i_{\text{cone}} + 1, \dots, N_1 - 1$, where j_n is the index of the rightmost boundary point in each row i .

While solving in the direction of z -axis, at each fixed $j = 1, \dots, j_{\text{junc}} - 1$, (2.21) was adjusted to calculate from index $i = 1$ to $i = i_m - 1$, where i_m is the index of the lowest boundary point in each column j and at each fixed $j = j_{\text{junc}}, \dots, N_2 - 1$, (2.21) was used.

Calculation of SECM response

After solving difference equations for each geometry, SECM response (2.8), (2.11), (2.14) and (2.16) had to be calculated in order to compare with experimental data and to present modelling results. Derivatives in these formulas were approximated using polynomial interpolation as in (1.39) and (1.40). Additionally, partial derivatives in r -direction were calculated for (2.14) and (2.16). The trapezoid rule was used to approximate integrals and formulas similar to (1.41) were derived.

For comparison with experimental data, only the steady-state current was important and it was determined that modelling time $T = 6$ s was sufficient time to reach the stable current in all geometries. Then, approach curve $i_{\text{approach}}(d)$ was obtained by calculating the steady-state current at varying height d , i.e. by approaching surface at $d = 0$. Approach curves are the output of SECM related experiments and, therefore, are the key result in SECM modelling.

2.4.4 Implementation details

The program code was implemented in Python with NumPy library using

- Libraries and techniques as explained in the previous chapter (section 1.4.5).
- Multiprocessing library for parallelizing computations using the HPC resources provided by the Faculty of Mathematics and Informatics of Vilnius University. Multiple processes were spawned for sets of model parameters, which include the distance d , the size of defect (H_{in} , H_{out} or H_{cone}) and RG factor (ratio r_{glass}/r_{el}). Due to the perfectly parallel nature of independent computer simulations, a lock synchronization mechanism was sufficient to ensure that processes do not override results while returning the output.

Data analysis and plotting were performed in MATLAB.

2.5 Results and Discussion

2.5.1 Comparison of experimental data and mathematical modelling results

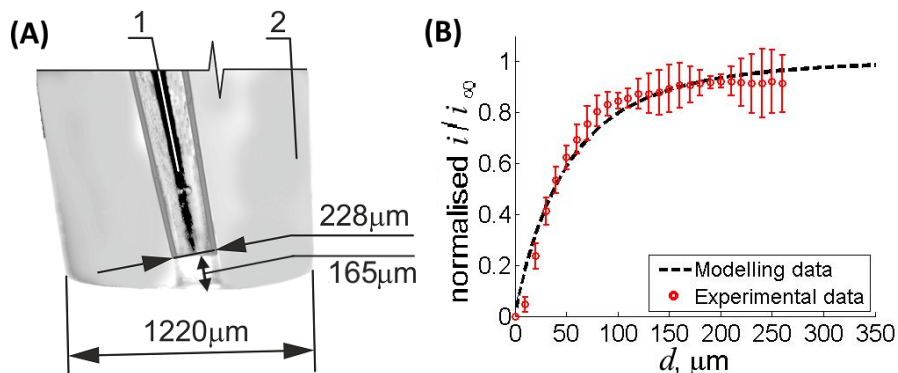


Figure 2.3: (A) Real recessed-UME image. No.1 denotes active part of the UME and No.2 is isolator. The size parameters of the UME and recess depth are shown on the image. (B) Comparison of steady state currents for experimental and modelling data using the UME shown in Fig. 2.3A ($r_{el} = 114 \mu\text{m}$, $r_{glass} = 610 \mu\text{m}$, $H_{in} = 165 \mu\text{m}$, applied potential -500 mV). Error bars show standard deviation for each experimental data point, which on average is ± 0.067 .

The approach curve for recessed-UME was computed using a mathematical model and compared with the experimentally obtained data using real recessed-UME represented in Fig. 2.3A. Data shows good correspondence for lower d values as shown in Fig. 2.3B. Difference increases for larger d values, this effect can be related to larger experimental errors (see error bars in Fig. 2.3B). Higher error bars at larger d values are attributed to the difficulty of achieving stable currents for the real recessed-UME for which the recess depth $H_{in} = 165 \mu\text{m}$ is considerably large compared to the radius $r_{el} = 114 \mu\text{m}$. Thus, these experimental difficulties are expected for such significant deviations from standard-UME.

A successful comparison shows that models of different geometries are compatible with real UMEs, which motivates the application of other models. Therefore, UME radius $r_{el} = 5 \mu\text{m}$ and RG factor 16 was used for further modelling.

2.5.2 Influence of UME geometry on approach curves

Approach curves in the negative feedback mode were modelled for UME with different geometries: recessed-UME (Fig. 2.4A,D,G), outwarded-UME (Fig. 2.4B,E,H), cone-UME (Fig. 2.4C,F,I) and compared with standard-UME. For each electrode, approach curves are presented with three different depths/heights/cone angles of conducting parts, when the current is: (i) absolute (Fig. 2.4A,B,C); (ii) normalised by diffusion-limited currents (Fig. 2.4D,E,F); (iii) normalised with subtracted background currents (Fig. 2.4G,H,I).

For recessed-UME, the absolute current decreases compared to the current of standard-UME (Fig. 2.4A). This can be explained by the fact that it is more difficult for oxygen to reach the conducting part of recessed-UME than in standard-UME case because the turning point of the isolator reduces the diffusion of all materials including oxygen. This effect has a more significant influence on the absolute current when the recession H_{in} is increasing. According to modelling results, a concentration gradient is greatest at the turning point (see section 2.5.4 Analysis of isolines) and with increasing recess depth H_{in} the gradient flattens further near the conducting part and then a lower current is observed. For example, the absolute current is 1.8 nA in recessed-UME case with 1 μm depth, and 0.8 nA with 5 μm depth.

On the other hand, approach curves for the outwarded-UME in Fig. 2.4B grow rapidly with increasing H_{out} . This is due to oxygen diffusion both to the side and the bottom of the conducting part of outwarded-UME. Thus, the conducting area of outwarded-UME is much larger than for standard-UME. In fact, the actual conducting part of outwarded-UME at the bottom of UMEs tip plays a less important role in oxygen consumption than the side of UMEs tip as further explained in the section 2.5.4.

In the case of cone-UME, absolute currents increase with a higher side angle as shown in Fig. 2.4C. The conducting area of the cone-UME is larger for higher angles, which results in a greater total current. Though the increase is not expected to be linear because the direction of normal derivative \vec{n} (depicted in Fig. 2.1D) also changes, i.e. approach curve Fig. 2.4C is influenced both by increasing active area of the UME and changing the direction of oxygen flow.

The diffusion-limited current depends proportionally on the surface area of the UME conducting part. Therefore, by increasing the surface area, the diffusion-limited current also increases, as it is shown in Fig.

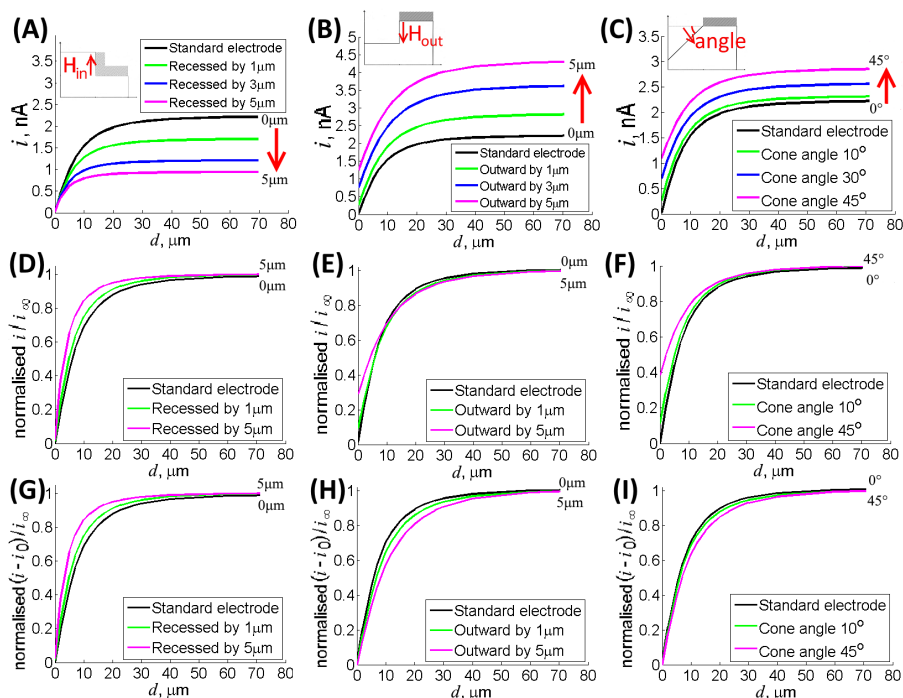


Figure 2.4: Left column: recessed-UME; middle column: outwarded-UME; right column: cone-UME. Top row: the steady state current dependency on d for varying levels of UME geometrical shapes compared with the current for standard-UME. Schemes in the corners of each Fig. (A), (B), (C) show which parameter is changed and the red arrows demonstrate direction of the change. Middle row: normalised currents i/i_{∞} , where i_{∞} is the steady state current with maximum distance concerned. Bottom row: normalised currents $(i - i_0)/i_{\infty}$, with the starting point of all curves moved to point 0 and then normalised. UME parameters are $r_{el} = 5 \mu\text{m}$, $r_{glass} = 80 \mu\text{m}$ in all figures.

2.4B,C. The decrease in the diffusion-limited current was observed in the case of recessed-UME. In this case, the diffusion to the conducting part of recessed-UME is more complicated. Therefore, the diffusion-limited current decreases when the conducting part of recessed-UME is deeper recessed within an insulating layer of the UME. Fitting mathematical models to experimental data is usually performed by comparing normalised currents, which are shown in Fig. 2.4D,E,F. In this case, recessed-UME generates 0 current at $d = 0$, because the diffusion is entirely blocked by the insulating part of recessed-UME. The depth

H_{in} of the recessed conducting part of the UME determines the behaviour of approach curves, which is similar to that registered during the electrochemical processes, where the kinetic constant of electrochemical reaction at the surface of interest is increased. It means that in the case of recessed-UME this difference will provide incorrect information about reaction kinetics. Therefore, the tendency of the approach curve in Fig. 2.4D, which represents the normalised recessed-UME current vs distance, is very similar to that obtained by standard-UME, only signal saturation rate is much higher in the case of recessed-UME. Fitting such experimental data should be made by taking into account this phenomenon.

On the contrary, the tendency of approach curve in Fig. 2.4E, which represents the normalised outwarded-UME current vs distance, is very different from that obtained by standard-UME, because the line starts at a certain current which is predetermined by protrusion height H_{out} and in addition the slope of the curve is lower in comparison with that of standard-UME. The last effect is determined by the absence of an insulating layer close to the surface of interest. When the conducting part of the UME is outwarded by height H_{out} less than $1\ \mu\text{m}$, the difference from the current from that of standard-UME is not significant. The situation changes when the conducting part is outwarded more than $5\ \mu\text{m}$. When approaching the surface with such outwarded-UME, the current will be not equal to zero even if the conducting part of the UME touches the surface of interest. Therefore, by attempting to approach the surface in such a way that the outwarded-UME current will decrease to zero, which is the standard procedure to determine the distance from approach curves, the probe and/or the surface of the sample can be damaged. Such dimensions of UME defect are not observable by optical microscopy and can be determined only by fitting the model to experimentally obtained approach curves. The proposed mathematical model can help to determine UME geometry and to calculate the actual zero distance which is crucial in SECM experiments.

The cone-UME (Fig. 2.4C,F) simulates the case when the UME has a defect on the conducting part which is sticking out from the UME. In some cases, the damage of the insulating and conducting parts of the electrode can induce an effect very similar to that of outwarded-UME. In such a case the decrease of the steady-state current down to 0, when the distance is 0 is not possible even if the conducting part of the conic-UME is touching the surface of interest. At the distances very close to the surface of interest the currents simulated with cone-UME are higher comparing to those registered by outwarded-UME.

The normalised approach curves can be additionally corrected by the elimination of the background current (Fig. 2.4G,H,I). This correction provides some additional insights: approach curves of recessed-UME are identical to that obtained without correction because in this case, background currents of recessed-UME and standard-UME are similar. When the background current is eliminated from approach curves simulated for outwarded-UME, the slopes of curves decrease by the increase of height H_{out} as shown in Fig. 2.4H. For conic-UME, the slopes of curves also decrease by the increased height H_{cone} of the conducting part (Fig. 2.4I). This elimination allows us to distinguish recessed-UMEs from outwarded-UMEs and conic-UMEs.

The shape of approach curves can be indicated by the SECM user as the variation of diameters ratio of the insulating and conducting parts of the UME (RG factor), but this interpretation could be wrong if the UME is of non-ideal shape. For example, if the conducting part of the electrode is recessed, the user evaluates the approach curve and decides that RG of an electrode is lower, but actually the depth $H_{in} = 5 \mu\text{m}$ is higher, and RG factor stays the same as in standard-UME case (Fig. 2.4D,G). This leads to an incorrect interpretation of measured results. Such miscalculations are possible because the behaviour of recessed-UME, which is recessed by depth $H_{in} = 5 \mu\text{m}$, shows lower imaginary RG factor than that for standard-UME. E and F parts of Fig. 2.4 do not show any influence on imaginary RG factor. H and I parts show lower imaginary RG if the conducting part of the electrode is recessed more deeply. In most cases, the RG factor is determined by an optical microscope before measuring. However, small recess depths, outwards heights and/or some other irregularities cannot be easily determined experimentally from approach curves and well-observed by optical microscopy. Therefore, the proposed fitting of the mathematical model with the results of approach curves will provide a tool for the determination and correction of inaccuracies of the RG factor, determined by optical microscopy.

Maximum difference for approach curves between non-standard UMEs and standard-UME were calculated using the formula:

$$Difference = \frac{\max_d \left(I(d) - I_{plane}(d) \right)}{\max_d \left(I_{plane}(d) \right)} \cdot 100 \%, \quad (2.24)$$

where I is approach curves of non-standard UME with varying parameter H_{in} , H_{out} or angle α and I_{plane} is the curve of standard-UME.

By comparing the difference in a current response between non-standard UMEs and standard-UME (Fig. 2.5), we conclude that the

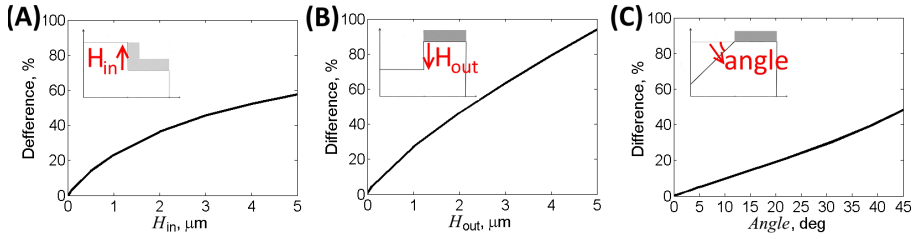


Figure 2.5: Differences between non-standard UMEs and standard-UME. The variable parameter for each type of the UME is shown in the scheme for each Fig. (A) recessed-UME, (B) outwarded-UME, (C) cone-UME.

highest difference is for outwarded-UME and reaches almost 100%. Maximal difference for recessed-UME is 60% with retraction depth $H_{in} = 5 \mu\text{m}$ for $5 \mu\text{m}$ radius UME. For cone-UME it is 50% at cone angle 45° , which corresponds to the same cone's protrusion height $H_{cone} = 5 \mu\text{m}$. In practice, if the UME is partly damaged, in most of the cases the insulating part contains cracks and cavities. If this break is very small, it cannot be seen by optical microscopy and thus the evaluation using the model becomes necessary. Even if the protrusion height H_{out} is only 2 – 5 μm for electrode radius $r_{el} = 5 \mu\text{m}$ used for modelling, this already provides 40% – 100% difference from standard-UME for registered signal.

Table 2.1: Dimensionless parameters of non-standard UME geometries that provide following differences from standard-UME approach curve. The UME with $r_{el} = 5 \mu\text{m}$, $r_{glass} = 80 \mu\text{m}$ was used to calculate data.

Difference from standard-UME	5 %	10 %	25 %	50 %
Recess depth H_{in}/r_{el}	0.034	0.075	0.225	0.745
Protrusion height H_{out}/r_{el}	0.027	0.064	0.186	0.438
Cone height H_{cone}/r_{el}	0.090	0.184	0.488	1.042

Fig. 2.5 can be used to calculate insertion depths and protrusion heights of non-standard UME that provides difference of 5%, 10%, 25% and 50% from standard-UME. This information is useful to determine UME suitability for SECM-based experiments by testing when the measurement error becomes bigger than desired. Dimensionless parameters of UME geometries were calculated by cubic approximation of data in Fig. 2.5 and presented in Table 2.1. Dimensionless parameters representing ratio with UME radius r_{el} were chosen so data can be used

for various sizes of the UME active part and it is standard procedure in SECM modelling [93]. Protrusion height for outwarded-UME is the smallest parameter to achieve given difference from standard-UME indicating that SECM with outwarded-UME is the most sensitive for measurement errors.

2.5.3 Influence of the RG factor on approach curves

Recessed-UMEs were modelled with different RG factors by changing the insulating part of electrodes. The conducting part of UME remains the same, therefore, the results did not change for all modelled RGs as was expected (Fig. 2.6A,B,C). By comparing normalized results (Fig. 2.6D,E,F) it was observed that at higher RG the behaviour of approach curves changes more significantly: the same value of the diffusion-limited current for $RG = 32$ is achieved at $30 \mu\text{m}$ distance using standard-UME, and at $15 \mu\text{m}$ distance using electrode recessed by $5 \mu\text{m}$ (Fig. 2.6F). The same effect is observed in Fig. 2.6G,H,I where the background current is eliminated. To determine the effect of RG, we plotted approach curves for varying RG factors when geometry in each scheme is fixed (Fig. 2.7). Significant difference between standard-UME and recessed-UME approach curves can be seen: the diffusion-limited current for standard-UME at $RG = 4$ is 2.5 nA ; while for recessed-UME it is 1.3 nA and 1 nA at $3 \mu\text{m}$ and $5 \mu\text{m}$, respectively.

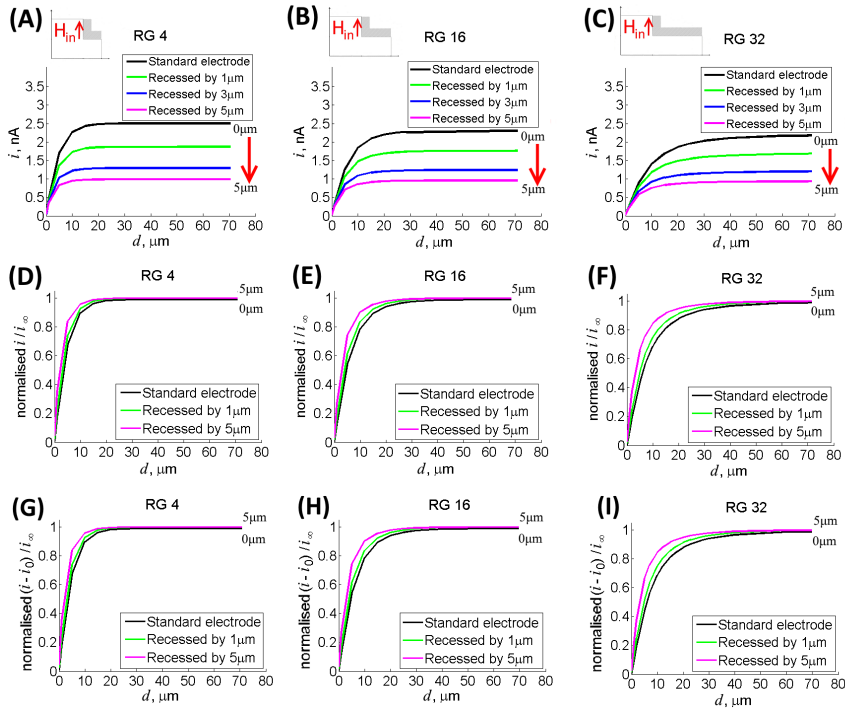


Figure 2.6: Approach curves for recessed-UME and varying RG factors in different columns. Top row: Steady state current dependency on d for varying recess depth. Schemes in the corners of each Fig.(A), (B), (C) show an approximate size of the electrode for the particular RG factor and red arrows demonstrate direction of angle change. Middle and bottom row: currents normalised with different methods. In all cases, electrodes radius $r_{el} = 5 \mu m$. Left column $r_{glass} = 20 \mu m$, middle column $r_{glass} = 80 \mu m$ (the value used everywhere else in the thesis), right column $r_{glass} = 160 \mu m$.

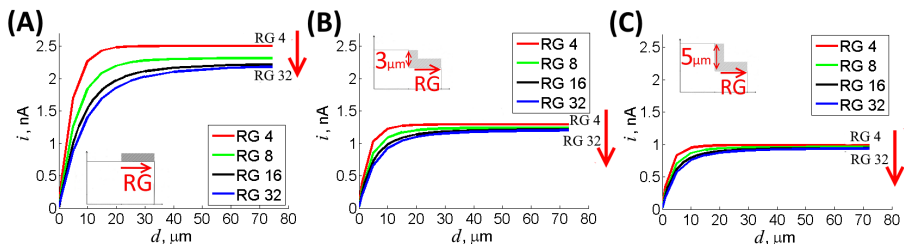


Figure 2.7: Approach curves for varying RG factors when the geometry, i.e. recess depth, is fixed in each figure: (A) standard-UME, (B) Recessed-UME with depth $3 \mu m$, (C) Recessed-UME with depth $5 \mu m$. Schemes in the corners of each figure show an approximate size of the electrode.

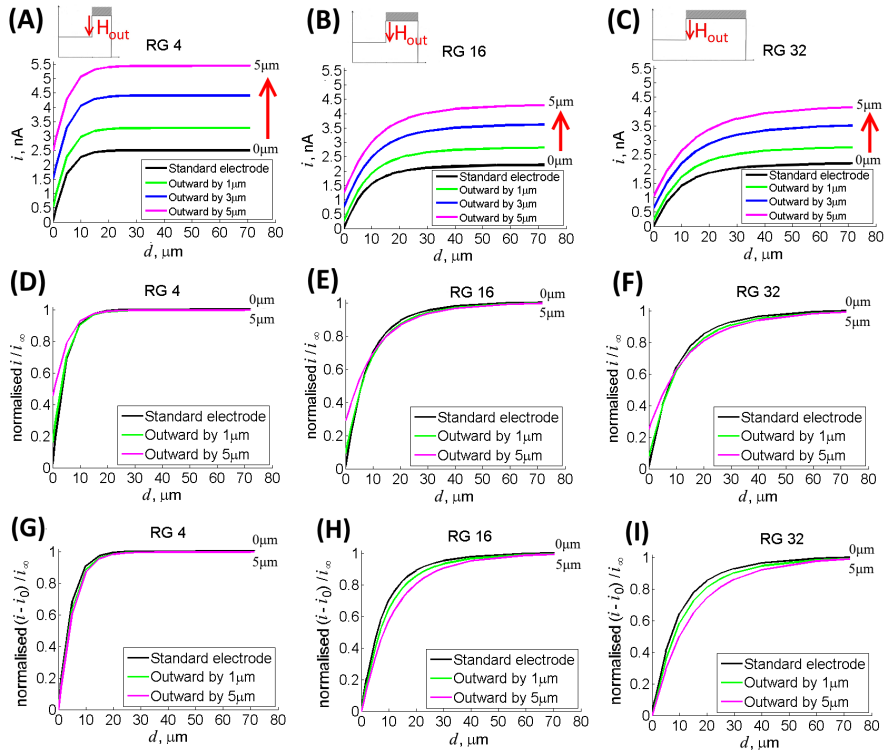


Figure 2.8: Approach curves for outwarded-UME and varying RG factors in different columns. Top row: Steady state current dependency on d for varying outward height. Middle and bottom row: currents normalised with different methods. Left column $r_{glass} = 20 \mu\text{m}$, middle column $r_{glass} = 80 \mu\text{m}$, right column $r_{glass} = 160 \mu\text{m}$.

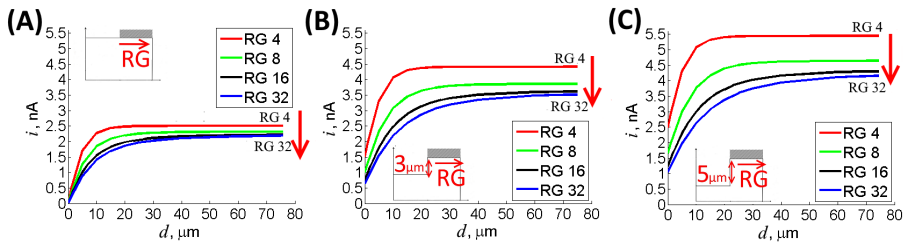


Figure 2.9: Approach curves for varying RG factors and different outward height: (A) standard-UME, (B) Outward-UME with height $3 \mu\text{m}$, (C) Outwarded-UME with height $5 \mu\text{m}$.

Outwarded-UME have high influence on RG factor: the diffusion-limited current was 5.5 nA , 4.4 nA and 4 nA for $\text{RG} = 4$, $\text{RG} = 16$ and $\text{RG} = 32$, respectively, when outward height was $5 \mu\text{m}$ (Fig. 2.8A,B,C). The normalised current at zero distance for $\text{RG} = 4$ is 0.44 , while for

RG = 16 and RG = 32 the normalised current reaches 0.3. By comparing approach curves for varying RG factors then the geometry in each scheme is fixed, it was observed that the diffusion-limited current is increasing together with outward height: the current is 2.5 nA, 4.5 nA and 5.5 nA with standard, 3 μm and 5 μm outwarded-UME, respectively, when RG is 4 (Fig. 2.9).

Concerning cone-UME, the results (Fig. 2.10A,B,C) show that the diffusion-limited current is the highest on cone-UME with the lowest RG = 4 factor. Moreover, it changes by increasing the cone a little bit more than using RG = 16 and RG = 32. RG = 4 current changed from 2.4 nA for standard-UME to 3.4 nA for cone angle 45°; while at RG = 16 current values are 2 nA and 2.9 nA; for RG = 32 current values are 2.1 nA and 2.8 nA. Thus, if we use cone-UME with RG = 4 the absolute difference is 1 nA, for RG = 16 it is 0.9 nA, and for RG = 32 – 0.7 nA. When the current was normalized (Fig. 2.10D,E,F), we obtained that at zero distance the normalized current is not equal to zero: at RG = 4 and cone angle 45° the current is 0.6 nA, while at RG = 16 it is 0.4 nA, and at RG = 32 – 0.35 nA. The current at zero distance did not reach zero because diffusion was not blocked as in the case of standard-UME. If the conducting part of the UME is outwarded, the diffusion should be blocked only by surface of interest when the UME is close to the surface. However, from data gathered using the mathematical model it was observed that the geometry of the insulating part is also important. When RG = 4, at 10 μm distance the increase of the current was observed.

The approach curves at three different cones were shown in Fig. 2.11. The RG factor's influence on cone-UME show low difference between RG factors in the case of standard-UME (Fig. 2.11A): $i = 2$ nA for RG = 32 and $i = 2.5$ nA for RG = 4. Increase in RG show higher differences (Fig. 2.11B,C) when cone angle is 30°: $i = 2.4$ nA for RG = 32, and $i = 2.9$ nA for RG = 4. For cone angle 45° currents are $i = 2.6$ nA for RG = 32 and $i = 3.4$ nA for RG = 4. So, the absolute difference is 0.5 nA for standard-UME and with cone angle 30° and 0.8 nA with cone angle 45°.

The differences from standard-UME were calculated depending on RG factor. (2.24) was used for calculations as in Fig. 2.5 where only RG = 8 was considered. Almost no dependency was observed for outwarded-UME (Fig. 2.12A). Considering recessed-UME (Fig. 2.12B), the difference from standard-UME is greater with small RG factors such as RG = 4, but for bigger RG factors such as RG = 16 and RG = 32 dependency on RG is still limited. Finally, the most substantial dependency was observed for cone-UME (Fig. 2.12C): differences are rapidly increasing with decreasing RG factor.

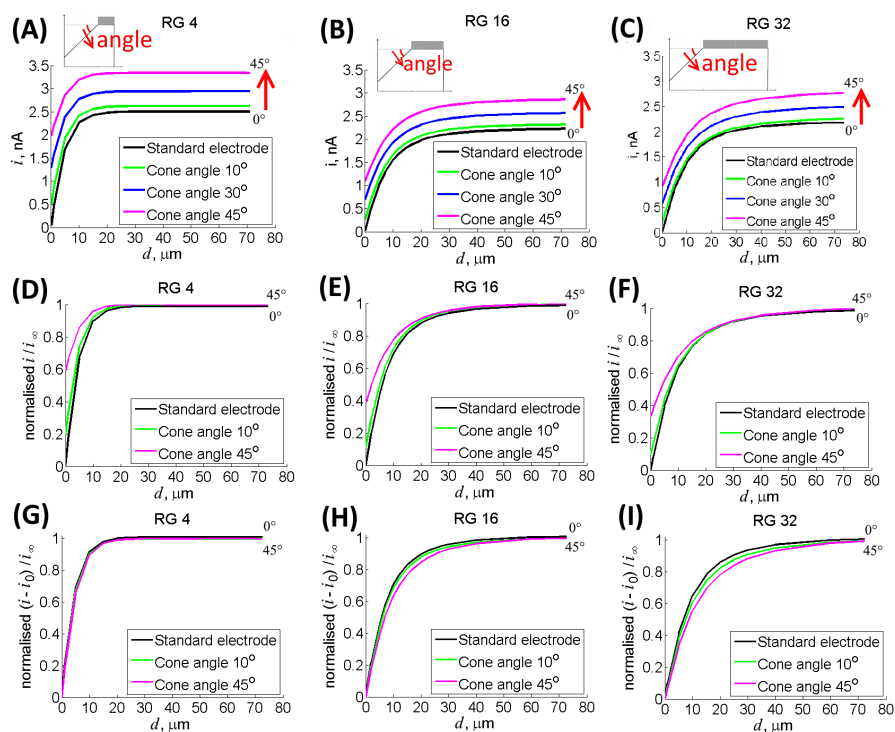


Figure 2.10: Approach curves for cone-UME and varying RG factors in different columns. Top row: Steady state current dependency on d for varying cone angle. Left column $r_{glass} = 20 \mu\text{m}$, middle column $r_{glass} = 80 \mu\text{m}$, right column $r_{glass} = 160 \mu\text{m}$.

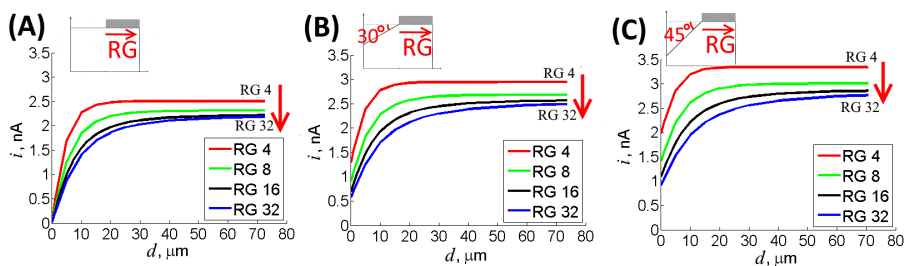


Figure 2.11: Approach curves for varying RG factors and different base angle of a cone: (A) standard-UME, (B) cone-UME with base angle 30° , (C) cone-UME with base angle 45° .

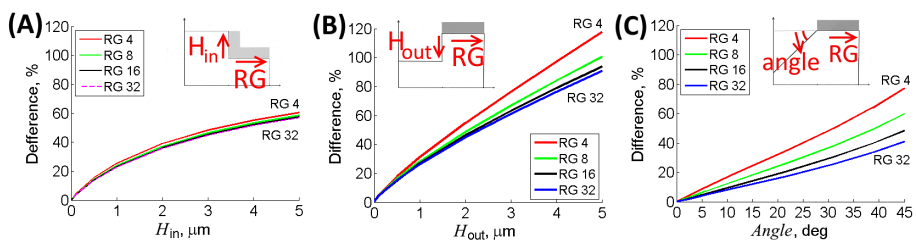


Figure 2.12: Differences between non-standard UMEs and standard-UME for varying RG factors. Geometry parameter for each type of the UME and RG factor are shown in the smaller schemes. (A) recessed-UME, (B) outward-UME, (C) cone-UME.

2.5.4 Analysis of isolines

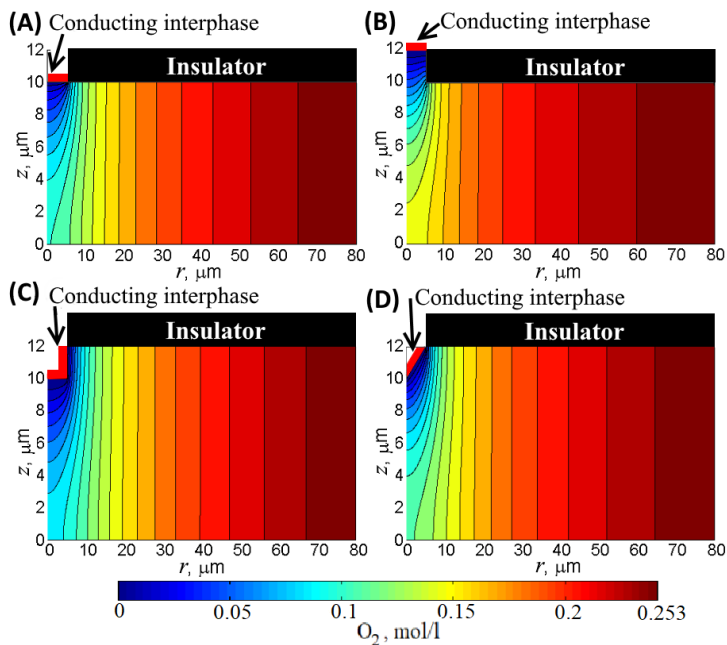


Figure 2.13: Isolines for various geometries of the UME. Conducting parts of UMEs are highlighted by red lines. (A) standard-UME, (B) recessed-UME, (C) outward-UME, (D) cone-UME.

Oxygen concentration isolines, presented in Fig. 2.13, display oxygen concentration levels in four environments close to analysed UMEs. We use this information to explain the differences in approach curves observed in modelled data. In general, oxygen concentration cannot be directly observed during an SECM experiment and the analysis of modelled oxygen concentration using isolines graphs is a valuable tool for a deeper understanding of SECM behaviour.

Isolines for standard-UME in Fig. 2.13A are interpreted as standard for comparison with that of other UMEs. As it is expected, the largest concentration of isolines is at $r = r_{el}$, i.e. the joint point between the UME tip and isolator. The highest rate of the current is also observed on this point using here presented experimental methods.

For outwarded-UME Fig. 2.13C, fewer isolines in z -direction than for standard-UME were observed, which is indicating that outwarded-UME would be less sensitive to the variation of oxygen concentration close to the surface of interest. Moreover, isolines are concentrated on the side of outwarded-UME, which is indicating that the greatest rate of oxygen diffusion is through this boundary edge. This effect will induce some discrepancy from the signal registered using standard-UME.

On the contrary, a greater number of isolines in z -direction for recessed-UME in Fig. 2.13B show increased sensitivity of this UME. But due to the large concentration of isolines on the turning point ($r = r_{el}, z = H$), lower concentrations of oxygen reach the conducting part of recessed-UME. In fact, if recess depth H_{in} is large enough or the distance from the surface is low, almost no oxygen reaches the tip and this kind of UME would be very inefficient.

Isolines of the cone-UME conducting part in Fig. 2.13D indicate greater sensibility compared to the standard-UME with the greatest concentration of isolines at the interphase of the conducting part of cone-UME with isolating part and at the sharp end of the cone. This may result in an undesirable effect of the increased current compared to that registered with the standard-UME.

2.5.5 Comparison with data of other studies

Ferrignio et al. [55] modelled recessed-UME and outwarded-UME and used the finite element method (FEM) to solve PDE. Analytical expression was established for the steady state current with maximum distance d :

$$i_{\infty} = 4nFD_{O_2}C_0 \left(r_{el} + \frac{\pi H_{out}}{4nH_{in}D_{O_2}t/r_{el}^2} \right), \quad (2.25)$$

which according to their research could be used in case of both UME types. In the study by Bartlett et al. [20] a model and simulations of recessed-UME using FEM were provided. Simulations were compared with analytical expressions derived by Bond et al. [26]:

$$i_{\infty, \text{norm}} = \frac{\pi}{4H_{in}/r_{el} + \pi}. \quad (2.26)$$

The formula is highly simplified and dimensionless (normalized), but it was shown that modelling data fits well.

Table 2.2: Differences between recessed-UME and standard-UME as calculated in the thesis, other models and by analytical expressions. Dimensionless distances were calculated and difference formula (2.24) was used for unified comparison. Data of the model of the thesis was taken from Fig. 2.5.

H_{in}/r_{el}	Thesis model	Ferrignio [55]	Analytical exp. (2.25)	Bartlett [20]	Analytical exp. (2.26)
0.04	9 %	1 %	5 %	9 %	6 %
0.08	18 %	7 %	13 %	12 %	9 %
0.4	38 %	36 %	34 %	36 %	34 %
0.8	52 %	52 %	50 %	52 %	50 %
1	58 %			57 %	56 %

Differences of the recessed-UME current (Fig. 2.5A) were compared with differences calculated from data of other models and analytical expressions in Table 2.2. It is evident that the model proposed in the thesis agreed well with data from other sources for larger values of recession depth H_{in} . Correspondence was worse for small H_{in} , but it can be seen that all models did not match so well.. Possible reasons are difficulties with FEM calculations with small depth, normalization and approximation procedures, etc.

In the case of outwarded-UME (Fig. 2.5B), the agreement was somewhat worse as shown in Table 2.3. The discrepancy was particularly high for small values of protrusion height H_{out} . However, it was reported in Ferrignio et al. that they had some difficulties in applying finite elements for calculations of standard-UME current. Furthermore, their own analytical function (2.26) approximates data very weakly at a small protrusion height, so it can be concluded that these calculations are unreliable. Meanwhile, the agreement between the model of the thesis and Ferrignio et al. was high for very larger and somewhat unrealistic values of H_{out} .

Table 2.3: Differences between outwarded-UME and standard-UME in simulations and analytical expression.

H_{out}/r_{el}	Thesis model	Ferrignio [55]	Analytical exp. (2.25)
0.04	12 %	17 %	3 %
0.4	46 %	62 %	30 %
1.6	147 %	120 %	171 %
3.2	254 %	241 %	297 %

2.6 Conclusions

The mathematical model, which describes three different non-standard geometries, was used to evaluate the difference from standard-UME in the current measured by broken UMEs. It was observed that the highest difference from standard-UME is obtained by outwarded-UME and the maximal difference reaches 100 % when the conducting part of the electrode is outwarded by 5 μm which cannot be clearly identified by optical microscopy. Differences for recessed-UME and outwarded-cone-UME are lower - 60 % and 50 % for 5 μm recess and 45° cone, respectively. These results were summed up in Table 2.1 showing which UME defects do not exceed the difference of 5 %, 10 %, 25 % and 50 % from standard-UME.

The advantage of the analysed mathematical model is that it can be used for the determination of defects in a simple buffer solution by comparing the simulated standard-UME response with experimental data. This method can be applied in various directions. In this study, buffer solutions were analysed, but the model can be extended with oxygen-reduction reactions to investigate the influence on reaction kinetics.

Acknowledgements

The authors are thankful for the HPC resources provided by the IT APC at the Faculty of Mathematics and Informatics of Vilnius University IT Research Center.

Chapter 3

Modelling of Fluorescence Dyes Uptake into 3D Cellular Spheroids

3.1 Introduction

In the Chapter 3 of the thesis, a novel mathematical and numerical model is proposed for the analysis of the accumulation of 2 types of fluorescent dyes – wheat germ agglutinin (WGA) and rhodamine – into cellular spheroids. A nonlinear system of reaction-diffusion equations was used for modelling the diffusion of WGA and rhodamine as well as the binding of WGA to the cells. Three different cases of the system were presented to describe the diffusion into cellular spheroids of these dyes. The Laplace operator of the nonlinear system was written in spherical coordinates because the modelled area is a sphere. The system was solved using a finite difference method and the resulting nonlinear system of algebraic equations was solved with an iterative method.

The computational results and the physical experiment were compared and close correspondence between them was achieved. Diffusion coefficients in the extracellular matrix for both dyes were calculated using model and experiment comparison. Moreover, the ratio between the dye concentration and the fluorescence intensity was evaluated. The influence of reaction parameters on dye penetration was analyzed. Dynamics of dyes uptake were estimated for spheroids of different size and cell/matrix density.

The mathematical modelling of 3D cellular spheroids is motivated by the recent emergency of 3D cell cultures in various biomedical studies. It is agreed that this method is more relevant to native tissues than the former gold standard – cell monolayers [46]. 3D cell cultures are usually used as a platform for primary drug testing, however, due to some limitations, not all drugs can be investigated. In that case, it would be useful to have mathematical models, which would predict drug accumulation and distribution in 3D cell cultures by using the data of similar already investigated molecules. The fluorescent dyes, whose physico-chemical characteristics such as structure and molecular mass are very similar to chemotherapeutic agents, could be used for modelling and quantification of drug penetration in 3D cell cultures.

One of the most commonly used 3D cell cultures is cellular spheroids. Cellular spheroids are self-assembled clusters of cell colonies cultured in environments where cell-cell interactions dominate over cell-substrate interactions. Some authors have published their attempts to simulate how various nanoparticles (NPs) accumulate and distribute in cellular spheroids. Gao et al. have established and studied a computational model to predict the time- and concentration-dependent diffusion of NPs in tumour cellular spheroids [58]. The mathematical model of antibody penetration into tumour spheroids was developed to gain an improved understanding of the quantitative interplay among the rate processes of diffusion, binding, degradation, and plasma clearance [66]. The same model was used to describe the diffusion of NPs into multicellular spheroids in the presence of the extracellular matrix modulator collagenase [65]. The results from the proposed model, in combination with the experimental results, suggested that particle size, particle binding, and porosity of biological tissue are the key parameters that need to be considered when designing NP drug carriers for cancer treatment. Our previous experimental study and modelling results also demonstrated that penetration of carboxylated nanoparticles was strongly limited and dependent on the size and porosity of cellular spheroids [77].

Chariou et al. provided the model to quantify diffusion and uptake of tobacco mosaic virus (TMV) in a spheroid system approximating a capillary-free segment of a solid tumour [33]. Model simulations predicted TMV concentration distribution over time in a tumour spheroid for different sizes and cell densities.

Oxygen consumption and diffusion in cellular spheroids were analyzed and a method was presented for estimating the rates of oxygen consumption and diffusion limit, the extents of the necrotic core, hypoxic region and proliferating rim [67].

Uptake and inward diffusion of a fluorescent dye calcein via gap junction intercellular communication were studied using a 3D multilayer spheroid model [1]. Quantitative studies about the kinetic parameters for efflux of various rhodamine dyes were performed [115] but only for 2D cell cultures. To the best of our knowledge, there are no mathematical models which would predict diffusion and accumulation of organic molecules (e.g. drugs or dyes) in 3D cell cultures.

Two types of fluorescent dyes were considered in the study – rhodamine 6G (R6G) and wheat germ agglutinin (WGA). R6G is a fluorescent positively charged lipophilic dye, which specifically stains and selectively accumulates in mitochondria. It was also reported that at higher concentrations, R6G also stained the endoplasmic reticulum and other membrane organelles. Due to its lipophilic nature R6G is also known as a specific stain for the detection of lipids. This allows R6G to be used as a universal lipid marker for both qualitative [43] and quantitative research [32]. Masuda and Oguma study showed that R6G dye could be used not only for in vitro cell studies but also for visualizing the vascular networks of the liver and to examine the intrahepatic flow distribution under various conditions [95].

WGA is a lectin that protects wheat (*Triticum*) from insects, yeast and bacteria. Wheat germ agglutinin selectively binds to N-acetylglucosamine and N-acetylneuraminic acid (sialic acid) residues which are predominantly found on the plasma membrane [145]. WGA conjugated to Alexa Fluor fluorophores (WGA-Alexa488) is used as a fluorescent marker to stain the plasma membrane of various mammalian cells.

In section 3.2 of the chapter, details about 3 mathematical models were presented alongside calculation of equations parameters and numerical solution. In section 3.3, computational and physical experiments were compared and results of the study were discussed. Finally, the results of the Chapter were summarized in conclusions 3.4.

3.2 Mathematical models

3.2.1 WGA migration modelled with reaction-diffusion equations

Diffusion is the driver of biological processes in cells and 3D spheroids. The diverse temporal scales of intracellular and intercellular processes

are determined by vastly diverse spatial and temporal scales in most biological and biophysical processes. The latter is due to small binding sites inside or on the cell membrane or to narrow passages between large cellular and intercellular compartments.

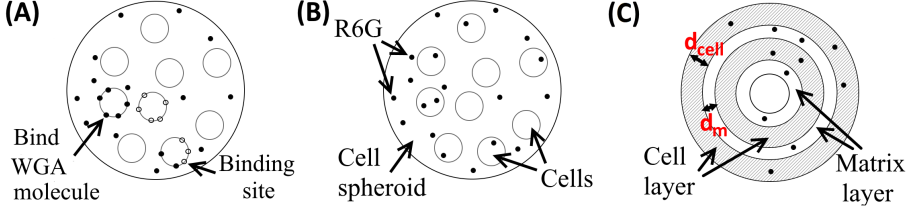


Figure 3.1: (A) WGA model, (B) R6G model, (C) Rings model.

WGA molecules diffusion and binding in 3D cell spheroids is expressed by the equation:

$$\frac{\partial C_{out}}{\partial t} = D \frac{1}{r^2} \frac{\partial}{\partial r} \left(r^2 \frac{\partial C_{out}}{\partial r} \right) - k_{bind} (B_{max} - C_{bind}) C_{out}$$

for $0 < t \leq T, \quad 0 < r < R, \quad (3.1)$

where $C_{out}(t, r)$ is the concentration of WGA molecules in spheroid as a function on time and coordinate, D – the diffusion coefficient, k_{bind} is a rate constant of binding of WGA to the cell membrane, R is the radius of a spheroid, t – time variable, r – the distance from the centre of sphere, T – modelling duration.

The diffusion equation was written in spherical coordinates and the assumption was made that spheroids are approximately homogeneous in all directions.

As shown in Fig. 3.1A, there is a limited number of sites on cell membranes for molecules to bind, which is denoted by the constant B_{max} [57]. When this number is reached, no molecules can bind on the cell membrane. The process of binding to cells is modelled by the equation:

$$\frac{\partial C_{bind}}{\partial t} = k_{bind} (B_{max} - C_{bind}) C_{out}, \quad 0 < t \leq T, \quad 0 < r < R, \quad (3.2)$$

where $C_{bind}(t, r)$ is the concentration of WGA molecules which are bound to the cells membrane.

The following boundary conditions are used:

$$\begin{aligned} C_{out}|_{r=R} &= C_{outside}, \\ \frac{\partial C_{out}}{\partial r}|_{r=0} &= 0, \quad t > 0, \end{aligned} \quad (3.3)$$

which show that in the exterior of a spheroid there is a constant concentration of WGA molecules $C_{outside} = \frac{5 \mu\text{g/mL}}{38643 \text{ g/mol}} = 0.13 \mu\text{M}$ and that there is symmetry to the centre of a spheroid.

Initial conditions for both functions of concentrations are

$$\begin{aligned} C_{out}|_{t=0} &= 0, \\ C_{bind}|_{t=0} &= 0, \quad 0 \leq r \leq R, \end{aligned} \quad (3.4)$$

indicating that there is no WGA molecules at the start of experiment and all binding sites are free.

3.2.2 Rhodamine migration modelled with diffusion equation

Rhodamine R6G diffuses both through cells and cellular matrix (Fig. 3.1B) and thus diffusion of R6G molecules in spheroids is modelled using the diffusion equation:

$$\frac{\partial C}{\partial t} = D \frac{1}{r^2} \frac{\partial}{\partial r} \left(r^2 \frac{\partial C}{\partial r} \right), \quad \text{for } 0 < t \leq T, \quad 0 < r < R, \quad (3.5)$$

where $C(t, r)$ is R6G concentration and it is a version of (3.1) without the reaction element.

The same boundary conditions are used for the R6G model as in (3.3):

$$\begin{aligned} C|_{r=R} &= C_{outside}, \\ \frac{\partial C}{\partial r}|_{r=0} &= 0, \quad t > 0. \end{aligned} \quad (3.6)$$

Molar concentration $C_{outside} = \frac{5 \mu\text{g/mL}}{493 \text{ g/mol}} = 10.4 \mu\text{M}$ is greater for R6G due to a smaller molar mass than WGA-Alexa488.

Initially, there are no Rhodamine molecules in spheroid, so we have

$$C|_{t=0} = 0, \quad 0 \leq r \leq R. \quad (3.7)$$

It should be noted that the R6G model is separate linearized version of the WGA model given by (3.1)–(3.4), but with k_{bind} set to 0 and different coefficients.

3.2.3 Rhodamine migration using the rings of cells and matrix layers model

Spheroids were modelled as concentric rings of cells and matrix layers as in Fig. 3.1C, where cell rings represent averaged cells and cellular matrix layer – material between the cells. The process is expressed by the following equation:

$$\frac{\partial C}{\partial t} = \frac{1}{r^2} \frac{\partial}{\partial r} \left(r^2 D(r) \frac{\partial C}{\partial r} \right), \quad \text{for } 0 < t \leq T, \quad 0 < r < R, \quad (3.8)$$

where $D(r)$ is a function representing the diffusion coefficient

$$D(r) = \begin{cases} D_{cell}, & \text{if } r \in \text{cell layer,} \\ D_{matrix}, & \text{if } r \in \text{matrix layer.} \end{cases} \quad (3.9)$$

D_{cell} is the diffusion coefficient in cells and D_{matrix} is the diffusion coefficient in cellular matrix, $d_{cell} = 10 \mu\text{m}$ is an average diameter of cells and d_m is an average distance between cells, which was calculated in such a way that a known number of cells N of size d_{cell} would fit into the spheroid of radius R .

Boundary and initial conditions remain the same as in section 3.2.2:

$$\begin{aligned} C|_{r=R} &= C_{outside}, \quad t > 0, \\ \frac{\partial C}{\partial r} \Big|_{r=0} &= 0, \quad t > 0, \\ C|_{t=0} &= 0, \quad 0 \leq r \leq R. \end{aligned} \quad (3.10)$$

3.2.4 Calculation of coefficients

Diffusion coefficient

The R6G dye diffuses both through the cells at diffusion rate D_{cell} and the extracellular matrix at the rate D_{matrix} . In the study, the diffusion

coefficient for the R6G model in (3.5) was averaged in the whole spheroid:

$$D = \phi D_{cell} + (1 - \phi) D_{matrix},$$

where $\phi = \frac{N_{cell} V_{cell}}{V_{sphere}}$ is the proportion of total cell volume to spheroid volume, $(1 - \phi)$ – the proportion of extracellular matrix volume to spheroid volume, V_{cell} is the volume of a cell, which is considered to be spherical, V_{sphere} – the volume of cellular spheroid. N_{cell} is the number of cells in particular spheroid ranging from 6000 to 14 000.

The diffusion coefficient of R6G or similar Rhodamine dyes was investigated theoretically and experimentally by many authors. It was observed that the coefficient varies from $4.0 \times 10^{-10} \text{ m}^2/\text{s}$ in water solutions [59] to $1.5 \times 10^{-18} \text{ m}^2/\text{s}$ in high concentration sucrose-water solutions [35]. $D_{cell} = 3 \times 10^{-13} \text{ m}^2/\text{s}$ in *stratum corneum* [6], i.e. the outermost layer of the skin, was chosen as it resembles the cells used in the experiment most closely. The diffusion coefficient in cellular matrix D_{matrix} was obtained by fitting experimental data to the R6G model data (see section 3.3.2).

For the Ring model, the same coefficient D_{matrix} was used, but the diffusion coefficient in cells was adjusted taking into account that cells would not be fully squeezed into a uniform cell ring and there would be some gaps at least between the sides of cells as shown in the scheme Fig. 3.1C. In the analyzed model the formula for $D_{cell, ring}$ was derived by calculating the ratio between the volume of sphere and cube:

$$D_{cell, ring} = \frac{\pi}{6} D_{cell} + \left(1 - \frac{\pi}{6}\right) D_{matrix}.$$

WGA molecules diffuse only through cellular matrix with cells acting as immobilized barriers. The diffusion through porous media model was used to calculate the diffusion coefficient [58, 141]:

$$D = (1 - \phi)^2 D_{matrix},$$

where $(1 - \phi)$ accounts for porosity. It was demonstrated [109] that diffusion rates of R6G and WGA-Alexa488 dyes differ only by approximately 2.1 % and the same R6G diffusion coefficient in matrix D_{matrix} was used.

Binding coefficients

Maximal concentration of binding sites per unit volume depends on a particular spheroid size and cell density. It was calculated using the

formula

$$B_{max} = \frac{N_{cell} B_{max, cell}}{N_A V_{sphere}}, \quad (3.11)$$

where $N_A = 6 \times 10^{23}$ is Avogadro constant, $B_{max, cell} = 5 \times 10^5$ sites/cell is the number of binding sites in a single cell [57].

The binding rate constant (association constant) for WGA was determinant to vary from 10^2 to 10^6 in studies [9, 57, 104]. During computational experiment several values of the binding constant were used. These calculations showed that at rates $k_{bind} = 10^3 - 10^4 \text{ M}^{-1}\text{s}^{-1}$ reaction speed is maximal possible, because the diffusion rate becomes a limiting factor. Therefore, $k_{bind} = 10^3 \text{ M}^{-1}\text{s}^{-1}$ was chosen for other computations.

Accumulative concentration

For comparison with experimental data, accumulative concentration C_{acc} per volume, i.e. the total concentration in a spheroid divided by its volume, was calculated as an integral

$$C_{acc}(t) = \frac{4\pi}{V_{sphere}} \int_0^R C(t, r) r^2 dr. \quad (3.12)$$

3.2.5 Numerical solution

First of all, a rectangular domain $\{(t, r) \in \mathbb{R}^2 : 0 < t \leq T, 0 < r < R\}$ had to be discretised for all models: WGA model (3.1)–(3.4), R6G model (3.5)–(3.7) and Ring model (3.8)–(3.10). The discrete 2D grid $\bar{\omega}$ was defined

$$\begin{aligned} \bar{\omega}_h &= \{r_i : r_i = ih, i = 0, \dots, N, r_0 = 0, z_N = R\}, \\ \bar{\omega}^\tau &= \{t^k : t^k = k\tau, k = 0, \dots, K, t^0 = 0, t^K = T\}, \\ \bar{\omega} &= \bar{\omega}^\tau \times \bar{\omega}_h. \end{aligned}$$

2D discrete grid was chosen consisting of 100 points in r direction and 240 000 points in t direction. Such a large number of points was necessary because modelling time $T = 24 \text{ h}$ was long and high accuracy had to be achieved.

The numerical solutions on grid $\bar{\omega}$ were denoted by $U_i^k \approx C_{out}(t^k, r_i)$ and $V_i^k \approx C_{bind}(t^k, r_i)$. Only solution $U_i^k \approx C(t^k, r_i)$ was used for R6G and Ring models.

Then, (3.1) was discretised using the Crank-Nicolson implicit scheme

$$\frac{U_i^{k+1} - U_i^k}{\tau} = D \left(\frac{\bar{U}_{i-1} - 2\bar{U}_i + \bar{U}_{i+1}}{h^2} + \frac{1}{r_i} \frac{\bar{U}_{i+1} - \bar{U}_{i-1}}{h} \right) - k_{bind}(B_{max} - \bar{V}_i)\bar{U}_i, \quad i = 1, \dots, N-1, \quad (3.13)$$

where $\bar{U}_i = (U_i^{k+1} + U_i^k)/2$ and $\bar{V}_i = (V_i^{k+1} + V_i^k)/2$. It is a well known stable scheme and the approximation error is second order, i.e. $\mathcal{O}(\tau^2 + h^2)$ in case continuity conditions are satisfied [101, 113]:

$$C_{out} \in C_4^3((0, T] \times (0, R)), \quad C_{bind} \in C^3((0, T]).$$

Reaction equation (3.2) was discretised by

$$\frac{V_i^{k+1} - V_i^k}{\tau} = k_{bind}(B_{max} - \bar{V}_i)\bar{U}_i, \quad i = 1, \dots, N-1, \quad (3.14)$$

which is again the second order scheme with $\mathcal{O}(\tau^2)$ error. Finally, boundary condition (3.3) for $r = 0$ was discretised by the second order finite difference formula

$$3U_0^{k+1} - 4U_1^{k+1} + 2U_2^{k+1} = 0. \quad (3.15)$$

These approximations guarantee that the entire system (3.1)–(3.4) was approximated by the stable second order scheme.

V_i^{k+1} was expressed from (3.14)

$$V_i^{k+1} = \frac{4V_i^k + \tau k_{bind}(2B_{max} - V_i^k)(U_i^{k+1} + U_i^k)}{4 + \tau k_{bind}(U_i^{k+1} + U_i^k)}. \quad (3.16)$$

By substituting (3.16) into (3.13), the nonlinear system of algebraic equations was derived

$$A\mathbf{U}^{k+1} = \hat{A}\mathbf{U}^k + F(\mathbf{U}^{k+1}, \mathbf{U}^k), \quad (3.17)$$

where $\mathbf{U}^k = (U_0^k, \dots, U_N^k)$, A and \hat{A} are $(N-1)$ -size matrices with coefficients from the diffusion term in (3.13), F is nonlinear part of the

system from the reaction term. (3.17) was linearized by Picard's iterative process [36]:

$$\begin{aligned} \mathbf{A}\mathbf{U}^{(j+1)} &= \widehat{\mathbf{A}}\mathbf{U}^k + F(\mathbf{U}^{(j)}, \mathbf{U}^k), \quad j = 0, \dots \\ \mathbf{U}^{(0)} &= \mathbf{U}^k. \end{aligned} \quad (3.18)$$

The system (3.18) is tridiagonal and was solved using the Thomas algorithm at each iteration step. The iterative process was repeated until condition between 2 iterations was no larger than $\varepsilon = 10^{-10}$. The process converged rapidly and no more than 4 iterations were required.

Because the R6G model is linear, (3.5) was discretized by the version of (3.13) without the reaction term and solved with a single application of the Thomas algorithm. In the case of the Ring model, the diffusion coefficient (3.9) is step function and, because of that, separate version of the Crank-Nicolson scheme was applied to approximate (3.8)

$$\frac{U_i^{k+1} - U_i^k}{\tau} = \frac{1}{r_i^2} \frac{D_{i+0.5} r_{i+0.5}^2 (\bar{U}_{i+1} - \bar{U}_i) - D_{i-0.5} r_{i-0.5}^2 (\bar{U}_i - \bar{U}_{i-1})}{h^2} \quad i = 1, \dots, N-1, \quad (3.19)$$

where $r_{i\pm 0.5} = r_i \pm 0.5h$, the diffusion coefficient $D_{i\pm 0.5} = D(r_i \pm 0.5h)$ from (3.9). The tridiagonal system of linear equations was derived from (3.19) and (3.15), which approximates boundary condition (3.10) at $r = 0$, and was solved by the Thomas algorithm.

Necessary integrals such as (3.12) on the discrete grid were calculated with the first order Newton-Cotes formula. All algorithms were implemented by the author in Python with the NumPy library.

3.3 Results

3.3.1 Analysis of experimental results

The accumulation of R6G in NIH3T3 spheroids was investigated using 2 methods: confocal microscopy (Fig. 3.2) and flow cytometry. In Fig. 3.2A, it was shown, that after 1 h of incubation, R6G accumulated only in the top layer of the spheroid and the intensity of it was relatively low compared with the images after longer incubation times. The accumulation of R6G increased after longer incubation times. After 4 h of

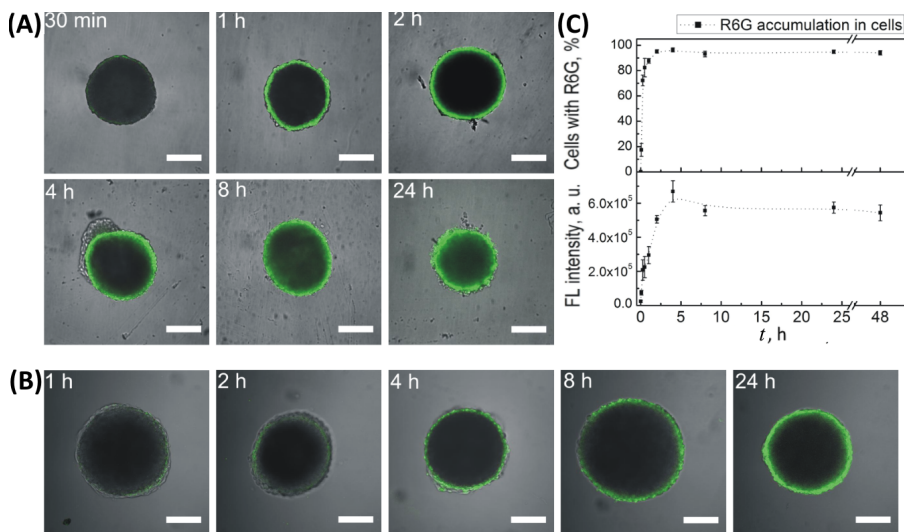


Figure 3.2: (A) Combined confocal microscopy and bright field images of R6G (green color, $\lambda_{ex} = 488 \text{ nm}$) distribution in NIH3T3 cellular spheroids (8000 cells/drop, $R \approx 134 \mu\text{m}$), after different incubation times t . (B) Combined confocal microscopy and bright field images of WGA-Alexa488 (green color, $\lambda_{ex} = 488 \text{ nm}$) distribution in NIH3T3 cellular spheroids, after different incubation times t . Representative images are shown. Scale bar $150 \mu\text{m}$. (C) Quantitative evaluation of R6G accumulation in NIH3T3 spheroids. Percentage of cells with R6G molecules (upper) and fluorescence (FL) intensity per spheroid volume (lower) are presented in separate graphs. Every value is an average of 3 samples. Error bars represent standard deviation. Dotted line is an approximation.

incubation R6G fluorescence was observed through the whole spheroid and fluorescence intensity increased after 8 h and 24 h of incubation.

The accumulation of WGA-Alexa488 dye in NIH3T3 spheroids was demonstrated in Fig. 3.2B. The penetration of WGA-Alexa488 dye in the NIH3T3 cellular spheroid was slower than R6G dye. After 4 h fluorescence of R6G dye was detected through the whole cellular spheroid optical section, while WGA-Alexa488 was detected only on the external part of the spheroid. Even after 24 h of incubation, only low fluorescence of WGA-Alexa488 was measured from internal parts of the spheroid, suggesting that a small amount of WGA-Alexa488 molecules penetrated into the centre of a cellular spheroid.

For quantitative evaluation of R6G accumulation in cellular spheroids measurements with flow cytometry were made. The obtained results were demonstrated in Fig. 3.2C and used for the comparison with mathematical modelling results as presented in Fig. 3.3A. The quantitative evaluation showed that after short times of incubations only cells, which were close to the spheroid surface, had accumulated R6G, thus the mean fluorescence intensity was low. It was observed (Fig. 3.2C, lower part) that fluorescence intensity was growing from 5 min to 4 h of incubation, but not as rapidly as the number of the cells which had R6G inside (Fig. 3.2C, upper part). After 2 h of incubation, $95 \pm 1\%$ of cells had accumulated R6G, but fluorescence intensity reached only $75 \pm 5\%$ of its maximum value. It can be concluded that some cells had accumulated only a small amount of R6G molecules. The peak of fluorescence intensity was observed after 4 h of incubation. Later fluorescence intensity stabilized and did not change during measurements. This means that after 4 h of incubation with R6G, spheroids of radius $R \approx 150 \mu\text{m}$ had fully accumulated R6G molecules. For comparison, in experiments with a single layer of cells the maximum fluorescence intensity is reached after 2 h of incubation.

3.3.2 Comparison between experimental and simulations data for R6G accumulation models

The diffusion coefficient in the cellular matrix was calculated by fitting model data to physical experimental data by the least squares method. Accumulative R6G concentration, which was calculated using the model (3.5)–(3.7) and integrated by (3.12), and fluorescence intensity from the experiment were normalized into non-dimensionless values in order to compare them. Linear dependence between fluorescence intensity and concentration of the source is well known and the device constant can be calculated by normalizing, i.e. by dividing by maximal concentration and fluorescence intensity. It was determined that $D_{matrix} = 4.2 \times 10^{-13} \text{ m}^2/\text{s}$ fits the experiment best (Fig. 3.3A) and the device constant for this particular experiment is 6.4×10^{10} .

Another experimental data set was used for the confirmation of the R6G model. Fluorescence intensities were calculated at 2 h time for spheroids with different radius and number of cells (Fig. 3.3B). Accumulated R6G concentrations were multiplied by the device constant and plotted for comparison with experimental data (Fig. 3.3B). Intensities calculated per cell decrease for larger spheroids which are expected because it is increasingly difficult for the dye to reach inner layers. The

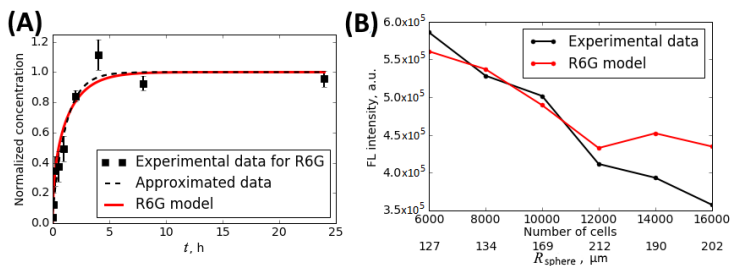


Figure 3.3: (A) R6G model curve (red line) was fitted to experimental data (dashed line) in order to find the diffusion coefficient in cellular matrix; 8000 cells, radius $134 \mu\text{m}$. Black squares are experimental data and their standard deviation is represented by error bars. (B) Accumulated fluorescence intensity compared to intensities from experimental data; different spheroid size and number of cells, time $t = 2 \text{ h}$.

very close correspondence between the experiment and model was observed up until the largest numbers of cells. The size of the cellular spheroid depends on the initial cell number until the critical number of cells is reached. It was observed that, while growing spheroids from 6000 up to 10 000 cells, the size of spheroid increased linearly, but spheroids with a large number of cells ($N_{\text{cell}} = 14000$ and $N_{\text{cell}} = 6000$) were similar in size and their radius did not depend on cell number. Thus our model showed that spheroids from 6000 up to 10 000 cells are suitable for dyes penetration studies, whereas larger spheroids should not be used because of inaccuracies.

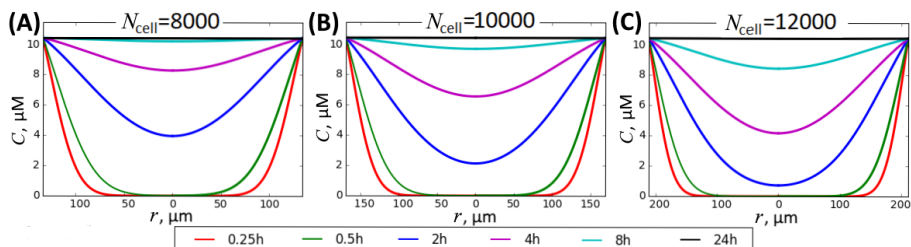


Figure 3.4: R6G concentration from centre to the sides of the spheroid at various time intervals and different spheroids (A) $N_{\text{cells}} = 8000$, $R = 134 \mu\text{m}$, (B) $N_{\text{cells}} = 10000$, $R = 169 \mu\text{m}$, (C) $N_{\text{cells}} = 12000$, $R = 212 \mu\text{m}$.

Using the R6G migration model (section 3.2.2) R6G dye accumulation inside the spheroid was calculated. Fig. 3.4 shows R6G concentration

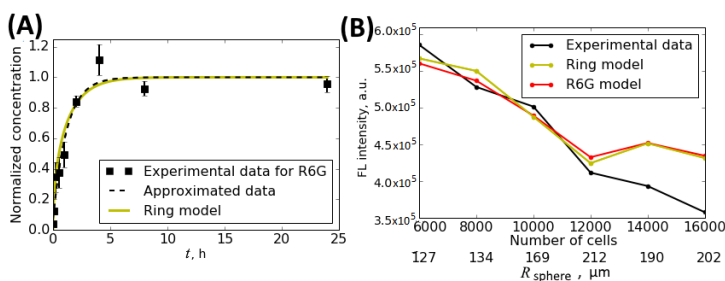


Figure 3.5: (A) Ring model results compared with spheroid penetration by time. Diffusion coefficients are taken from the R6G model. Spheroid with 8000 cells, radius 134 μm . (B) Accumulated fluorescence intensity from the Ring model data, R6G model and experiment, time $t = 2$ h.

dependency from distance r to the centre at various time intervals. Three spheroids were modelled with a different number of cells, i.e. cell/matrix density, and spheroid radius R . These parameters were taken from experimental data.

It can be observed that the first few layers ($\sim 20 - 30 \mu\text{m}$) were almost fully accumulated after about 15 min in all spheroids. The centre of the smallest analyzed spheroid was filled after less than 8 h (Fig. 3.4A) but the centre of the larger spheroid in Fig. 3.4C was reached much slower. After 24 h all spheroids were completely filled with R6G molecules.

An alternative Ring model was proposed in order to better understand R6G penetration into spheroids as explained in section 3.2.3. The penetration curve in Fig. 3.5A was calculated with R6G cell and matrix diffusion coefficients which were used in the previously analyzed R6G model. The curve is very close to approximated experimental data as the mean squared error is only 0.04 %. For comparison, penetration curve calculated with the R6G model (Fig. 3.3A) has an error of 0.05 % from experimental data. It can be concluded that the error is very small in both cases.

In Fig. 3.5B the fluorescence intensity of the Ring model was plotted against experimental and R6G model data. While both models agree fairly well with experimental data, the Ring model is slightly more accurate with 4.9 % error compared to 5.2 % error for the R6G model. From these results, we conclude that both models are successful and can be used for further analysis of dyes penetration. The Ring model can be applied to determine the effects of cells diameter and cellular matrix layer size, i.e. the average distance between cells, on dye penetration.

3.3.3 Nonlinear WGA model analysis

The WGA model was proposed in section 3.2.1 to analyze WGA molecules diffusion and binding to cells. This process is experimentally difficult to conduct and modelling has to be employed. It is expected that the WGA model would be accurate because WGA diffusion in 3D spheroids is closely related to R6G diffusion which agrees with the experiment well as shown in section 3.3.2. Comparing with the R6G model, the reaction term was added to account for binding to cells and binding rate k_{bind} and the concentration of binding sites B_{max} was evaluated. Diffusion was calculated only in the cellular matrix because WGA molecules do not diffuse through the cell membrane.

Using the WGA model concentration in cellular matrix C_{out} and concentration of bound WGA molecules C_{bind} were computed and shown in the upper and middle rows of Fig. 3.6 for 3 different spheroids. It was observed that the penetration rate for the smaller spheroid (Fig. 3.6A) was faster than for the larger one (Fig. 3.6B). The spheroid formed from 8000 cells was denser than 6000 cells spheroid and thus there was a greater amount of binding sites (compare Fig. 3.6E with Fig. 3.6D). Because of that WGA penetration into the centre of 8000 cell spheroid was slowed down not only by greater size but also by a faster binding process.

In the case of the largest spheroids (Fig. 3.6C), it was observed in the experiment that they were much sparser (see x axis in Fig. 3.3B). As it was mentioned before, some changes in spheroid formation occurred due to a large number of cells. It was demonstrated that the spheroid's porosity depends on the size and cell type [77]. 3D spheroids formed from cancer cells are sparser because cancer cells tend to migrate and metastasize. As shown in Fig. 3.6F, the number of binding sites per unit volume was much smaller and almost all sites were taken in 24 h. Therefore, diffusion was not slowed so much by the reaction term and the spheroid centre was almost completely penetrated by WGA in 24 h even though the spheroid was larger than the others.

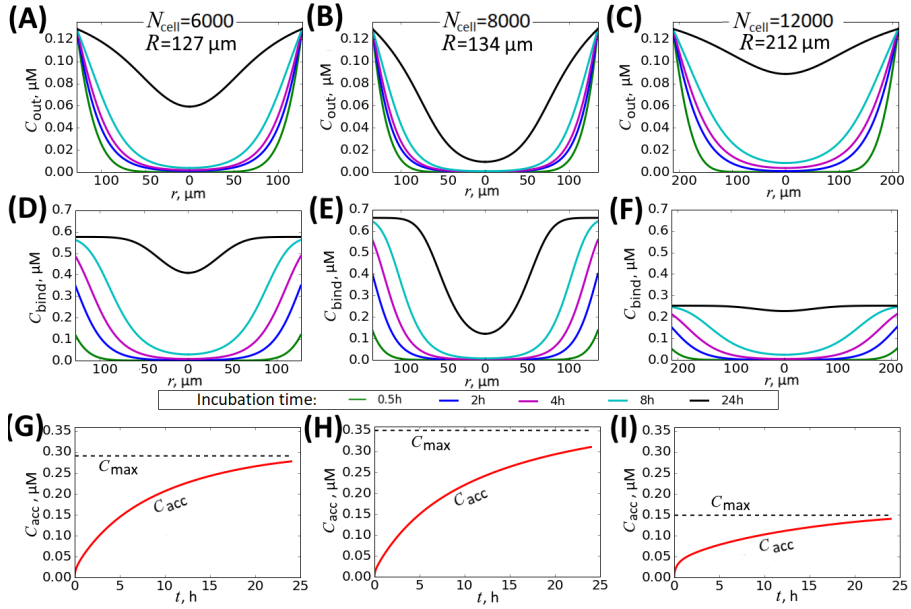


Figure 3.6: WGA dye concentration C_{out} in cellular matrix (upper row) and C_{bind} in cells (middle row). Bottom row: accumulative WGA concentration C_{acc} in matrix and cell together. C_{max} shows maximum concentration for each spheroid. Left column: spheroid with 6000 cells and radius 127 μm , middle column: Spheroid with 8000 cells and radius 134 μm , right column: Spheroid with 12 000 cells and radius 212 μm .

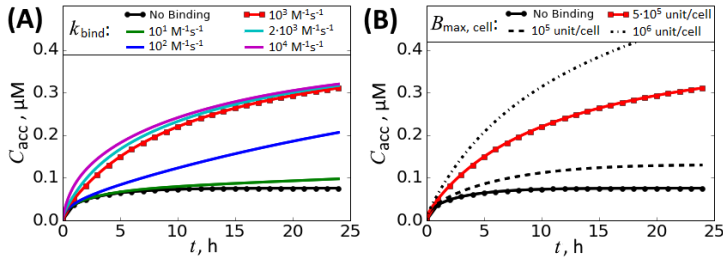


Figure 3.7: Accumulative WGA concentration in 8000 cells spheroid with (A) different binding constant k_{bind} and fixed $B_{max, cell} = 5 \times 10^{-5}$ unit/cell binding sites; (B) different number of binding sites $B_{max, cell}$ and fixed $k_{bind} = 10^3 \text{ M}^{-1}\text{s}^{-1}$. The red line marks results with same binding parameters.

These nonlinear effects were further explained in Fig. 3.6G, H, I.

Accumulated concentration per volume

$$C_{acc}(t) = (1 - \phi) C_{out, acc}(t) + \phi C_{bind, acc}(t), \quad \phi = \frac{N_{cell} V_{cell}}{V_{sphere}}$$

was calculated and compared with maximum concentration per volume

$$C_{max} = (1 - \phi) C_{outside} + \phi B_{max},$$

which can accumulate into cellular matrix and cell membranes of spheroids. Accumulated concentrations in matrix $C_{out, acc}$ and in cells $C_{bind, acc}$ were calculated by (3.12). The spheroid with 8000 cells (Fig. 3.6H) was the densest and, therefore, it accumulated more WGA molecules on average than the smaller spheroid (Fig. 3.6G). It was observed that the accumulative concentration of 8000 cell spheroid was greater even though the centre was almost not incubated at all at 24 h. It can be explained by spherical geometry, because outer layers of a sphere account for a much greater volume than inner layers. On the other hand, for 12 000 cell spheroid C_{max} and C_{acc} are much smaller due to lesser density (B_{max} is 2 – 3 times smaller than B_{max} for 6000 and 8000 cells spheroids) and its matrix layer was penetrated more rapidly (Fig. 3.6C) than for smaller spheroids.

The effect of reaction parameters to accumulative WGA dye concentration was investigated for the spheroid of radius 134 μm and formed from 8000 cells. Various values (Fig. 3.7A) of the binding constant k_{bind} were tested. It was observed that with $k_{bind} = 10^4 \text{ M}^{-1} \text{ s}^{-1}$ accumulation speed no longer increased which means that diffusion process is a limiting factor and this binding rate is so rapid that all available dye molecules bind almost instantly. However, at lower binding ratios ($< 10^2 \text{ M}^{-1} \text{ s}^{-1}$) accumulation speed was almost linear. Then the constant was set to zero, the binding process stopped and concentration reached its balance at about 4 h, which is compatible with R6G models.

In Fig. 3.7B the effects of the number of binding sites per cell $B_{max, cell}$, which was used to calculate binding site concentration B_{max} by (3.11), can be seen. As expected, a greater number of sites resulted in increased accumulative concentration. Fig. 3.7A, B showed, that WGA dye accumulation dynamics strongly depend on the binding constant and the number of receptors (binding sites) in the cells. From modelling results at a fixed binding rate constant $k_{bind} = 10^3 \text{ M}^{-1} \text{ s}^{-1}$ it could be predicted that 3.4 times more WGA dye molecules accumulated after 24 h for cells with 10 times more receptors on their plasma membranes.

3.4 Conclusions

The reaction-diffusion model was presented for analysis of dyes penetration into cellular spheroids. Both cases of the model for R6G dye, i.e. linear diffusion model and Ring model, showed a close correspondence with experimental results. Using the model, it was calculated that the diffusion coefficient in the cellular matrix is $D = 4.2 \times 10^{-13} \text{ m}^2/\text{s}$, which is about 4 times higher than the diffusion coefficient in cells used in calculations. Accumulation dynamics were analyzed and it was shown that about 4 h are necessary to reach a balance, but the central zone is not fully incubated until about 10 h. These dynamics also strongly depend on the spheroid size and density.

The dynamics of WGA-Alexa488 dye penetration into the spheroid was analyzed using a nonlinear case of the model. The effect of the binding rate and binding sites number on penetration dynamics was researched. Our experimental and modelling results showed that the dynamic of WGA-Alexa488 dye accumulation in cells is non-linear, because of several biological processes, such as the rate of endocytosis, the density of cells and extracellular matrix, type and concentration of receptors in the cells plasma membrane and other factors.

Chapter 4

Verification of Model Implementation

The final chapter is dedicated to the verification of numerical algorithms which are applied for solving PDEs of proposed models.

Model verification and validation (V&V) is an important concept in computer simulations [132]. Verification is defined as the process of determining that a model and its solution is accurately implemented. Validation is the process of determining if a model is an accurate representation of the real-world data/experiment.

Numerous techniques and frameworks have been proposed for V&V in literature [83, 118, 142]. The correctness of differential equations-based computer models, which are solved by finite difference or finite element methods, was analysed using various testing methods: (i) comparison with known test solutions [29, 85], (ii) analysis of model behaviour under test conditions [23], (iii) comparison between model and experimental data [34, 51].

Various techniques were applied to determine if the implementation of the models, presented in the thesis, was correct. Model validation was carried in each particular chapter by comparing simulations with physical experiment data.

4.1 Theoretical properties of solutions of differential equations

Maximum and minimum values

It is well established that PDEs and systems of PDEs of parabolic type satisfy the maximum principle [48, 128]. The strong version of the principle states that the maximum (and minimum) of the solution is attained only on the boundary of the domain Ω_T , i.e. at initial values $\Omega \times \{0\}$ or at the border of Ω_T , and all values in the interior points must be smaller (or greater than the minimum). The numerical solution must follow the same principle: maximum (and minimum) is attained at the boundary point of grid and values at inner points are smaller (greater) [116].

Naturally, these conditions also follow from chemical/biological applications of models. The maximum principle guarantees that concentrations of reagents cannot be greater than the amount provided in an exterior solution. The minimum principle ensures that concentrations do not become negative because in all models some boundary or initial condition is 0.

Graphically the maximum principle for UME geometry models was demonstrated by isolines in Fig. 2.13 which show that $0 \leq C_{O_2} \leq 0.253 \text{ mol/m}^3$ for $t = T$.

Table 4.1: Maximum and minimum is compared between inner and boundary points showing that the maximum principle is attained. Model parameters: $d = 100 \text{ }\mu\text{m}$, $Gl_{c_{\text{outside}}} = 0.6 \text{ mol/m}^3$.

	Max in inner points	Max at boundary	Min in inner points	Min at boundary
C_{O_2}	0.252 95	0.253	3.340×10^{-6}	0
C_{Glc}	0.590 66	0.6	7.081×10^{-18}	0
$C_{H_2O_2}$	0.005 94	0.006 14	4.069×10^{-28}	0
C_{Glu}	0.021 15	0.021 99	4.240×10^{-47}	0

Computational tests of the maximum principle for the RC-SECM model were provided in Table 4.1. As expected, the maximum and minimum of numerical solutions $U_{O_2}, U_{Glc}, U_{H_2O_2}, U_{Glu}$ was attained in the boundary of the domain. In particular, $U_{O_2} \leq 0.253 \text{ mol/m}^3$ and

$U_{Glc} \leq 0.6 \text{ mol/m}^3$, which is due to boundary conditions, while the upper limit of $U_{H_2O_2}$ and U_{Gll} is computed by the model as it depends on reaction rate, i.e. reaction rate constants, Glc_{outside} .

The maximum principle was tested for other models in in Table 4.2. For SECM geometry models minimum values of 0 were attained at the boundary according to the theory, while the maximum value was slightly larger than expected 0.253 mol/m^3 which can be attributed to computational error and approximation error for the Neumann type boundary condition.

In the case of fluorescence dyes models, only the nonlinear WGA migration model was tested as the others are its simplified versions. The maximum value of $0.13 \mu\text{M}$ was attained at the outer boundary of the sphere according to (3.3). The minimum was attained at the inner boundary $r = 0$ and it was slightly negative for some initial iterations ($k < 500$) due to approximation errors for condition (3.3). Correct minimum of 0 was attained at the initial time $k = 0$ as expected.

Table 4.2: Maximum principle is attained for other models presented in the thesis.

Max in inner points	Max at boundary	Min in inner points	Min at boundary
C_{O_2} from the recessed-UME model, recessed by $H_{in} = 2 \mu\text{m}$			
$0.253 + 8.6 \times 10^{-10}$	$0.253 + 8.7 \times 10^{-10}$	3.597×10^{-5}	0
C_{O_2} from the outwarded-UME model, protrusion $H_{out} = 2 \mu\text{m}$			
$0.253 + 2.5 \times 10^{-10}$	$0.253 + 2.7 \times 10^{-10}$	2.817×10^{-5}	0
C_{O_2} from the cone-UME model, cone height $H_{cone} = 2 \mu\text{m}$			
$0.253 + 6.8 \times 10^{-10}$	$0.253 + 6.8 \times 10^{-10}$	3.632×10^{-4}	0
C_{out} from the WGA model. Spheroid radius $R = 134 \mu\text{m}$			
1.290×10^{-7}	1.300×10^{-7}	3.253×10^{-189}	-1.075×10^{-64}

Conservation of mass

Physical systems and their respective differential equations typically follow some law of conservation of mass, energy, etc. [4, 121, 128, 135]. Conservation laws state that physical quantities, such as total mass, energy, the net charge, etc., remain constant as the system evolves,

i.e. differential equations, which govern the system, conserve those quantities.

In the case of SECM at redox competition mode, concentrations of surface-immobilized reagents $C_{GOx^{ox}}$, $C_{GOx \cdot Glc}$, $C_{GOx^{re}}$ and $C_{GOx \cdot O_2}$ conserve the mass. The physical reason for the property is that molecules of glucose oxidase GOx^{ox} and other 3 forms of it are immobilized, i.e. fixed, on the surface, act as a catalyst for Glc/ O_2 reaction and can not be consumed or moved.

Conservation of mass principle is formally derived as follows. Reaction equations (1.6) are summed, which cancels right-hand side terms:

$$\frac{\partial C_{GOx^{ox}}}{\partial t} + \frac{\partial C_{GOx \cdot Glc}}{\partial t} + \frac{\partial C_{GOx^{re}}}{\partial t} + \frac{\partial C_{GOx \cdot O_2}}{\partial t} = 0$$

for $0 < t \leq T$, $0 < r < r_{glass}$. (4.1)

(4.1) is integrated by $\int_0^{\tilde{t}} dt$, where \tilde{t} – any fixed time. Initial conditions (1.8), which sets $C_{GOx^{ox}} = 2.114 \times 10^{-8}$ mol/m² and others to 0, are inserted to obtain the conservation principle:

$$C_{GOx^{ox}} + C_{GOx \cdot Glc} + C_{GOx^{re}} + C_{GOx \cdot O_2} = 2.114 \times 10^{-8} \text{ mol/m}^2$$

for $t = \tilde{t}$, $0 < r < r_{glass}$, (4.2)

which states that at any spatial point r and at time \tilde{t} the total concentration of surface-immobilized reagents remains constant and is equal to initial concentration of GOx^{ox} , i.e. 2.114×10^{-8} mol/m².

Obviously, the numerical solution V_j^k has to retain conservation principle for all $k > 0$, $0 \leq j < N_2$. A numerical version of the principle follows from (4.2), but can be separately derived from approximation formulas (1.37) by summing them and rewriting

$$\begin{aligned} V_{GOx^{ox},j}^{k+1} + V_{GOx \cdot Glc,j}^{k+1} + V_{GOx^{re},j}^{k+1} + V_{GOx \cdot O_2,j}^{k+1} &= \\ &= V_{GOx^{ox},j}^k + V_{GOx \cdot Glc,j}^k + V_{GOx^{re},j}^k + V_{GOx \cdot O_2,j}^k, \end{aligned}$$

for $k = 0, \dots, K - 1$, $j = 0, \dots, N_2 - 1$. (4.3)

We repeatedly insert into (4.3) values at k , $k - 1, \dots, 1$ and then initial condition (1.8) to derive conservation principle for numerical solution

$$\begin{aligned} V_{\text{sum},j}^{k+1} &= V_{GOx^{ox},j}^{k+1} + V_{GOx \cdot Glc,j}^{k+1} + V_{GOx^{re},j}^{k+1} + V_{GOx \cdot O_2,j}^{k+1} = \\ &= 2.114 \times 10^{-8} \text{ mol/m}^2, \quad \textit{for } k = 0, \dots, K, j = 0, \dots, N_2 - 1. \end{aligned}$$
 (4.4)

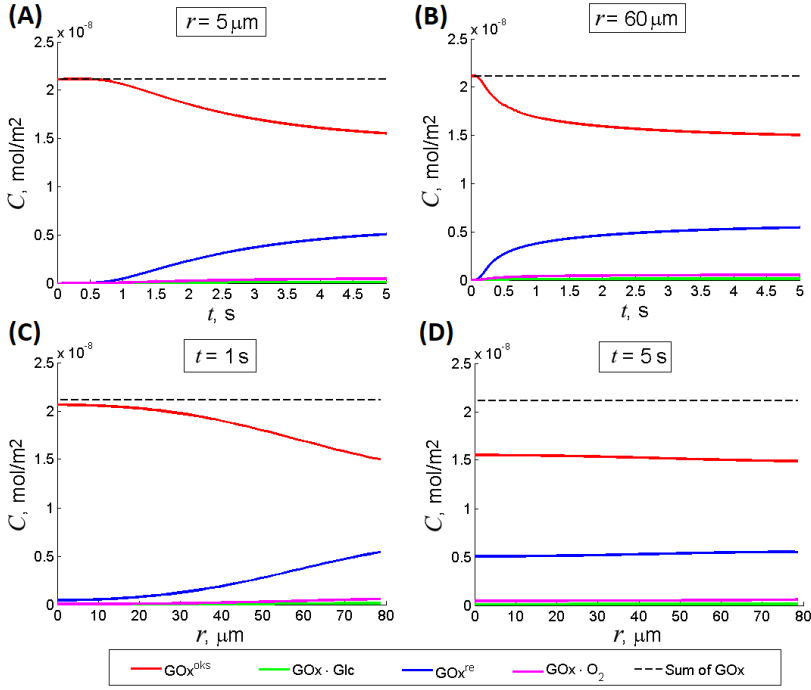


Figure 4.1: Concentrations of surface-immobilized reagents and their sum, which is always at $2.114 \times 10^{-8} \text{ mol/m}^2$. (A)(B) fixed radius, (C)(D) fixed time. Simulations were performed with $Glc_{\text{out}} = 0.6 \text{ mM}$, reaction rate $k_1 = 100 \text{ M}^{-1}\text{s}^{-1}$.

Simulations have been performed to test if the numerical conservation law is upheld. According to the calculations, for exterior Glc concentration $Glc_{\text{out}} = 0.6 \text{ mM}$ (fast reaction):

$$\min_{\substack{0 < k < K \\ 0 \leq j < N_2}} V_{\text{sum}, j}^k = 2.113\,999\,999\,999\,77 \times 10^{-8},$$

$$\max_{\substack{0 < k < K \\ 0 \leq j < N_2}} V_{\text{sum}, j}^k = 2.114\,000\,000\,000\,21 \times 10^{-8}$$

and $Glc_{\text{out}} = 0.2 \text{ mM}$ (slow reaction):

$$\min_{\substack{0 < k < K \\ 0 \leq j < N_2}} V_{\text{sum}, j}^k = 2.113\,999\,999\,999\,66 \times 10^{-8},$$

$$\max_{\substack{0 < k < K \\ 0 \leq j < N_2}} V_{\text{sum}, j}^k = 2.114\,000\,000\,000\,15 \times 10^{-8},$$

which show that at each (k, j) the sum differs from 2.114×10^{-8} only by computational error.

Conservation law is visually demonstrated in Fig. 4.1, where a dashed line represents V_{sum}^k and is always at $2.114 \times 10^{-8} \text{ mol/m}^2$. Therefore, the law of conservation of mass is upheld.

4.2 Convergence of numerical solution

Convergence to exact solution

It is proven (see e.g. [72, 108, 116]), that numerical solutions of PDEs, which are solved in the thesis, converge to exact solutions as the step size approaches 0. In the case of the RC-SECM model,

$$U_{i,j}^k \rightarrow C_{\text{diff}}(t^k, z_i, r_j), V_j^k \rightarrow C_{\text{surf}}(t^k, r_j) \text{ as } K, N_1, N_2 \rightarrow \infty.$$

Obviously, arbitrary large values cannot be chosen in practical computations. The convergence is tested numerically by increasing the number of mesh nodes (i.e. decreasing step size) and analyzing the influence on numerical solution. Typically, mesh size is increased 2 times and then a higher-accuracy solution is compared with a lower-accuracy one in some norm (maximum or L_p).

However, two numerical solutions of SECM models can not be directly compared, because points of non-uniform grids ω_h and $\omega_{h/2}$ do not intersect. Therefore, Solution $U_{i,j}^k$ has to be summed (integrated) by some method. The most natural approach is to use the formula of electric current (1.38):

$$i(t) = 2\pi nFD_{O_2} \int_0^{r_{el}} \frac{\partial C_{O_2}}{\partial z} \Big|_{z=d} r \, dr,$$

because it is the response of SECM experiment and the goal of numerical computations is to calculate it accurately. The norm is defined for the numerical equivalent $I^k \approx i(t^k)$ in order to measure the error

$$\|I\| = \max_{0 \leq k \leq K} I^k. \quad (4.5)$$

The convergence to the exact solution is illustrated in Fig. 4.2 by increasing the size of spatial grid ω_h . Curves of Electric current are moving upwards in both tested cases (Fig. 4.2A,C) and the difference

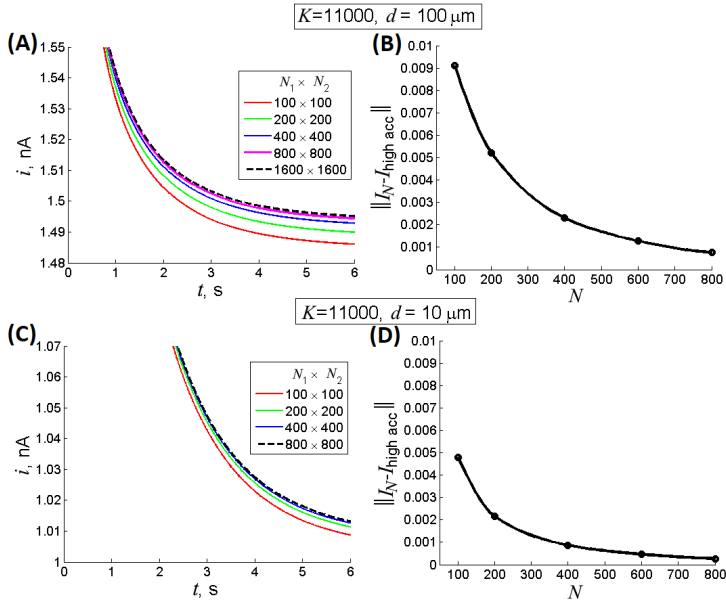


Figure 4.2: Left column: Convergence of current I as size of spatial grid increases, right column: convergence of errors. (A)(B) $d = 100\ \mu\text{m}$, i.e. UME is positioned further from the substrate, (C)(D) $d = 10\ \mu\text{m}$, i.e. UME is positioned close to the substrate. $I_{\text{high acc}}$ – the current, calculated with the highest accuracy grid.

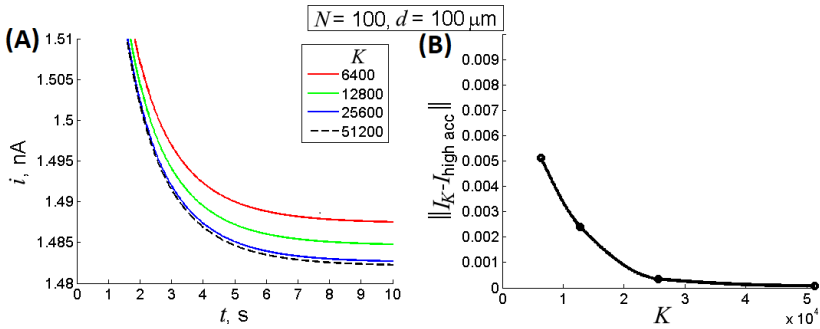


Figure 4.3: (A) convergence of current I as the size of temporal grid increases. (B) convergence of errors. $I_{\text{high acc}}$ is the current, calculated with the highest accuracy grid.

between them decreases as N grows. Absolute errors are calculated in Fig. 4.2B,D using the maximum norm (4.5). It can be concluded that the error approaches 0 as N increases for the spatial grid.

The analysis of the size of temporal grid ω^T demonstrated convergence by temporal variable (Fig. 4.3).

Convergence of non-standard geometry models to the standard-UME model

The numerical solution can be compared with the analytical solution in order to validate the correctness of numerical schemes and test their properties as shown in literature [5, 31, 130]. In more difficult cases, a model can be simplified to the version with a known analytical solution.

According to our knowledge, even a simplified version of UME geometry models, e.g. the standard-UME model, does not have an analytical solution. However, the numerical solution of different models of UME geometries can be compared with the numerical solution of the standard-UME model. It is expected that as the level of imperfectness in the non-standard model approaches 0, measured electric current should coincide with the current of the standard-UME model. It should be noted, that only convergence can be tested because neither 0 imperfectness can be plugged into the model, nor its arbitrary small value due to computational limitations, e.g. all numbers are limited by computer precision. The convergence between models is also not trivial as the discrete grid, numerical schemes and even formula for current calculations are different.

Computer simulations have been performed to test convergence of the cone-UME model to standard-UME at the distance $d = 100 \mu\text{m}$. It is shown in Fig. 4.4A, that electric current, calculated by the cone-UME model, quickly approaches the current of standard-UME if h_{cone} is sufficiently small. In particular, the error of 0.1 %, measured by the norm (4.5), is reached at $h_{cone} = 0.01 \mu\text{m}$, which is about 0.01 % of full distance between the electrode and surface (Fig. 4.4B).

Furthermore, the convergence of the outwarded-UME model has also been tested at the same distance $d = 100 \mu\text{m}$ (Fig. 4.5A). The electric current of the outwarded-UME model approaches standard-UME current much slower and $h_{out} = 10^{-5} \mu\text{m}$ (about 10^{-5} % of full distance) is necessary to reach just 1 % error between models (Fig. 4.5B).

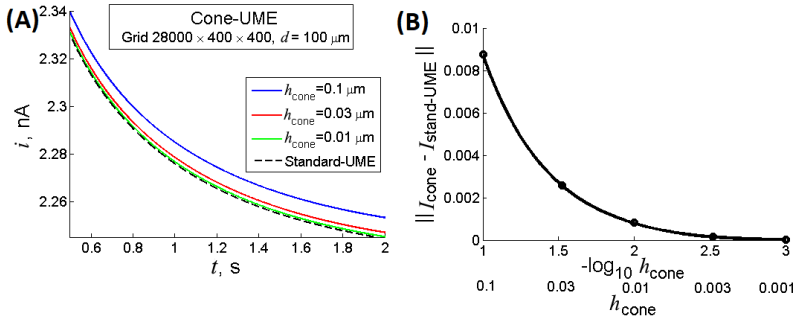


Figure 4.4: Convergence of cone-UME current I_{cone} to the case of standard-UME $I_{\text{stand-UME}}$. (A) electric currents, (B) errors.

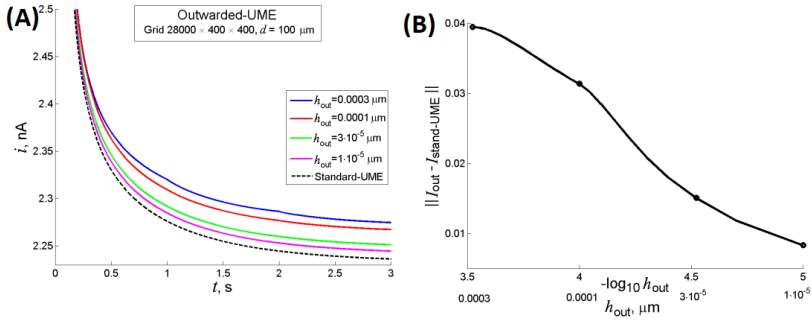


Figure 4.5: Convergence of outwarded-UME current I_{out} to the case of standard-UME $I_{\text{stand-UME}}$. (A) electric currents, (B) errors.

However, the convergence is registered and we conclude that this property holds. The recessed-UME case is not presented, but the model converges quickly due to better numerical properties.

4.3 Method of a test solution

A numerical algorithm, which solves a differential equation, can be verified by inserting some freely chosen function into the differential equation, calculating derivatives and subtracting the error in order for the function to satisfy the equation. Possibly, initial-boundary conditions have to be also modified, but the chosen function should satisfy these conditions to preserve the behaviour and properties of a real solution. Because of complicated boundary conditions and non-rectangular domains, the construction of a test solution is complicated for SECM models, but it can be done for dye penetration models.

In order to test the solution of the WGA model (3.1)–(3.4), equations with their initial-boundary conditions have been modified:

$$\begin{aligned}
\frac{\partial C_{out}}{\partial t} &= D \frac{1}{r^2} \frac{\partial}{\partial r} \left(r^2 \frac{\partial C_{out}}{\partial r} \right) - k_{bind} (B_{max} - C_{bind}) C_{out} + f(t, r) \\
\frac{\partial C_{bind}}{\partial t} &= k_{bind} (B_{max} - C_{bind}) C_{out} \quad \text{for } 0 < t \leq T, \quad 0 < r < R, \\
C_{out} \Big|_{r=R} &= \mu(t), \quad t > 0, \\
\frac{\partial C_{out}}{\partial r} \Big|_{r=0} &= 0, \quad t > 0, \\
C_{out} \Big|_{t=0} &= 0, \quad 0 \leq r \leq R, \\
C_{bind} \Big|_{t=0} &= 0, \quad 0 \leq r \leq R.
\end{aligned} \tag{4.6}$$

The test solution $C_{out} = tr^2$, which satisfies initial-boundary conditions ($\mu(t)$ has to be computed), has been chosen. By plugging it into the 2nd equation of system (4.6), ordinary differential equation is derived as r is considered a parameter:

$$\frac{\partial C_{bind}}{\partial t} = k_{bind} tr^2 (B_{max} - C_{bind}),$$

which is solved by separation of variables method to obtain

$$C_{bind} = B_{max} \left(1 - e^{-0.5k_{bind}t^2r^2} \right).$$

In order for the chosen C_{out} to satisfy (4.6), functions have to be taken

$$\begin{aligned}
f(t, r) &= r^2 - 6Dt + k_{bind} B_{max} tr^2 e^{-0.5k_{bind}t^2r^2}, \\
\mu(t) &= R^2 t.
\end{aligned}$$

The numerical scheme (3.13) have been adjusted according to the changes made. The diffusion equation (4.6) is discretised by

$$\begin{aligned}
\frac{U_i^{k+1} - U_i^k}{\tau} &= D \left(\frac{\bar{U}_{i-1} - 2\bar{U}_i + \bar{U}_{i+1}}{h^2} + \frac{1}{r_i} \frac{\bar{U}_{i+1} - \bar{U}_{i-1}}{h} \right) - \\
&\quad - k_{bind} (B_{max} - \bar{V}_i) \bar{U}_i + f(t^{k+1}, r_i), \quad i = 1, \dots, N-1,
\end{aligned}$$

and at the boundary $r = R$ approximation $U_N^k = \mu(t^k)$ for $k = 0, \dots, K$ is used. However, these modifications do not change the algorithm and the approximation error of second order is retained.

In order to compare numerical solutions U and V with exact solutions C_{out} and C_{bind} , relative error in the maximum norm is calculated by

$$\|\varepsilon_U\| = \max_{\substack{0 \leq k \leq K \\ 0 \leq i \leq N}} |U_i^k - C_{out}(t^k, r_i)|$$

$$\|\varepsilon_V\| = \max_{\substack{0 \leq k \leq K \\ 0 \leq i \leq N}} |V_i^k - C_{bind}(t^k, r_i)|.$$

The ratio between errors of grids of different size is used to evaluate order of the method

$$\theta = \frac{\|\varepsilon\|_{K \times N}}{\|\varepsilon\|_{2K \times 2N}},$$

where $\|\varepsilon\|_{K \times N}$ denotes the error of $(K \times N)$ -sized grid.

Simulations have been performed using increasingly larger grids and results are shown in Table 4.3. It is evident that the errors $\|\varepsilon_U\|$ and $\|\varepsilon_V\|$ for both solutions C_{out} and C_{bind} are small and tend to 0 as the size of grid increases. Moreover, the ratio between errors θ is ~ 4 , then the size of the grid is increased by 2 in both directions. It shows that the order of approximation error is second, i.e. the error is $\mathcal{O}(\tau^2 + h^2)$ as theoretically predicted.

Table 4.3: Errors between the numerical and exact solution depending on the grid size for functions C_{out} and C_{bind} .

K	N	$\ \varepsilon_U\ $	θ_U	$\ \varepsilon_V\ $	θ_V
1000	100	8.94×10^{-14}		1.11×10^{-12}	
2000	200	2.23×10^{-14}	4.009	2.78×10^{-13}	3.993
4000	400	5.59×10^{-15}	3.989	6.94×10^{-14}	4.006
8000	800	1.40×10^{-15}	3.993	1.74×10^{-14}	3.989

General conclusions

Three mathematical and numerical models were presented in the thesis: (i) SECM acting in the redox-competition mode (RC-SECM mode), (ii) geometry of SECM electrodes and (iii) the uptake of dyes into cell spheroids. The models were written using reaction-diffusion equations, which were solved by numerical methods. In all cases, computer simulations were compared with real physical experiments and good agreement was achieved to demonstrate the credibility of the models. Finally, a number of numerical experiments were provided to analyse the properties of the modelled systems. Following general conclusions were made:

- The novel computer model of SECM is an appropriate tool for investigation of RC-SECM mode behaviour and determination of reaction and diffusion coefficients. In particular, the diffusion coefficient of oxygen is inversely proportional to the concentration of glucose in the medium and the formula to calculate this coefficient has been proposed for the RC-SECM mode. Calculations show that electric signal, measured by SECM electrode, significantly decreases due to the presence of glucose or other materials.
- Mathematical models, which describe three most common non-standard geometries of ultramicroelectrode (UME), is an applicable technique to evaluate the difference from standard-UME in electric current measured by SECM electrodes. It was determined, that outwarded-UME provides the highest measurement errors, whereas errors of recessed-UME and cone-UME experiments are approximately 2 times lower with the same level of deviation from standard UME.
- Using the model of R6G dye uptake into cellular spheroids, the diffusion coefficient in the cellular matrix has been calculated and it is about 4 times higher than the diffusion coefficient of cells, used in the experiment. By analysing accumulation dynamics into

spheroids, time necessary to incubate the centre zone of the spheroid is calculated, which is relevant for the practical application of fluorescent dyes in chemotherapeutic drug research. It is shown that the dynamics also strongly depend on the size and density of the spheroid.

- The dynamics of WGA-Alexa488 dye penetration into the spheroid is analysed using a nonlinear case of the model. The effect of binding rate and the number of binding sites on penetration dynamics is shown to be nonlinear because of the process of binding to the cells.

Bibliography

- [1] T.-M. Achilli, S. McCalla, J. Meyer, A. Tripathi, and J. R. Morgan. Multilayer spheroids to quantify drug uptake and diffusion in 3D. *Molecular Pharmaceutics*, 11(7):2071–2081, 2014.
- [2] A. Agrawal and R. Peckover. Nonuniform grid generation for boundary-layer problems. *Computer Physics Communications*, 19(2):171–178, 1980.
- [3] J. L. Amphlett and G. Denuault. Scanning electrochemical microscopy (SECM): An investigation of the effects of tip geometry on amperometric tip response. *The Journal of Physical Chemistry B*, 102(49):9946–9951, 1998.
- [4] S. C. Anco and G. Bluman. Direct construction method for conservation laws of partial differential equations. Part I: Examples of conservation law classifications. *arXiv preprint math-ph/0108023*, 2001.
- [5] B. S. Anglin, R. A. Lebensohn, and A. D. Rollett. Validation of a numerical method based on Fast Fourier Transforms for heterogeneous thermoelastic materials by comparison with analytical solutions. *Computational Materials Science*, 87:209–217, 2014.
- [6] Y. G. Anissimov, X. Zhao, M. S. Roberts, and A. V. Zvyagin. Fluorescence recovery after photo-bleaching as a method to determine local diffusion coefficient in the stratum corneum. *International Journal of Pharmaceutics*, 435(1):93–97, 2012.
- [7] V. Ašeris, E. Gaidamauskaitė, J. Kulys, and R. Baronas. Modelling glucose dehydrogenase-based amperometric biosensor utilizing synergistic substrates conversion. *Electrochimica Acta*, 146:752–758, 2014.
- [8] M. J. Baines, M. E. Hubbard, and P. K. Jimack. A moving mesh finite element algorithm for the adaptive solution of time-dependent partial differential equations with moving boundaries. *Applied Numerical Mathematics*, 54(3-4):450–469, 2005.
- [9] G. Bains, R. T. Lee, Y. C. Lee, and E. Freire. Microcalorimetric study of wheat germ agglutinin binding to N-acetylglucosamine and its oligomers. *Biochemistry*, 31(50):12624–12628, 1992.

- [10] W. Bangerth and R. Rannacher. *Adaptive finite element methods for differential equations*. Birkhäuser, 2013.
- [11] A. J. Bard and M. V. Mirkin. *Scanning electrochemical microscopy*. CRC Press, 2012.
- [12] A. J. Bard, F. R. F. Fan, J. Kwak, and O. Lev. Scanning electrochemical microscopy. Introduction and principles. *Analytical Chemistry*, 61(2):132–138, 1989.
- [13] A. J. Bard, M. V. Mirkin, P. R. Unwin, and D. O. Wipf. Scanning electrochemical microscopy. 12. Theory and experiment of the feedback mode with finite heterogeneous electron-transfer kinetics and arbitrary substrate size. *The Journal of Physical Chemistry*, 96(4):1861–1868, 1992.
- [14] R. Baronas, F. Ivanauskas, and J. Kulys. The influence of the enzyme membrane thickness on the response of amperometric biosensors. *Sensors*, 3(7):248–262, 2003.
- [15] R. Baronas, F. Ivanauskas, J. Kulys, and M. Sapagovas. Modelling of amperometric biosensors with rough surface of the enzyme membrane. *Journal of Mathematical Chemistry*, 34(3-4):227–242, 2003.
- [16] R. Baronas, J. Kulys, and F. Ivanauskas. Modelling amperometric enzyme electrode with substrate cyclic conversion. *Biosensors and Bioelectronics*, 19(8):915–922, 2004.
- [17] R. Baronas, F. Ivanauskas, and J. Kulys. Mathematical modeling of biosensors based on an array of enzyme microreactors. *Sensors*, 6(4):453–465, 2006.
- [18] R. Baronas, J. Kulys, and F. Ivanauskas. Computational modelling of biosensors with perforated and selective membranes. *Journal of Mathematical Chemistry*, 39(2):345–362, 2006.
- [19] R. Baronas, F. Ivanauskas, and J. Kulys. *Mathematical modeling of biosensors: An introduction for chemists and mathematicians*, volume 9. Springer Science & Business Media, 2009.
- [20] P. Bartlett and S. Taylor. An accurate microdisc simulation model for recessed microdisc electrodes. *Journal of Electroanalytical Chemistry*, 453(1-2):49–60, 1998. doi: 10.1016/S0022-0728(98)00242-3.
- [21] P. N. Bartlett, C. S. Toh, E. J. Calvo, and V. Flexer. *Modelling biosensor responses*. Wiley: Chichester, England, 2008.
- [22] R. Becker, H. Kapp, and R. Rannacher. Adaptive finite element methods for optimal control of partial differential equations: Basic concept. *SIAM Journal on Control and Optimization*, 39(1):113–132, 2000.
- [23] L. Beilina. Energy estimates and numerical verification of the stabilized domain decomposition finite element/finite difference approach for time-dependent Maxwell’s system. *Central European*

- Journal of Mathematics*, 11(4):702–733, 2013.
- [24] H. Ben-Yoav, A. Biran, M. Sternheim, S. Belkin, A. Freeman, and Y. Shacham-Diamand. Functional modeling of electrochemical whole-cell biosensors. *Sensors and Actuators B: Chemical*, 181:479–485, 2013.
- [25] M. J. Berger and J. Olinger. Adaptive mesh refinement for hyperbolic partial differential equations. *Journal of Computational Physics*, 53(3):484–512, 1984.
- [26] A. M. Bond, D. Luscombe, K. B. Oldham, and C. G. Zoski. A comparison of the chronoamperometric response at inlaid and recessed disc microelectrodes. *Journal of Electroanalytical Chemistry and Interfacial Electrochemistry*, 249(1-2):1–14, 1988.
- [27] H. J. Bright and Q. H. Gibson. The oxidation of 1-deuterated glucose by glucose oxidase. *Journal of Biological Chemistry*, 242(5):994–1003, 1967.
- [28] D. Britz, R. Baronas, E. Gaidamauskaitė, and F. Ivanauskas. Further comparisons of finite difference schemes for computational modelling of biosensors. *Nonlinear Analysis: Modelling and Control*, 14(4):419–433, 2009.
- [29] E. Bueler, C. S. Lingle, J. A. Kallen-Brown, D. N. Covey, and L. N. Bowman. Exact solutions and verification of numerical models for isothermal ice sheets. *Journal of Glaciology*, 51(173):291–306, 2005.
- [30] J. C. Caendish, D. A. Field, and W. H. Frey. An approach to automatic three-dimensional finite element mesh generation. *International Journal for Numerical Methods in Engineering*, 21(2):329–347, 1985.
- [31] G. Carbone, M. Scaraggi, and U. Tartaglino. Adhesive contact of rough surfaces: comparison between numerical calculations and analytical theories. *The European Physical Journal E*, 30(1):65–74, 2009.
- [32] G. Cernansky, D.-F. Liau, S. A. Hashim, and S. F. Ryan. Estimation of phosphatidylglycerol in fluids containing pulmonary surfactant. *Journal of Lipid Research*, 21(8):1128–1131, 1980.
- [33] P. L. Chariou, K. L. Lee, J. K. Pokorski, G. M. Saidel, and N. F. Steinmetz. Diffusion and uptake of tobacco mosaic virus as therapeutic carrier in tumor tissue: Effect of nanoparticle aspect ratio. *The Journal of Physical Chemistry B*, 120(26):6120–6129, 2016.
- [34] R. T. Cheng, V. Casulli, and J. W. Gartner. Tidal, residual, intertidal mudflat (TRIM) model and its applications to San Francisco Bay, California. *Estuarine, Coastal and Shelf Science*, 36(3):235–280, 1993.
- [35] Y. Chenyakin, D. A. Ullmann, E. Evoy, L. Renbaum-Wolff, S. Kamal, and A. K. Bertram. Diffusion coefficients of organic molecules in sucrose-water solutions and comparison with Stokes–

- Einstein predictions. *Atmospheric Chemistry and Physics*, 17(3): 2423–2435, 2017.
- [36] R. Čiegis. *Diferencialinių lygčių skaitiniai sprendimo metodai (Numerical Methods for Differential Equations)*. Technika, Vilnius, Lithuania, 2003.
- [37] R. Cornut and C. Lefrou. New analytical approximation of feedback approach curves with a microdisk SECM tip and irreversible kinetic reaction at the substrate. *Journal of Electroanalytical Chemistry*, 621(2):178–184, 2008.
- [38] R. Cornut, P. Hapiot, and C. Lefrou. Enzyme-mediator kinetics studies with SECM: Numerical results and procedures to determine kinetics constants. *Journal of Electroanalytical Chemistry*, 633(1): 221–227, 2009.
- [39] R. Cornut, A. Bhasin, S. Lhenry, M. Etienne, and C. Lefrou. Accurate and simplified consideration of the probe geometrical defaults in scanning electrochemical microscopy: Theoretical and experimental investigations. *Analytical Chemistry*, 83(24):9669–9675, 2011. doi: 10.1021/ac2026018.
- [40] R. Cornut, S. Poirier, and J. Mauzeroll. Forced convection during feedback approach curve measurements in scanning electrochemical microscopy: Maximal displacement velocity with a microdisk. *Analytical Chemistry*, 84(8):3531–3537, 2012.
- [41] R. Daniel, R. Almog, A. Ron, S. Belkin, and Y. S. Diamand. Modeling and measurement of a whole-cell bioluminescent biosensor based on a single photon avalanche diode. *Biosensors and Bioelectronics*, 24(4):882–887, 2008.
- [42] S. R. Deshmukh, A. B. Mhadeshwar, and D. G. Vlachos. Microreactor modeling for hydrogen production from ammonia decomposition on ruthenium. *Industrial & Engineering Chemistry Research*, 43(12):2986–2999, 2004.
- [43] J. C. Dittmer and R. L. Lester. A simple, specific spray for the detection of phospholipids on thin-layer chromatograms. *Journal of Lipid Research*, 5(1):126–127, 1964.
- [44] K. Eckhard and W. Schuhmann. Localised visualisation of O₂ consumption and H₂O₂ formation by means of SECM for the characterisation of fuel cell catalyst activity. *Electrochimica Acta*, 53(3):1164–1169, 2007.
- [45] K. Eckhard, X. Chen, F. Turcu, and W. Schuhmann. Redox competition mode of scanning electrochemical microscopy (RC-SECM) for visualisation of local catalytic activity. *Physical Chemistry Chemical Physics*, 8(45):5359–5365, 2006.
- [46] R. Edmondson, J. J. Broglie, A. F. Adcock, and L. Yang. Three-dimensional cell culture systems and their applications in drug

- discovery and cell-based biosensors. *ASSAY and Drug Development Technologies*, 12(4):207–218, 2014.
- [47] M. A. Edwards, S. Martin, A. L. Whitworth, J. V. Macpherson, and P. R. Unwin. Scanning electrochemical microscopy: principles and applications to biophysical systems. *Physiological Measurement*, 27(12):R63–R108, 2006. doi: 10.1088/0967-3334/27/12/R01.
- [48] L. C. Evans. *Partial Differential Equations*. Graduate studies in mathematics. American Mathematical Society, 2010.
- [49] S. A. G. Evans, K. Brakha, M. Billon, P. Mailley, and G. Denuault. Scanning electrochemical microscopy (SECM): localized glucose oxidase immobilization via the direct electrochemical microspotting of polypyrrole–biotin films. *Electrochemistry Communications*, 7(2):135–140, 2005.
- [50] M. Faghri, E. M. Sparrow, and A. T. Prata. Finite-difference solutions of convection-diffusion problems in irregular domains, using a nonorthogonal coordinate transformation. *Numerical Heat Transfer*, 7(2):183–209, 1984.
- [51] B. Farkas, R. Singh, and T. Rumsey. Modeling heat and mass transfer in immersion frying. II, model solution and verification. *Journal of Food Engineering*, 29(2):227–248, 1996.
- [52] R. Fazio and A. Jannelli. Finite difference schemes on quasi-uniform grids for BVPs on infinite intervals. *Journal of Computational and Applied Mathematics*, 269:14–23, 2014.
- [53] R. Fazio, A. Jannelli, and S. Agreste. A finite difference method on non-uniform meshes for time-fractional advection–diffusion equations with a source term. *Applied Sciences*, 8(6):960, 2018.
- [54] J. L. Fernandez and A. J. Bard. Scanning electrochemical microscopy. 47. Imaging electrocatalytic activity for oxygen reduction in an acidic medium by the tip generation-substrate collection mode. *Analytical Chemistry*, 75(13):2967–2974, 2003.
- [55] R. Ferrigno, P. Brevet, and H. Girault. Finite element simulation of the chronoamperometric response of recessed and protruding microdisc electrodes. *Electrochimica Acta*, 42(12):1895–1903, 1997.
- [56] L. Gamet, F. Ducros, F. Nicoud, and T. Poinso. Compact finite difference schemes on non-uniform meshes. Application to direct numerical simulations of compressible flows. *International Journal for Numerical Methods in Fluids*, 29(2):159–191, 1999.
- [57] P. Ganguly and N. G. Fossett. The role of sialic acid in the activation of platelets by wheat germ agglutinin. *Blood*, 63(1):181–187, 1984.
- [58] Y. Gao, M. Li, B. Chen, Z. Shen, P. Guo, M. G. Wientjes, and J. L.-S. Au. Predictive models of diffusive nanoparticle transport in 3-dimensional tumor cell spheroids. *The AAPS Journal*, 15(3):

- 816–831, 2013.
- [59] P.-O. Gendron, F. Avaltroni, and K. J. Wilkinson. Diffusion coefficients of several rhodamine derivatives as determined by pulsed field gradient–nuclear magnetic resonance and fluorescence correlation spectroscopy. *Journal of Fluorescence*, 18(6):1093–1101, 2008.
- [60] C. Geuzaine and J.-F. Remacle. Gmsh: A 3-D finite element mesh generator with built-in pre- and post-processing facilities. *International Journal for Numerical Methods in Engineering*, 79(11):1309–1331, 2009.
- [61] Q. H. Gibson, B. E. P. Swoboda, and V. Massey. Kinetics and mechanism of action of glucose oxidase. *Journal of Biological Chemistry*, 239(11):3927–3934, 1964.
- [62] C. Goldstein. The finite element method with nonuniform mesh sizes for unbounded domains. *Mathematics of Computation*, 36(154):387–404, 1981.
- [63] C. Goldstein. The finite element method with non-uniform mesh sizes applied to the exterior helmholtz problem. *Numerische Mathematik*, 38(1):61–82, 1982.
- [64] Y. González-García, S. J. García, A. E. Hughes, and J. M. C. Mol. A combined redox-competition and negative-feedback SECM study of self-healing anticorrosive coatings. *Electrochemistry Communications*, 13(10):1094–1097, 2011.
- [65] T. T. Goodman, J. Chen, K. Matveev, and S. H. Pun. Spatio-temporal modeling of nanoparticle delivery to multicellular tumor spheroids. *Biotechnology and Bioengineering*, 101(2):388–399, 2008.
- [66] C. P. Graff and K. D. Wittrup. Theoretical analysis of antibody targeting of tumor spheroids: importance of dosage for penetration, and affinity for retention. *Cancer Research*, 63(6):1288–1296, 2003.
- [67] D. R. Grimes, C. Kelly, K. Bloch, and M. Partridge. A method for estimating the oxygen consumption rate in multicellular tumour spheroids. *Journal of The Royal Society Interface*, 11(92):20131124, 2014.
- [68] L. Guadagnini, A. Maljusch, X. Chen, S. Neugebauer, D. Tonelli, and W. Schuhmann. Visualization of electrocatalytic activity of microstructured metal hexacyanoferrates by means of redox competition mode of scanning electrochemical microscopy (RC-SECM). *Electrochimica Acta*, 54(14):3753–3758, 2009.
- [69] W. Hackbusch. *Elliptic differential equations: theory and numerical treatment*, volume 18. Springer, 2017.
- [70] J. Heinze and M. Störzbach. Electrochemistry at ultramicroelectrodes—simulation of heterogeneous and homogeneous kinetics by an improved ADI—technique. *Berichte der Bunsengesellschaft für physikalische Chemie*, 90(11):1043–1048,

- 1986.
- [71] N. J. Higham. *Accuracy and stability of numerical algorithms*. SIAM, 2002.
 - [72] W. H. Hundsdorfer and J. G. Verwer. Stability and convergence of the Peaceman-Rachford ADI method for initial-boundary value problems. *Mathematics of Computation*, 53(187):81–101, 1989.
 - [73] B. Hunt. Finite difference approximation of boundary conditions along irregular boundaries. *International Journal for Numerical Methods in Engineering*, 12(2):229–235, 1978.
 - [74] F. Ivanauskas, I. Morkvenaite-Vilkonciene, R. Astrauskas, and A. Ramanavicius. Modelling of scanning electrochemical microscopy at redox competition mode using diffusion and reaction equations. *Electrochimica Acta*, 222:347–354, 2016. doi: 10.1016/j.electacta.2016.10.179.
 - [75] M. Jamnongwong, K. Loubiere, N. Dietrich, and G. Hébrard. Experimental study of oxygen diffusion coefficients in clean water containing salt, glucose or surfactant: Consequences on the liquid-side mass transfer coefficients. *Chemical Engineering Journal*, 165(3):758–768, 2010.
 - [76] A. Jannelli and R. Fazio. Adaptive stiff solvers at low accuracy and complexity. *Journal of Computational and Applied Mathematics*, 191(2):246–258, 2006.
 - [77] G. Jarockyte, D. Dapkute, V. Karabanovas, J. V. Daugmaudis, F. Ivanauskas, and R. Rotomskis. 3D cellular spheroids as tools for understanding carboxylated quantum dot behavior in tumors. *Biochimica et Biophysica Acta (BBA) - General Subjects*, 1862(4):914–923, 2018.
 - [78] L. Jianchun, G. A. Pope, and K. Sepehrnoori. A high-resolution finite-difference scheme for nonuniform grids. *Applied Mathematical Modelling*, 19(3):162–172, 1995.
 - [79] G. N. Jovanovic, P. Žnidaršič Plazl, P. Sakrithichai, and K. Al-Khaldi. Dechlorination of p-chlorophenol in a microreactor with bimetallic Pd/Fe catalyst. *Industrial & Engineering Chemistry Research*, 44(14):5099–5106, 2005.
 - [80] A. Kaffash, K. Rostami, and H. R. Zare. Modeling of an electrochemical nanobiosensor in COMSOL Multiphysics to determine phenol in the presence of horseradish peroxidase enzyme. *Enzyme and Microbial Technology*, 121:23–28, 2019.
 - [81] N. S. Kaisare, J. H. Lee, and A. G. Fedorov. Hydrogen generation in a reverse-flow microreactor: 1. Model formulation and scaling. *AIChE Journal*, 51(8):2254–2264, 2005.
 - [82] K. Karnicka, K. Eckhard, D. A. Guschin, L. Stoica, P. J. Kulesza, and W. Schuhmann. Visualisation of the local bio-electrocatalytic

- activity in biofuel cell cathodes by means of redox competition scanning electrochemical microscopy (RC-SECM). *Electrochemistry Communications*, 9(8):1998–2002, 2007.
- [83] J. P. Kleijnen. Verification and validation of simulation models. *European Journal of Operational Research*, 82(1):145–162, 1995.
- [84] T. Krauthammer. Accuracy of the finite element method near a curved boundary. *Computers & Structures*, 10(6):921–929, 1979.
- [85] B. H. Kueper and E. O. Frind. Two-phase flow in heterogeneous porous media: 1. Model development. *Water Resources Research*, 27(6):1049–1057, 1991.
- [86] J. Kwak and A. J. Bard. Scanning electrochemical microscopy. Theory of the feedback mode. *Analytical Chemistry*, 61(11):1221–1227, 1989.
- [87] F. O. Laforge, P. Sun, and M. V. Mirkin. Physicochemical applications of scanning electrochemical microscopy. *Advances in Chemical Physics*, 139:177–244, 2008.
- [88] K. Leonhardt, A. Avdic, A. Lugstein, I. Pobelov, T. Wandlowski, M. Wu, B. Gollas, and G. Denuault. Atomic force microscopy-scanning electrochemical microscopy: influence of tip geometry and insulation defects on diffusion controlled currents at conical electrodes. *Analytical Chemistry*, 83(8):2971–2977, 2011. doi: 10.1021/ac103083y.
- [89] V. Leskovac, S. Trivić, G. Wohlfahrt, J. Kandrač, and D. Peričin. Glucose oxidase from *Aspergillus niger*: the mechanism of action with molecular oxygen, quinones, and one-electron acceptors. *The International Journal of Biochemistry & Cell Biology*, 37(4):731–750, 2005.
- [90] P. Liljeroth, C. Johans, C. J. Slevin, B. M. Quinn, and K. Kontturi. Disk-generation/ring-collection scanning electrochemical microscopy: theory and application. *Analytical Chemistry*, 74(9):1972–1978, 2002.
- [91] G. Lindsey, S. Abercrombie, G. Denuault, S. Daniele, and E. De Faveri. Scanning electrochemical microscopy: approach curves for sphere-cap scanning electrochemical microscopy tips. *Analytical Chemistry*, 79(7):2952–2956, 2007. doi: 10.1021/ac061427c.
- [92] N. Martens and E. A. H. Hall. Model for an immobilized oxidase enzyme electrode in the presence of two oxidants. *Analytical Chemistry*, 66(17):2763–2770, 1994.
- [93] R. D. Martin and P. R. Unwin. Scanning electrochemical microscopy: theory and experiment for the positive feedback mode with unequal diffusion coefficients of the redox mediator couple. *Journal of Electroanalytical Chemistry*, 439(1):123–136, 1997.

- [94] R. D. Martin and P. R. Unwin. Theory and experiment for the substrate generation/tip collection mode of the scanning electrochemical microscope: Application as an approach for measuring the diffusion coefficient ratio of a redox couple. *Analytical Chemistry*, 70(2):276–284, 1998.
- [95] Y. Masuda and T. Oguma. Examination of intrahepatic flow distribution by vital staining with rhodamine 6G in isolated perfused rat liver. *The Japanese Journal of Pharmacology*, 83(3):215–224, 2000.
- [96] K. McKelvey, M. A. Edwards, and P. R. Unwin. Intermittent contact-scanning electrochemical microscopy (IC-SECM): a new approach for tip positioning and simultaneous imaging of interfacial topography and activity. *Analytical Chemistry*, 82(15): 6334–6337, 2010.
- [97] M. M. Miller, G. A. Prinz, S.-F. Cheng, and S. Bounnak. Detection of a micron-sized magnetic sphere using a ring-shaped anisotropic magnetoresistance-based sensor: A model for a magnetoresistance-based biosensor. *Applied Physics Letters*, 81(12):2211–2213, 2002.
- [98] M. V. Mirkin and A. J. Bard. Multidimensional integral equations: a new approach to solving microelectrode diffusion problems: part 2. Applications to microband electrodes and the scanning electrochemical microscope. *Journal of Electroanalytical Chemistry*, 323(1?2):29–51, 1992. ISSN 1572-6657. doi: 10.1016/0022-0728(92)80002-L.
- [99] I. Morkvenaite-Vilkonciene, A. Ramanaviciene, and A. Ramanavicius. Redox competition and generation-collection modes based scanning electrochemical microscopy for the evaluation of immobilised glucose oxidase-catalysed reactions. *RSC Advances*, 4(91): 50064–50069, 2014.
- [100] I. Morkvenaite-Vilkonciene, P. Genys, A. Ramanaviciene, and A. Ramanavicius. Scanning electrochemical impedance microscopy for investigation of glucose oxidase catalyzed reaction. *Colloids and Surfaces B: Biointerfaces*, 126:598–602, 2015.
- [101] K. Morton and D. Mayers. *Numerical Solution of Partial Differential Equations: An Introduction*. Cambridge University Press, 2005. ISBN 9781139443203.
- [102] V. Nabaei, R. K. Rajkumar, A. Manzin, O. Kazakova, and A. Tzalenchuk. Optimization of Hall bar response to localized magnetic and electric fields. *Journal of Applied Physics*, 113(6), 2013.
- [103] V. Nabaei, R. Chandrawati, and H. Heidari. Magnetic biosensors: Modelling and simulation. *Biosensors and Bioelectronics*, 103:69–86, 2018.
- [104] Y. Nagata and M. M. Burger. Wheat germ agglutinin molecu-

- lar characteristics and specificity for sugar binding. *Journal of Biological Chemistry*, 249(10):3116–3122, 1974.
- [105] T. Nann and J. Heinze. Simulation in electrochemistry using the finite element method: Part 1: The algorithm. *Electrochemistry Communications*, 1(7):289–294, 1999.
- [106] T. Nann and J. Heinze. Simulation in electrochemistry using the finite element method part 2: scanning electrochemical microscopy. *Electrochimica Acta*, 48(27):3975–3980, 2003.
- [107] B. Noye and R. Arnold. Accurate finite difference approximations for the Neumann condition on a curved boundary. *Applied Mathematical Modelling*, 14(1):2–13, 1990.
- [108] D. W. Peaceman and H. H. Rachford, Jr. The numerical solution of parabolic and elliptic differential equations. *Journal of the Society for Industrial and Applied Mathematics*, 3(1):28–41, 1955.
- [109] Z. Petrášek and P. Schwillé. Precise measurement of diffusion coefficients using scanning fluorescence correlation spectroscopy. *Biophysical Journal*, 94(4):1437–1448, 2008.
- [110] D. T. Pierce, P. R. Unwin, and A. J. Bard. Scanning electrochemical microscopy. 17. Studies of enzyme-mediator kinetics for membrane- and surface-immobilized glucose oxidase. *Analytical Chemistry*, 64(17):1795–1804, 1992.
- [111] R. Popovtzer, A. Natan, and Y. Shacham-Diamand. Mathematical model of whole cell based bio-chip: An electrochemical biosensor for water toxicity detection. *Journal of Electroanalytical Chemistry*, 602(1):17–23, 2007.
- [112] F. L. Qiu and A. C. Fisher. The boundary element method: chronoamperometric simulations at microelectrodes. *Electrochemistry Communications*, 5(1):87–93, 2003.
- [113] A. Quarteroni, R. Sacco, and F. Saleri. *Numerical mathematics*, volume 37. Springer Science & Business Media, 2010.
- [114] A. Rabner, E. Martinez, R. Pedhazur, T. Elad, S. Belkin, and Y. Shacham. Mathematical modeling of a bioluminescent E. coli based biosensor. *Nonlinear Analysis: Modelling and Control*, 14: 505–529, 2009.
- [115] C. Saengkhae, C. Loetchutinat, and A. Garnier-Suillerot. Kinetic analysis of rhodamines efflux mediated by the multidrug resistance protein (MRP1). *Biophysical Journal*, 85(3):2006–2014, 2003.
- [116] A. A. Samarskii. *The theory of difference schemes*, volume 240. CRC Press, 2001.
- [117] C. M. Sánchez-Sánchez, J. Rodríguez-López, and A. J. Bard. Scanning electrochemical microscopy. 60. Quantitative calibration of the SECM substrate generation/tip collection mode and its use for the study of the oxygen reduction mechanism. *Analytical Chem-*

- istry, 80(9):3254–3260, 2008.
- [118] R. G. Sargent. Verification and validation of simulation models. In *Proceedings of the 2010 winter simulation conference*, pages 166–183. IEEE, 2010.
- [119] T. Schulmeister and D. Pfeiffer. Mathematical modelling of amperometric enzyme electrodes with perforated membranes. *Bio-sensors and Bioelectronics*, 8(2):75–79, 1993.
- [120] Y. Selzer and D. Mandler. Scanning electrochemical microscopy. Theory of the feedback mode for hemispherical ultramicroelectrodes: Steady-state and transient behavior. *Analytical Chemistry*, 72(11):2383–2390, 2000.
- [121] L. F. Shampine. Conservation laws and the numerical solution of ODEs. *Computers & Mathematics with Applications*, 12(5-6):1287–1296, 1986.
- [122] R. Šimkus, R. Baronas, and Ž. Ledas. A multi-cellular network of metabolically active *E. coli* as a weak gel of living Janus particles. *Soft Matter*, 9(17):4489–4500, 2013.
- [123] O. Sklyar and G. Wittstock. Numerical simulations of complex nonsymmetrical 3D systems for scanning electrochemical microscopy using the boundary element method. *The Journal of Physical Chemistry B*, 106(30):7499–7508, 2002.
- [124] O. Sklyar, J. Ufheil, J. Heinze, and G. Wittstock. Application of the boundary element method numerical simulations for characterization of heptode ultramicroelectrodes in SECM experiments. *Electrochimica Acta*, 49(1):117–128, 2003.
- [125] O. Sklyar, A. Kueng, C. Kranz, B. Mizaikoff, A. Lugstein, E. Bertagnolli, and G. Wittstock. Numerical simulation of scanning electrochemical microscopy experiments with frame-shaped integrated atomic force microscopy-SECM probes using the boundary element method. *Analytical Chemistry*, 77(3):764–771, 2005.
- [126] E. S. Smotkin, F. T. Moy, and W. Z. Plachy. Dioxygen solubility in aqueous phosphatidylcholine dispersions. *Biochimica et Biophysica Acta (BBA)-Biomembranes*, 1061(1):33–38, 1991.
- [127] W. D. Stein and T. Litman. *Channels, carriers, and pumps: an introduction to membrane transport*. Elsevier, 2014.
- [128] W. A. Strauss. *Partial differential equations: An introduction*. John Wiley & Sons, 2007.
- [129] Y. Su. Modeling and characteristic study of thin film based biosensor based on COMSOL. *Mathematical Problems in Engineering*, 2014, 2014.
- [130] N. H. Sweilam, M. M. Khader, and A. M. S. Mahdy. Crank-Nicolson finite difference method for solving time-fractional diffusion equation. *Journal of Fractional Calculus and Applications*, 2(2):

- 1–9, 2012.
- [131] R. Teranishi, E. Higuchi, M. Chiku, and H. Inoue. Analysis of kinetics of oxygen reduction reaction in alkaline solution by scanning electrochemical microscopy. *Ecs Transactions*, 41(1):2179–2184, 2011.
- [132] B. H. Thacker, S. W. Doebeling, F. M. Hemez, M. C. Anderson, J. E. Pepin, and E. A. Rodriguez. Concepts of model verification and validation. Technical report, Los Alamos National Lab., 2004.
- [133] M. Tišma, B. Zelić, D. Vasić-Rački, P. Žnidaršič Plazl, and I. Plazl. Modelling of laccase-catalyzed L-DOPA oxidation in a microreactor. *Chemical Engineering Journal*, 149(1-3):383–388, 2009.
- [134] A. O. Tjell and K. Almdal. Diffusion rate of hydrogen peroxide through water-swelled polyurethane membranes. *Sensing and bio-sensing research*, 21:35–39, 2018.
- [135] G. A. Truskey, F. Yuan, and D. F. Katz. *Transport phenomena in biological systems*. Pearson/Prentice Hall, 2004.
- [136] E. Turkel. Accuracy of schemes with nonuniform meshes for compressible fluid flows. *Applied Numerical Mathematics*, 2(6): 529–550, 1986.
- [137] B. Ungerböck, A. Pohar, T. Mayr, and I. Plazl. Online oxygen measurements inside a microreactor with modeling of transport phenomena. *Microfluidics and Nanofluidics*, 14(3-4):565–574, 2013.
- [138] P. R. Unwin and A. J. Bard. Scanning electrochemical microscopy. 9. Theory and application of the feedback mode to the measurement of following chemical reaction rates in electrode processes. *The Journal of Physical Chemistry*, 95(20):7814–7824, 1991.
- [139] S. A. M. van Stroe-Biezen, F. M. Everaerts, L. J. J. Janssen, and R. A. Tacke. Diffusion coefficients of oxygen, hydrogen peroxide and glucose in a hydrogel. *Analytica Chimica Acta*, 273(1-2):553–560, 1993.
- [140] R. Verfürth. A posteriori error estimation and adaptive mesh-refinement techniques. *Journal of Computational and Applied Mathematics*, 50(1-3):67–83, 1994.
- [141] B. A. Westrin and A. Axelsson. Diffusion in gels containing immobilized cells: a critical review. *Biotechnology and Bioengineering*, 38(5):439–446, 1991.
- [142] R. B. Whitner and O. Balci. Guidelines for selecting and using simulation model verification techniques. In *Proceedings of the 21st conference on Winter simulation*, pages 559–568, 1989.
- [143] T. Wilhelm and G. Wittstock. Analysis of interaction in patterned multienzyme layers by using scanning electrochemical microscopy. *Angewandte Chemie International Edition*, 42(20):2248–2250, 2003.

- [144] G. Wittstock, M. Burchardt, S. E. Pust, Y. Shen, and C. Zhao. Scanning electrochemical microscopy for direct imaging of reaction rates. *Angewandte Chemie International Edition*, 46(10):1584–1617, 2007.
- [145] C. S. Wright. Structural comparison of the two distinct sugar binding sites in wheat germ agglutinin isolectin II. *Journal of Molecular Biology*, 178(1):91–104, 1984.
- [146] T. Yasukawa, Y. Hirano, N. Motochi, H. Shiku, and T. Matsue. Enzyme immunosensing of pepsinogens 1 and 2 by scanning electrochemical microscopy. *Biosensors and Bioelectronics*, 22(12):3099–3104, 2007.
- [147] H. Ye, H. S. Park, and A. J. Bard. Screening of electrocatalysts for photoelectrochemical water oxidation on W-doped BiVO₄ photocatalysts by scanning electrochemical microscopy. *The Journal of Physical Chemistry C*, 115(25):12464–12470, 2011.
- [148] T. Yoetz-Kopelman, R. Pandey, A. Freeman, and Y. Shacham-Diamand. Modeling of suspended vs. immobilized whole-cell amperometric biosensors. *Sensors and Actuators B: Chemical*, 238:1248–1257, 2017.
- [149] C. Zhao and G. Wittstock. Scanning electrochemical microscopy for detection of biosensor and biochip surfaces with immobilized pyrroloquinoline quinone (PQQ)-dependent glucose dehydrogenase as enzyme label. *Biosensors and Bioelectronics*, 20(7):1277–1284, 2005.
- [150] C. G. Zoski and M. V. Mirkin. Steady-state limiting currents at finite conical microelectrodes. *Analytical Chemistry*, 74(9):1986–1992, 2002.
- [151] C. G. Zoski, B. Liu, and A. J. Bard. Scanning electrochemical microscopy: Theory and characterization of electrodes of finite conical geometry. *Analytical Chemistry*, 76(13):3646–3654, 2004. doi: 10.1021/ac049938r.

Santrauka (Summary in Lithuanian)

Tyrimų sritis

Pasitelkus kompiuterinį modeliavimą disertacijoje tiriamos sudėtingos cheminės ir biofizikinės sistemos, kurios yra aprašomos dalinių išvestinių lygtimis (DIL) su netiesinėmis kraštinėmis sąlygomis ir DIL sudėtingos geometrijos (netačiakampėse) srityse. Šios DIL sprendžiamos baigtinių skirtumų metodu ir kitais skaitiniais algoritmais.

DIL sprendimo su netiesinėmis kraštinėmis sąlygomis problemos kyla dėl cheminių ir biologinių procesų matematinio modeliavimo. Tyrimai netačiakampėse srityse yra aktualūs dėl poreikio įvertinti matavimo prietaisų paklaidas, atsirandančias dėl geometrijos nukrypimo nuo standarto. DIL netiesinės sistemos yra pritaikytos tyrinėti chemoterapinių vaistų patekimą į audinius.

Tikslas

Tyrimo buvo suformuluoti du pagrindiniai tikslai:

1. Sukurti skenuojančio elektrocheminio mikroskopo (SECM) matematinius modelius ir reikalingas kompiuterines programas reakcijos-difuzijos procesams ir SECM elektrodo geometrinėms savybėms modeliuoti.
2. Sudaryti kompiuterinį modelį fluorescencinių dažų prasiskverbimui į sferoido formos ląstelių struktūrą.

Tikslams pasiekti buvo iškeltos šios užduotys:

- Sukurti matematinius ir skaitinius modelius (i) SECM, veikiančio oksidacijos-redukcijos konkurencijos režimu, (ii) SECM su įvairiais nestandartiniais ultramikroelektrodais (UME) ir (iii) dažų prasiškerbimui į ląstelių sferoidus.
- Parašyti kompiuterines programas, atliekančias skaičiavimus dideliu tikslumu.
- Pasiiekti modelio ir eksperimentinių duomenų suderinamumą apskaičiuojant nežinomus modelių parametrus.
- Apskaičiuoti reakcijos kinetines konstantas ir deguonies difuzijos koeficientus SECM eksperimentams.
- Sukurti algoritmus, kuriais įvertinamas elektros srovės skirtumas (paklaidos), matuojant standartiniu elektrodu ir neidealios formos elektrodais.
- Ištirti fluorescencinių dažų, išiskverbiančių į ląstelių sferoidus, savybes priklausomai nuo ląstelių koncentracijos, prisijungimo taškų kiekio ir kt.

Metodai

SECM oksidacijos-redukcijos konkurencijos (RC-SECM) režimu modeliuojamas nestacionarių reakcijos-difuzijos lygčių sistema su netiesinėmis 3-iojo tipo kraštinėmis sąlygomis. SECM geometrija modeliuojama difuzijos lygtimis netačiakampėse geometrijose. Ląstelių sferoidai modeliuojami nestacionariomis reakcijos-difuzijos lygtimis, kuriose yra netiesiniai nariai, atsakingi už reakcijas tarp ląstelių ir fluorescencinių dažų. Šiems procesams buvo atlikti skaitiniai eksperimentai. Autorius sukūrė kompiuterinius modelius MATLAB ir Python programavimo kalbomis. Skaičiavimai buvo atlikti naudojant Vilniaus universiteto Matematikos ir informatikos fakulteto superkompiuterį.

Naujumas

- Disertacijoje pasiūlytas naujas matematinis modelis SECM, veikiančio oksidacijos-redukcijos konkurencijos režimu. Pagrindinis

šio modelio naujumas yra SECM modelių, aprašančių difuziją, sujungimas su reakcijų lygtimis naudojant netiesinę 3-iojo tipo kraštinę sąlygą.

- Nestandartinės geometrijos elektrodų tyrimas leidžia įvertinti matavimų paklaidas tarp eksperimentų, atliktų su neidealios formos elektrodu ir standartiniu tobulu elektrodu. SECM įrangos tyrimai yra populiarėjanti sritis, bet šiame darbe pirmą kartą buvo išsamiai išnagrinėtas dažniausių geometrijos nukrypimų poveikis matavimams.
- Pasiūlytas efektyvus netolygaus diskretaus tinklo sudarymo metodas, skirtas SECM modeliams stačiakampėse ir netačiakampėse elektrodo geometrijose.
- Pirmą kartą šiame tyrime modeliuotas fluorescencinių dažų prasišverbimas ir kaupimasis ląstelių sferoiduose. Pagrindinis naujumas yra nežinomų parametrų dažų molekulėms apskaičiavimas ir sėkmingas modelių validavimas fiziniu eksperimentu.

Ginami teiginiai

- Pasiūlyti kompiuteriniai modeliai yra tinkamos priemonės simuliuoti analizuotas sistemas, t. y. RC-SECM režimą, SECM su skirtingomis elektrodo geometrijomis ir fluorescencinių dažų skverbimais.
- Kiekvieno modelio korektiškumas patvirtinas (i) parodant gerą atitikimą tarp modeliavimo ir fizinio eksperimento duomenų ir (ii) patikrinant skaitinių algoritmų įgyvendinimą tam skirtais verifikavimo metodais.
- Realizuoti skaitiniai algoritmai yra tikslūs (antros eilės), besąlygiškai stabilūs ir leidžia DIL uždavinį suvesti į tiesinių lygčių sistemas, kurios efektyviai sprendžiamos perkelties metodu.
- RC-SECM režime deguonies difuzijos koeficientas yra atvirkščiai proporcingas ištirpusių medžiagų, tokių kaip gliukozė, koncentracijoms.
- Didžiausios matavimų paklaidos lyginant su standartiniu elektrodu padaromos su išlindusiu elektrodu. Įtrauktam ir kūginiam elektrodui šis skirtumas mažesnis. Be to, šios paklaidos mažėja, kai didėja santykis tarp izoliatoriaus ir elektrodo spindulių.

Disertacijos struktūra

Disertaciją sudaro šios dalys: įvadas, keturi skyriai, išvados ir literatūros sąrašas.

S.1 skyriuje analizuojamas SECM modelis, aprašytas 8 netiesinių reakcijos-difuzijos lygčių sistema. Ji sprendžiama neišreikštiniu baigtiųjų skirtumų metodu. Skaitinis sprendinys lyginamas su fizinio eksperimento rezultatais ir, priderinus modeliavimo duomenis su eksperimento rezultatais, apskaičiuojami reakcijos koeficientai ir difuzijos parametrai.

S.2 skyriuje pristatyti 4 SECM modeliai: 1 standartinės geometrijos (iš **S.1** skyriaus) ir 3 nestandartinės. DIL, aprašančios UME šiose geometrijose, yra išsprendžiamos skaitiškai ir skaitinio eksperimento rezultatai įtrauktam elektrodui palyginami su fiziniu eksperimentu parodant gerą atitikimą. Tada apskaičiuojamas paklaidos tarp rodmenų standartinėje ir nestandartinėse geometrijose bei tirama kitų SECM geometrijos parametrų įtaka matuojamai elektros srovei.

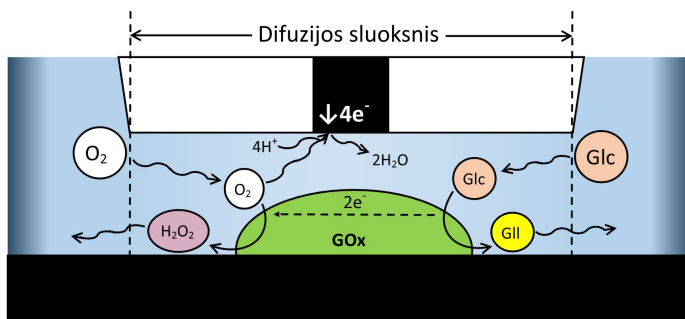
S.3 skyriuje fluorescencinių dažų įsisavinimas 3D ląstelių kultūrose modeliuojamas reakcijos-difuzijos lygtimis, kurios sprendžiamos skaitiniais metodais. Pateikiami modeliai yra skirti išanalizuoti dviejų tipų dažus ir geometrines ląstelių sferoidų savybes. Skaitinio tyrimo rezultatai palyginami su biologiniu eksperimentu. Difuzijos koeficientas tarpląstelinėje terpėje ir sferoidų prisotinimo dažais laikas apskaičiuojami naudojant pateiktus modelius.

Siekiant pagrįsti algoritmų įgyvendinimo korektiškumą, įvairūs modelio verifikavimo būdai buvo išanalizuoti ir pritaikyti ketvirtame disertacijos skyriuje.

S.1 SECM modeliavimas oksidacijos-redukcijos konkurencijos režime naudojant reakcijos-difuzijos lygtis

S.1.1 Fizinis modelis

Skenuojanti elektrocheminė mikroskopija (SECM) yra pažangus elektrocheminis metodas, pagrįstas matavimais naudojant ultramikroelektrodą (UME). Naudojantis šiuo prietaisu UME, kurio laidžioji dalis yra kelių

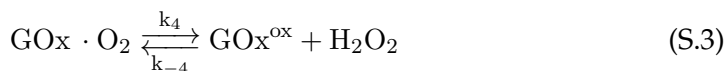
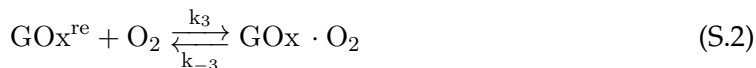
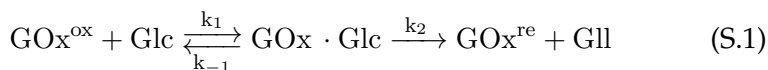


S.1 pav.: SECM matavimo schema oksidacijos-redukcijos konkurencijos režime.

dešimtųjų mikrometrų intervale, o izoliatoriaus dalis yra kelių šimtų mikrometrų diapazone, nuskaito 3D erdvę arti katalitinių ar elektrochemiškai aktyvių paviršių [12].

Šiame skyriuje nagrinėjamas oksidacijos-redukcijos konkurencijos režimas (RC-SECM), kuris naudojamas tyrimuose fermentinei kinetikai įvertinti bei vizualizuoti [68, 82]. Pagal šį režimą ištirpęs deguonis sunaudojamas dviem konkuruojančiais būdais (S.1 pav.): vienas yra pagrįstas UME vykstančia elektrochemine reakcija, o kitas – reakcija ant nelaidaus paviršiaus, katalizuojama imobilizuoto fermento, pvz., gliukozės oksidazės (GOx), kuri naudoja O₂ kaip elektronų akceptorį. Šiuo režimu tiek (i) GOx, imobilizuoti ant nelaidžio paviršiaus, tiek (ii) UME, veikiantys esant neigiamam potencialui, konkuruoja dėl ištirpusio deguonies ([99]).

Kai vandenyje yra ištirpusio deguonies O₂, gliukozę Glc yra katalizuojama GOx. Šio proceso metu sunaudojamas O₂ ir Glc, o gaminami vandenilio peroksidas H₂O₂ ir gliukonolaktonas Gll pagal lygtis:



UME srovės vertė priklauso nuo ištirpusio deguonies koncentracijos ir visų kitų elektrochemiškai aktyvių medžiagų buvimo šalia UME paviršiaus bei nuo elektrinio potencialo, veikiančio UME. Naudojamoje

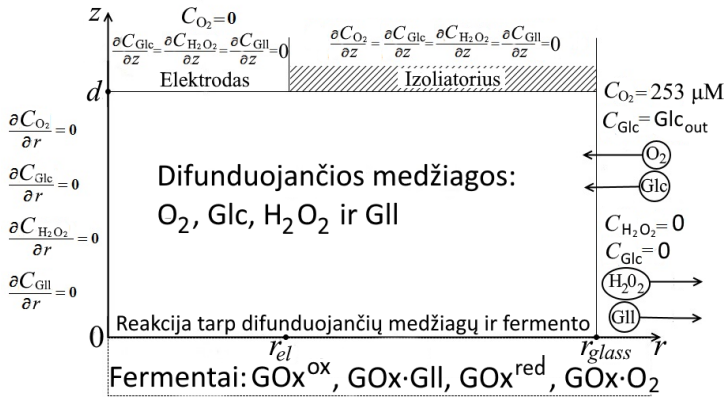
RC-SECM sistemoje (S.1 pav.) deguonis sunaudojamas dviem būdais: (i) vykdant redukcijos reakciją UME paviršiuje



ir (ii) fermentinių reakcijų metu, kai deguonis veikia kaip elektronų akceptorius, kuris prisijungia elektronus iš GOx pagal (S.1), ir perduoda juos deguoniui pagal reakcijas (S.2)–(S.3). Reakcijų greičių konstantos k buvo paimtos iš tyrimų [27, 89] ir koreguotos pagal cheminio eksperimento duomenis.

S.1.2 Matematinis modelis

Dėl simetrijos aplink centrinę elektrodo ašį modelis užrašomas cilindrinėse koordinatėse. Cilindro formos srityje atliekami SECM matavimai (S.1 pav.) yra pakeisti į 2D sritį S.2 pav.



S.2 pav.: Modeliavimo srities schema. Pavaizduotos 8 modeliuotos medžiagos - 4 difunduojantys reagentai bei 4 fermento GOx formos, kraštinės sąlygos 4-ioms difunduojančioms medžiagoms ir išorinis srautas.

Difuzijos procesai išreiškiami antruoju Fiko dėsniumi [87]:

$$\begin{aligned} \frac{\partial C_{\text{O}_2}}{\partial t} &= D_{\text{O}_2} \Delta C_{\text{O}_2}, \\ \frac{\partial C_{\text{Glc}}}{\partial t} &= D_{\text{Glc}} \Delta C_{\text{Glc}}, \\ \frac{\partial C_{\text{H}_2\text{O}_2}}{\partial t} &= D_{\text{H}_2\text{O}_2} \Delta C_{\text{H}_2\text{O}_2}, \\ \frac{\partial C_{\text{Gll}}}{\partial t} &= D_{\text{Gll}} \Delta C_{\text{Gll}}, \quad 0 < t \leq T, \quad 0 < z < d, \quad 0 < r < r_{\text{glass}}. \end{aligned} \quad (\text{S.5})$$

Šiose lygtyse:

C_{O_2} , C_{Glc} , $C_{H_2O_2}$ ir C_{Glu} yra atitinkamų difunduojančių reagentų koncentracijos, kurios išreiškiamos kaip laiko t , erdviųjų koordinačių z ir r funkcijos.

D_{O_2} , D_{Glc} , $D_{H_2O_2}$ ir D_{Glu} yra difuzijos koeficientai.

d yra atstumas tarp fermentu modifikuoto paviršiaus ir elektrodo. Skaitinio eksperimento metu d keičiamas nuo 1 μm iki 120 μm . Tai atitinka elektrodo stumdymą aukštyn ir žemyn cheminio eksperimento metu.

$r_{glass} = 80 \mu\text{m}$ yra izoliuotos srities spindulys.

T yra skaičiavimo eksperimento trukmė, matuojama sekundėmis.

Laplaso operatorius Δ cilindrinėse koordinatėse su centrine simetrija yra

$$\Delta C = \frac{1}{r} \frac{\partial C}{\partial r} \left(r \frac{\partial C}{\partial r} \right) + \frac{\partial^2 C}{\partial z^2}.$$

Cheminės reakcijos (S.1)–(S.3) paviršiuje $z = 0$ yra išreiškiamos reakcijų lygtimis fermentams:

$$\begin{aligned} \frac{\partial C_{GOx^{ox}}}{\partial t} &= -k_1 C_{GOx^{ox}} C_{Glc} + k_{-1} C_{GOx \cdot Glc} + k_4 C_{GOx \cdot O_2} - \\ &\quad - k_{-4} C_{GOx^{ox}} C_{H_2O_2}, \\ \frac{\partial C_{GOx \cdot Glc}}{\partial t} &= k_1 C_{GOx^{ox}} C_{Glc} - (k_{-1} + k_2) C_{GOx \cdot Glc}, \\ \frac{\partial C_{GOx^{re}}}{\partial t} &= k_2 C_{GOx \cdot Glc} - k_3 C_{GOx^{re}} C_{O_2} + k_{-3} C_{GOx \cdot O_2}, \\ \frac{\partial C_{GOx \cdot O_2}}{\partial t} &= k_3 C_{GOx^{re}} C_{O_2} - k_{-3} C_{GOx \cdot O_2} - k_4 C_{GOx \cdot O_2} + \\ &\quad + k_{-4} C_{GOx^{ox}} C_{H_2O_2}, \end{aligned} \tag{S.6}$$

$$0 < t \leq T, \quad 0 \leq r < r_{glass},$$

kur $C_{GOx^{ox}}$, $C_{GOx \cdot Glc}$, $C_{GOx^{re}}$ ir $C_{GOx \cdot O_2}$ yra paviršiuje imobilizuotų fermentų koncentracijos, priklausančios nuo laiko t ir spindulio r .

Difunduojančioms medžiagoms reakcijos greičio dėsniai ant pagrindo $z = 0$ yra išvedami iš cheminių lygčių (S.1)–(S.3) taip pat kaip (S.6).

Jie yra naudojami kaip 3-ojo tipo kraštinės sąlygos kraštui $z = 0$:

$$\begin{aligned}
 D_{O_2} \frac{\partial C_{O_2}}{\partial z} &= k_3 C_{GOx}^{r_{el}} C_{O_2} - k_{-3} C_{GOx} \cdot O_2, \\
 D_{Glc} \frac{\partial C_{Glc}}{\partial z} &= k_1 C_{GOx}^{ox} C_{Glc} - k_{-1} C_{GOx} \cdot Glc, \\
 D_{H_2O_2} \frac{\partial C_{H_2O_2}}{\partial z} &= -k_4 C_{GOx} \cdot O_2 + k_{-4} C_{GOx}^{ox} C_{H_2O_2}, \\
 D_{Gll} \frac{\partial C_{Gll}}{\partial z} &= k_2 C_{GOx} \cdot Glc, \quad 0 < t \leq T, \quad z = 0, \quad 0 \leq r < r_{glass}.
 \end{aligned} \tag{S.7}$$

Fermentinės reakcijos pradžioje deguonies koncentracija difuzijos sluoksnyje yra $253 \mu\text{M}$ ($M = \text{mol/L}$), aktyviosios gliukozės oksidazės GOx paviršiaus koncentracija yra $2,114 \cdot 10^{-8} \text{ mol/m}^2$. Laikoma, kad visų kitų reagentų pradžioje nėra, todėl $C_{GOx} \cdot Glc = C_{GOx}^{r_{el}} = C_{GOx} \cdot O_2 = 0$, $t = 0$, $0 < r < r_{glass}$:

Likusios kraštinės sąlygos sistemai (S.5) yra nurodytos S.2 pav.

S.1.3 Skaitinis sprendimas ir SECM atsakas

Turi būti išspręsta 8 diferencialinių lygčių sistema (S.5)–(S.6) su pradinėmis-kraštinėmis sąlygomis. 4 difuzijos lygtims (S.5) buvo naudojamas kintamos krypties neišreikštinis baigtinių skirtumų metodas (ADIFDM), kuris yra klasikinis difuzijos lygčių 2D erdvėje sprendimo metodas. Šio metodo efektyvumą demonstravo įvairios tyrimų grupės [19, 120]. Nedifunduojančių reagentų paprastųjų diferencialinių lygčių sistema (S.6) buvo išspręsta simetriniu Eulerio metodu.

Pagrindinis parametras, žinomas kaip ultramikroelektrodo atsakas, yra elektros srovė, kuri matuojama elektrodu ties $z = 0$, $0 < r < r_{el}$ ir susidaro iš O_2 srauto, t. y. lemiamą C_{O_2} gradiento dydžio. Su SECM pamatuotos srovės grafikas dar vadinamas artėjimo kreive, nes fiziniai eksperimentai yra atliekami artinant UME arčiau fermentu modifikuoto paviršiaus, t. y. artėjama prie paviršiaus ir kiekvieną kartą sustojus registruojamas elektrinis signalas. Srovė per elektrodą apskaičiuojama kaip laiko funkcija [11]:

$$i(t) = 2\pi n F D_{O_2} \int_0^{r_{el}} \left. \frac{\partial C_{O_2}}{\partial z} \right|_{z=d} r dr, \tag{S.8}$$

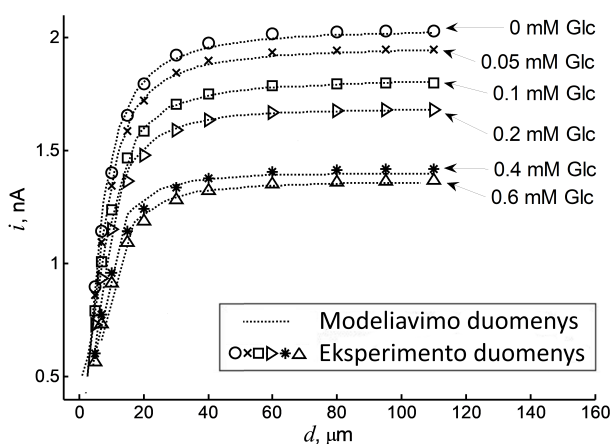
kur $n = 4$ yra pasikeistų elektronų skaičius ir F – Faradėjaus konstanta. Integralas (S.8) buvo apytiksliai apskaičiuotas pagal antrosios eilės Niutono-Koteso kvadratūros formules.

S.1.4 Modeliavimo ir eksperimento rezultatai

Kompiuterinio modeliavimo rezultatai buvo palyginti su realiais RC-SECM eksperimentais (S.3 pav.), kurie buvo atlikti su 6 fiksuotomis gliukozės koncentracijos vertėmis: tarp 0 mM (be fermentinės reakcijos) ir 0,6 mM. Kaip ir tikėtasi, artėjimo kreivės su didesne Glc koncentracija buvo žemiau nei mažesnės koncentracijos kreivės. Ši savybė yra RC-SECM režimo esmė, nes O_2 vartojimas ant elektrodo yra sulėtėjęs dėl konkurencijos su O_2 vartojimu fermentinės reakcijos metu, kuri yra greitesnė esant didesnei Glc koncentracijai. Be to, artėjimo kreivių pozicijoms taip pat turėjo įtakos O_2 difuzijos koeficiento D_{O_2} skaičiavimas pagal formulę:

$$D_{O_2} = 4,7 \cdot 10^{-10} + \frac{2,7 \cdot 10^{-10}}{Glc_{out} + 0,4}, \quad (S.9)$$

kur Glc_{out} – Glc koncentracija išoriniame tirpale. (S.9) buvo išvesta priderinus skaitinio eksperimento duomenis prie cheminio eksperimento ir koeficientus suskaičiavus mažiausių kvadratų metodu. Kadangi D_{O_2} mažėja esant didesniai Glc kiekiui, pastoviosios būsenos srovė, apskaičiuota tiek modeliuojant, tiek eksperimentu, taip pat buvo mažesnė.



S.3 pav.: Srovės ir atstumo d priklausomybė modelio bei eksperimento duomenims, kai skirtingos gliukozės koncentracijos įpiltos į buferinį tirpalą.

Ties mažesniais atstumais d , kur stebimas staigus elektrinio signalo pakilimas, modelio ir eksperimentinių duomenų atitikimas buvo šiek tiek prastesnis. Tai galima paaiškinti matavimo paklaidomis, priklausomybe nuo eksperimento rezultatų kalibravimo ir modelio prielaidų neatitikimu mažiausiais atstumais ($d \lesssim 1 \mu\text{m}$) dėl naujų fizinių veiksnių. Galima laikyti, kad kompiuterinių ir cheminių eksperimentų rezultatai labai gerai sutapo.

S.1.5 Išvados

Šiame skyriuje pirmą kartą literatūroje pateiktas SECM, veikiančio oksidacijos-redukcijos konkurencijos režimu, modelis, kuris buvo užrašytas 8 reakcijos-difuzijos lygčių sistema. Naudojant šį modelį buvo apskaičiuotas deguonies sunaudojimo greitis fermentinėje reakcijoje, įvertinta fermentinių reakcijų kinetika ir nustatytas deguonies difuzijos koeficientas skirtingos sudėties terpėse. Apskaičiavus šiuos parametrus buvo pasiektas geras atitikimas su cheminio eksperimento duomenimis.

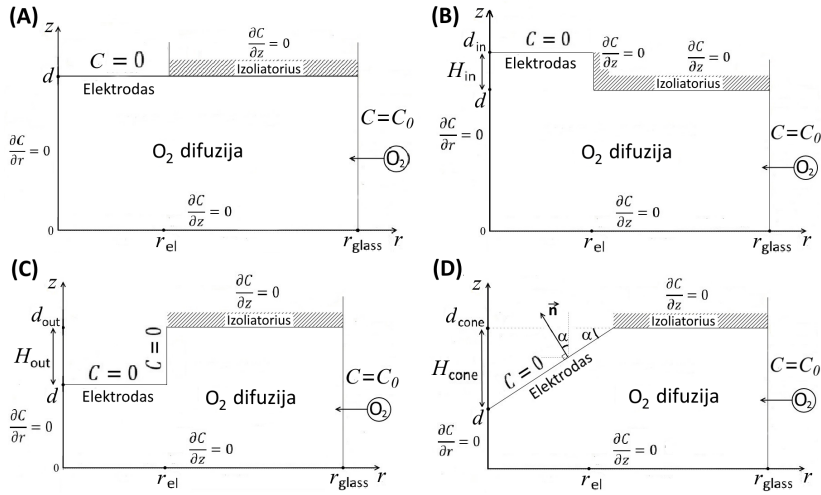
S.2 Elektrodo geometrijos įtakos su SECM matuojamai srovei matematinis modeliavimas

S.2.1 Įžanga

SECM yra galingas įrankis lokalizuotiems elektrochemiškai aktyvių paviršių tyrimams nuskaitant juos ultramikroelektrodu [74]. Siekiant tikslių matavimo rezultatų, UME turėtų būti kruopščiai paruoštas ir prieš matuojant nustatyta elektrodo geometrija – RG faktorius (santykis tarp elektrodo ir izoliatoriaus spindulio), elektrodo paviršiaus savybės. UME gamyba vis dar yra labai sudėtinga ir atliekama rankiniu būdu, todėl gamyboje sunku išvengti UME geometrijos pokyčių nuo idealiai lygios formos. Be to, UME geometrija keičiasi kiekvieną kartą, kai UME yra šlifuojamas ar netyčia pažeidžiamas eksperimento metu palietus tiriamąjį paviršių. Šie UME geometrijos pokyčiai sukelia didelius UME srovės svyravimus. Paprastas ir laiką taupantis būdas UME geometrijai nustatyti būtų eksperimentu gautų srovės kreivių palyginimas su kreivėmis, gautomis pagal konkretų matematinį modelį. Siekiant įvertinti UME geometrijos įtaką eksperimento rezultatams, atlikti skaitmeniniai modeliavimai [13, 39, 120, 123], bet vis dar reikalingas bendras metodas padedantis nustatyti UME geometriją.

Šiame skyriuje aprašyti matematiniai modeliai, skirti ištirti keletą UME geometrijų: standartinį UME, įtrauktą UME su laidžia dalimi, įtraukta į izoliatoriaus vidų, išlindusį UME su laidžia dalimi, išlindusia iš izoliatoriaus, ir kūginį UME kūgio formos laidžia dalimi, išlindusia iš izoliatoriaus. Šis tyrimas yra skirtas biologinių sistemų be oksidacijos-redukcijos mediatorių tyrimui, o pateikto metodo pranašumas yra tas, kad galima atpažinti UME geometriją, registruojant deguonį buferiniame tirpale neigiamo grįžtamojo ryšio režimu SECM.

S.2.2 Elektrodo geometrijos ir jų matematiniai modeliai



S.4 pav.: Modeliavimo sričių schemas su kraštinėmis sąlygomis, svarbiais UME geometrijos parametrais ir kt. (A) Standartinis UME, (B) įtrauktas UME, kurio įtraukimo gylis H_{in} , (C) išlindęs UME su išsikišimo aukščiu H_{out} , (D) kūginis UME su pagrindo kampu α .

Standartinio elektrodo matematinis modelis

Stačiakampė sritis S.4A pav. naudojama standartinio UME geometrijai pavaizduoti. Deguonies difuzija užrašoma:

$$\frac{\partial C}{\partial t} = D_{O_2} \left(\frac{\partial^2 C}{\partial r^2} + \frac{1}{r} \frac{\partial C}{\partial r} + \frac{\partial^2 C}{\partial z^2} \right),$$

$$0 < t \leq T, \quad 0 < z < d, \quad 0 < r < r_{glass}, \quad (S.10)$$

kur C yra O_2 koncentracija, išreikšta kaip laiko t ir 2 erdvinių koordinačių r ir z funkcija. T yra skaičiavimo eksperimento trukmė, d – atstumas nuo paviršiaus iki aktyvios elektrodo dalies, $r_{el} = 5 \mu m$ yra laidžiosios dalies spindulys ir $r_{glass} = 80 \mu m$ – UME izoliuotos dalies spindulys. Deguonies difuzijos koeficientas vandenyje D_{O_2} yra $1,105 \cdot 10^{-9} m^2/s$ [74].

Pradinė sąlyga yra $C = 253 \mu M$ už $t = 0$, $0 < z < d$, $0 < r < r_{glass}$. Visos reikalingos kraštinės sąlygos parodytos S.4A pav.

UME srovės stipris apskaičiuojamas pagal (S.8).

Elektrodo su įtraukta laidžia dalimi matematinis modelis

Analizavome situaciją, kai aktyvioji (laidžioji) UME dalis yra įtraukta gyliu H_{in} į izoliatoriaus dalį. Atstumas nuo paviršiaus iki įtraukto UME izoliacinės dalies vis dar yra d , tačiau atstumas tarp paviršiaus $z = 0$ (eksperimente tai – aktyvus paviršius) ir UME laidžios dalies yra $d_{in} = d + H_{in}$. Šis atstumas visada yra didesnis nei d , taigi šioje geometrijoje laidžioji UME dalis yra toliau nuo paviršiaus lyginant su idealios formos plokštumą turinčiu UME. Modeliavimo sritis S.4B pav. susideda iš 2 sujungtų stačiakampių: didesnio aukštis d yra toks pat kaip standartiniame UME S.4A pav., o aukščio H_{in} mažesnis atitinka įtrauktą dalį.

Difuzijos lygtis (S.10), pradinė sąlyga ir didžioji dalis kraštinių sąlygų išlieka tos pačios, tačiau pateikiamos naujoje srityje, kaip parodyta S.4B pav. Pasikeičia šios sąlygos: kraštinė sąlyga ant elektrodo yra $C = 0$, $t > 0$, $z = d_{in}$, $0 < r \leq r_{el}$, o įtrauktoje dalyje prie izoliatoriaus yra nauja deguonies srauto blokavimo sąlyga $\frac{\partial C}{\partial r} = 0$, $t > 0$, $d < z < d_{in}$, $r = r_{el}$.

Norint apskaičiuoti srovę, naudojama lygtis, panaši į (S.8):

$$i(t) = 2\pi n F D_{O_2} \int_0^{r_{el}} \left. \frac{\partial C}{\partial z} \right|_{z=d_{in}} r dr. \quad (S.11)$$

Elektrodo su išlindusia laidžia dalimi matematinis modelis

Išlindęs UME modeliuojamas kaip laidaus paviršiaus cilindras, išlindęs iš UME izoliacinės dalies į difuzijos sritį. Yra 2 UME laidžiosios cilindro dalys: disko formos elektrodo galas kaip standartiniame UME ir cilindro

šonas (S.4C pav.). Tai reiškia, kad aktyviosios UME dalies paviršiaus plotas yra didesnis nei standartinio UME ir ši sritis priklauso nuo išsi-kišimo aukščio H_{out} . Atstumas tarp tyrimų paviršiaus ($z = 0$) ir UME laidžiojo paviršiaus išlieka d , tačiau atstumas nuo tyrimų paviršiaus iki izoliuotosios išorinės UME dalies padidėja iki $d_{out} = d + H_{out}$. Taigi, net kai d priartėja prie 0, deguonies difuzija į išlindusį UME nėra užblo-kuota, nes pro UME cilindro šonus patenka deguonis. Tai yra esminis skirtumas nuo ankstesnių modelių.

Difuzijos lygtis (S.10) ir pradinės-kraštinės sąlygos išlieka tokios pačios kaip standartiniam UME, išskyrus naują kraštinę sąlygą cilindro šone $C = 0, \quad t > 0, \quad d \leq z \leq d_{out}, \quad r = r_{el}$ ir sąlygą izoliatoriui, kuris šiuo atveju yra d_{out} atstumu nuo paviršiaus: $\frac{\partial C}{\partial z} = 0, \quad t > 0, \quad z = d_{out}, \quad r_{el} < r < r_{glass}$.

Srovė per elektrodo aktyvią dalį skaičiuojama kaip dviejų integralų suma:

$$i(t) = 2\pi n F D_{O_2} \int_0^{r_{el}} \left. \frac{\partial C}{\partial z} \right|_{z=d} r dr + 2\pi n F D_{O_2} r_{el} \int_d^{d_{out}} \left. \frac{\partial C}{\partial r} \right|_{r=r_{el}} dz. \quad (S.12)$$

Elektrodo su kūgine laidžia dalimi matematinis modelis

Valant elektrodus, o tai dažniausiai daroma švitriniumi popieriumi, gali at-sirasti smulkių, bet aštrių pažeidimų laidžiojoje dalyje. Nagrinėjamame kūginiame UME šie nelygumai modeliuojami vienu suvidurkintu išlin-dusiu kūgiu. Tikimasi, kad iš modelio su šia viena išlindusia dalimi galima geriau suprasti veikimą elektrodo su nelygiais aktyviais pavi-ršiais.

Lygties (S.10) sprendimo sritis yra stačiakampis su vienu iškirptu kampu, reiškiančiu kūginę laidžiąją dalį. Kūgio kraštas sudaro kampą α su kūgio pagrindu. Atstumas tarp tyrimų paviršiaus ir kūgio viršūnės yra d , o atstumas nuo šio paviršiaus iki izoliatoriaus yra $d_{cone} = d + H_{cone}$, kur kūgio aukštis $H_{cone} = r_{el} / \tan(\alpha)$. Akivaizdu, kad laidžiosios dalies plotas yra didesnis nei standartinio UME, o tyrimų paviršius nepasiekia izoliatoriaus net su $d = 0$ panašiai kaip išlindusio UME atveju. Pradinės-kraštinės sąlygos yra įprastos, išskyrus sąlygą ant kūgio šono UME aktyviai daliai:

$$C = 0, \quad t > 0, \quad 0 \leq r \leq r_{el}, \quad z = r \tan \alpha + d.$$

Srovės kryptis per kūginį UME yra statmena kūgio šonui, todėl normalinė išvestinė \vec{n} , sudaranti kampą α su r ašimi (pagal S.4D pav.), naudojama apskaičiuoti srovės stipriui:

$$i(t) = \frac{2\pi n F D_{O_2}}{\cos \alpha} \int_0^{r_{el}} \frac{\partial C}{\partial \vec{n}} r dr. \quad (S.13)$$

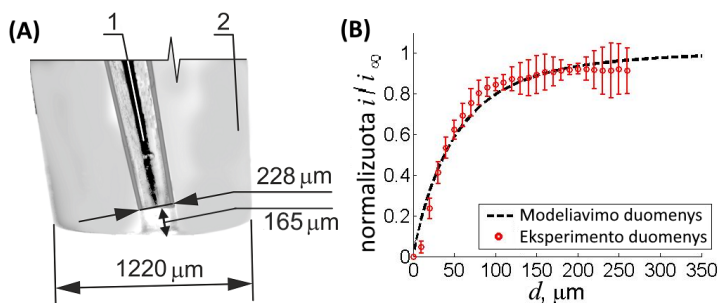
S.2.3 Skaitinis sprendimas

Lygtis (S.10) visose 4 skirtingose geometrijose su atitinkamomis pradinėmis-kraštinėmis sąlygomis buvo išspręsta skaitiniu būdu, naudojant kintamos krypties neišreikštinį baigtinių skirtumų metodą [3, 93]. Algoritmai, sprendžiantys uždavinį, buvo realizuoti naudojant Python su Numpy biblioteka. Buvo pasirinktas netolygus tinklas, sudarytas iš 200×200 taškų, ypač sutirštinant tinklo taškus, esančius šalia elektrodo, ir prie aštrių nestandartinės geometrijos kampų. Laiko parametras T buvo paimtas pakankamai didelis, kad būtų užtikrintas stabilus sprendinys. Atliekant skaitinį eksperimentą nustatyta, kad analizuotų elektrodų srovės kreivėms stabilizuotis pakanka $T = 6$ s ir tam reikia maždaug $10 \cdot 10^3 - 250 \cdot 10^3$ laiko žingsnių, priklausomai nuo UME geometrijos.

S.2.4 Modeliavimo rezultatai

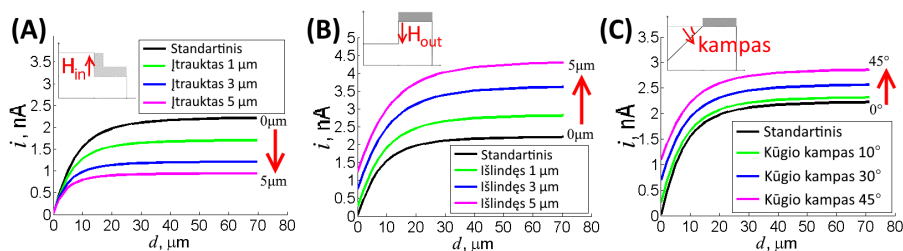
Eksperimento duomenų ir matematinio modeliavimo rezultatų palyginimas

Įtraukto UME srovės stiprio kreivė buvo apskaičiuota naudojant matematinį modelį ir palyginta su eksperimento būdu gautais duomenimis, naudojant realų įtrauktą UME, pavaizduotą S.5A pav. Duomenys rodo gerą atitikimą mažesnėms d reikšmėms, kaip parodyta S.5B pav., bet skirtumas padidėja esant didesnėms d reikšmėms. Šis poveikis gali būti susijęs su didesnėmis eksperimentinėmis paklaidomis (žr. paklaidų juostas S.5B pav.). Aukštesnės paklaidų juostos esant didesnėms d reikšmėms atsiranda dėl to, kad sudėtinga pasiekti stabilias srovės realiam įtrauktam UME, kurio įtraukimo gylis $H_{in} = 165 \mu\text{m}$ yra gana didelis palyginti su spinduliu $r_{el} = 114 \mu\text{m}$. Taigi, šie eksperimentiniai sunkumai buvo tikėtini dėl tokių reikšmingų nukrypimų nuo standartinio UME. Dėl geros atitikties su cheminio eksperimento duomenimis prasminga naudoti modelius UME geometrijos įtakos tyrimams.



S.5 pav.: A) Realus įtraukto UME vaizdas. (B) Nusistovėjusios srovės eksperimento ir modeliavimo duomenų palyginimas naudojant UME, pavaizduotą A dalyje.

UME geometrijos įtaka srovės stiprio kreivėms

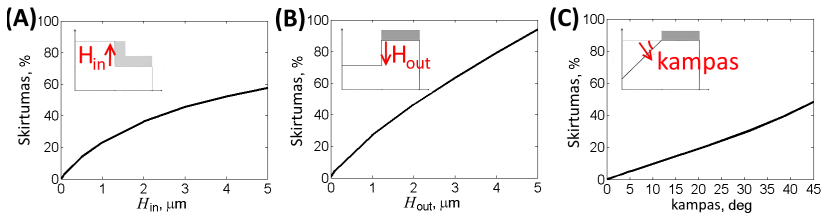


S.6 pav.: Pastovios būsenos srovės priklausomybė nuo d , atsižvelgiant į nestandartinių UME geometrines formas. Paveikslėlių kampuose rodoma, kuris parametras yra keičiamas, o raudonos rodyklės žymi pokyčio kryptį. (A) Išlindęs UME; (B) įtrauktas UME; (C) kūginis UME.

Įtraukto UME atveju absoliutinė srovė mažėja palyginti su standartinio UME srove (pav. S.6A). Tai galima paaiškinti tuo, kad deguoniui yra sunkiau pasiekti laidžiąją UME dalį nei standartiniam UME, nes izoliatoriaus posūkiu sumažina visų medžiagų, įskaitant deguonį, difuziją. Kita vertus, srovės kreivės išlindusiam elektrodui (S.6B pav.) sparčiai auga, didėjant H_{out} . Taip yra dėl deguonies difuzijos į elektrodo laidžiosios dalies dvi dalis (vietoje įprastos vienos) – šoninę ir apatinę. Taigi, UME laidus plotas yra daug didesnis nei standartinio UME. Kūginio UME atveju absoliutinė srovė didėja esant didesniai šoniniam kampui, kaip parodyta S.6C pav. Kūginio UME laidus plotas yra didesnis didesniems kampams, todėl kyla bendra srovė, tačiau tikimasi, kad padidėjimas nebus tiesinis, nes kinta ir normalinės išvestinės \vec{n}

(pavaizduota S.4D pav.) kryptis. Taigi, srovės kreivėms S.6C pav. įtakos turi tiek didėjantis aktyvusis UME plotas, tiek kintanti deguonies srauto kryptis.

Norėdami tiksliau ištirti geometrijos nukrypimo nuo standarto įtaką, suskaičiavome skirtumus (paklaidas) tarp nestandartinių UME ir standartinio UME srovės imdami maksimalią skirtumo reikšmę tarp srovės grafikų. Pagal S.7 pav., darome išvadą, kad didžiausias skirtumas yra išlindusiam UME ir siekia beveik 100 % su 5 μm išlindimu ir 5 μm spindulio elektrodu. Maksimalus įtraukto UME skirtumas yra 60 % su įtraukimo gyliu $H_{in} = 5 \mu\text{m}$, o kūginio UME atveju – 50 % su kūgio kampų 45°, kuris atitinka to paties kūgio išsikišimo aukštį $H_{cone} = 5 \mu\text{m}$. Naudojant šiuos duomenis galima sužinoti, kiek stipriai pažeistas UME.



S.7 pav.: Srovės skirtumai tarp nestandartinių UME ir standartinio UME priklausomai nuo geometrijos nukrypimo nuo standarto.

Naudojantis S.7 pav. duomenimis apskaičiuojama, su koku nestandartinio UME įtraukimo gyliu / išsikišimo aukščiu gaunama tam tikra paklaida nuo standartinio UME. Ši informacija yra naudinga norint nustatyti UME tinkamumą SECM atliekamais eksperimentams – tikrinama, kada matavimo paklaida tampa didesnė nei norėta. Tuo tikslu buvo apskaičiuoti UME geometrijų parametrai, su kuriais gaunamos 5 %, 10 %, 25 % ir 50 % paklaidos nuo standarto naudojant kubinį aproksimavimą S.7 pav. duomenims ir pateikti S.1 lentelėje. Buvo parinkti bedimensiniai parametrai, atspindintys santykį su UME spinduliu r_{el} , kad duomenis būtų galima naudoti įvairaus dydžio UME aktyviajai daliai. Tai yra standartinė procedūra SECM modeliuojant [93]. Iš S.1 lentelės matosi, kad išlindusio UME išsikišimo aukštis yra parametras, su kuriuo greičiausiai pasiekiami pasirinkti skirtumai nuo standartinio UME, o tai rodo, kad SECM su išlindusiu UME yra jautriausias matavimo paklaidoms. Išlindusio UME atvejis yra itin aktualus, nes tokio tipo pažeidimai labai paplitę ir atsiranda poliruojant arba per greitai priartėjant prie tiriamo paviršiaus ar su juo susilietus.

S.1 lentelė: Bedimensiniai UME geometrijų parametrai, su kuriais atsiranda 5 %, 10 %, 25 % ir 50 % skirtumai nuo standartinio UME srovės stiprio kreivių.

Skirtumas nuo standartinio UME	5 %	10 %	25 %	50 %
Įtraukimo gylis H_{in}/r_{el}	0,034	0,075	0,225	0,745
Išlindimo aukštis H_{out}/r_{el}	0,027	0,064	0,186	0,438
Kūgio aukštis H_{cone}/r_{el}	0,090	0,184	0,488	1,042

S.2.5 Išvados

Matematinis modelis, apibūdinantis tris skirtingas nestandartines UME geometrijas (įtrauktos, išlindusios ir kūgio formos aktyvios dalies), buvo naudojamas įvertinant matavimų paklaidą nuo standartinio UME srovės matuojant apgadintais ar neidealios formos UME. Pastebėta, kad didžiausias skirtumas nuo standarto gaunamas išlindusiam UME ir maksimalus skirtumas siekia 100 %, kai laidžioji elektrodo dalis yra išlindusi tokiu pat dydžiu, koks yra elektrodo spindulys. Skirtumai tarp įtraukto UME ir kūginio UME yra mažesni – atitinkamai 60 % ir 50 % įtraukimui / kūgio aukščiui lygiam elektrodo spinduliui.

Išnagrinėto matematinio modelio privalumas yra tas, kad jis gali būti panaudotas defektams nustatyti paprastame tirpale palyginant modeliuotą UME reakciją su eksperimentiniais duomenimis. Šis metodas gali būti taikomas įvairiomis kryptimis. Šioje darbo dalyje buvo analizuojami buferiniai tirpalai, tačiau, norint ištirti įtaką reakcijos kinetikai, modelį galima išplėsti deguonies redukcijos reakcijomis.

S.3 Fluorescencinių dažų prasiskverbimo į ląstelių sferoidus modeliavimas

Šioje dalyje naudojant netiesinę reakcijos-difuzijos lygčių sistemą buvo modeliuojama kviečių gemalų agliutinino (WGA-Alexa488) ir rodamino (R6G) dažų difuzija, o taip pat WGA-Alexa488 prisijungimas prie ląstelių. Šių dažų difuzijai į ląstelių sferoidus (suspaustos sferos formos ląstelių darinius) apibūdinti buvo pateikti trys skirtingi modeliai – R6G modelis, užrašytas difuzijos lygtimi, žiedų modelis su kintamu difuzijos koeficientu ir WGA modelis, užrašytas reakcijos-difuzijos lygtimis.

S.3.1 Modelių taikymai fiziniuose eksperimentuose

Dažų patekimo į ląstelių sferoidus modeliavimas motyvuojamas 3D ląstelių kultūrų pritaikymu įvairiuose biomedicinos tyrimuose. Sutarinama, kad 3D kultūrų metodas yra artimesnis natūraliems audiniams nei buvęs standartas – vienasluoksnės ląstelių kultūros [46]. 3D ląstelių kultūros paprastai naudojamos kaip pirminio vaistų, skirtų vėžio gydymui, tyrimo platforma, tačiau dėl įvairių apribojimų ne visus vaistus galima iširti. Tokiu atveju būtų naudinga turėti matematinius modelius, kurie, panaudojus panašių jau iširtų molekulių duomenis, numatytų vaistų kaupimąsi ir pasiskirstymą 3D ląstelių kultūrose. Fluorescenciniai dažai, kurių fizikinės ir cheminės savybės, tokios kaip struktūra ir molekulinė masė, yra labai panašūs į chemoterapinius agentus, galėtų būti naudojami modeliuojant ir kiekybiškai įvertinant vaistų įsiskverbimą į 3D ląstelių kultūras. Viena iš dažniausiai naudojamų 3D ląstelių kultūrų yra ląstelių sferoidai, kurie yra sferoido formos savarankiškai susiformavusios ląstelių grupės [1, 66].

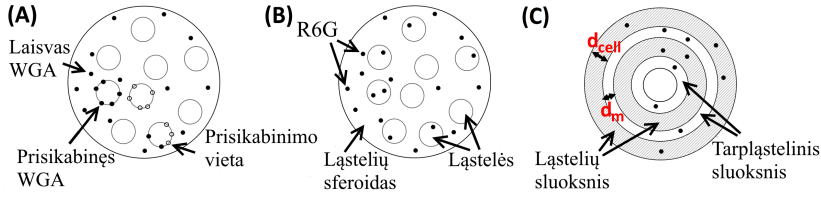
Šiame tyrime naudotas rodaminas 6G (R6G) yra fluorescenciniai lipofiliniai dažai, kurie specialiai nusidažo ir kaupiasi mitochondrijose. Dėl savo lipofilinės prigimties R6G taip pat žinomas kaip specifinė lipidų apšvietimo dėmė, leidžianti R6G naudoti kaip fluorescencinį lipidų žymeklį [32, 43]. Taip pat buvo parodyta [95], kad R6G dažai gali būti naudojami *in vitro* (t. y. stikle, mėgintuvėlyje) ląstelių studijoms, vizualizuojant kepenų kraujagyslių tinklus ir tiriant kraujo tekėjimo pasiskirstymą kepenyse įvairiomis sąlygomis.

Taip pat modeliavime naudotas kviečių gemalų agliutinas (WGA) – lektinas, apsaugantis kviečius nuo vabzdžių, mielių ir bakterijų. WGA selektyviai jungiasi su sialio rūgšties liekanomis, kurių daugiausiai randama plazminėje membranoje [145]. WGA-Alexa488, kuris yra WGA ir Alexa Fluor fluoroforų junginys, naudojamas kaip fluorescencinis žymeklis dažyti įvairių žinduolių ląstelių plazminę membraną.

S.3.2 Matematiniai modeliai

WGA judėjimas, modeliuojamas reakcijos-difuzijos lygtimis

WGA molekulės juda tarpląstelinėje terpėje difuzijos būdu, o į ląsteles patenka prisijungdamos prie specialių prisikabinimo vietų membranoje kaip parodyta S.8A pav. WGA molekulių difuzija ir prisikabinimas prie



S.8 pav.: (A) WGA modelis, (B) R6G modelis, (C) žiedų modelis.

ląstelių sferoiduose išreiškiamas lygtimi sferinėse koordinatėse:

$$\frac{\partial C_{out}}{\partial t} = D \frac{1}{r^2} \frac{\partial}{\partial r} \left(r^2 \frac{\partial C_{out}}{\partial r} \right) - k_{bind} (B_{max} - C_{bind}) C_{out},$$

$$0 < t \leq T, \quad 0 < r < R, \quad (\text{S.14})$$

kur k_{bind} yra WGA prisikabinimo prie ląstelių membranos greičio konstanta, R yra sferos spindulys, D – difuzijos koeficientas, $C_{out}(t, r)$ yra difunduojančių WGA molekulių koncentracija sferoje, T – modeliavimo trukmė. Padaryta prielaida, kad sferoidai yra homogeniški visomis kryptimis.

Ląstelių membranose yra ribotas molekulių prisikabinimo vietų skaičius, žymimas konstanta B_{max} [57]. Kai šis skaičius pasiekiamas, molekulės nebegali prisijungti prie ląstelės membranos. Prisikabinimo prie ląstelių procesas modeliuojamas pagal lygtį:

$$\frac{\partial C_{bind}}{\partial t} = k_{bind} (B_{max} - C_{bind}) C_{out}, \quad 0 < t \leq T, \quad (\text{S.15})$$

kur $C_{bind}(t, r)$ yra koncentracija WGA molekulių, prisikabinusių prie ląstelių membranos.

Naudojamos pradinės-kraštinės sąlygos:

$$\begin{aligned} C_{out} \Big|_{t=0} &= 0, & 0 \leq r \leq R, \\ C_{bind} \Big|_{t=0} &= 0, & 0 \leq r \leq R, \\ C_{out} \Big|_{r=R} &= 0,13 \mu\text{M}, & t > 0, \\ \frac{\partial C_{out}}{\partial r} \Big|_{r=0} &= 0, & t > 0. \end{aligned} \quad (\text{S.16})$$

Rodamino judėjimas, modeliuojamas difuzijos lygtimi

Rodaminas R6G difunduoja tiek per ląsteles, tiek tarpląstelinę medžiagą (S.8B pav.), todėl R6G molekulių judėjimas sferoiduose modeliuojama naudojant difuzijos lygtį:

$$\frac{\partial C}{\partial t} = D \frac{1}{r^2} \frac{\partial}{\partial r} \left(r^2 \frac{\partial C}{\partial r} \right), \quad 0 < t \leq T, \quad 0 < r < R, \quad (\text{S.17})$$

kur $C(t, r)$ yra R6G koncentracija, o lygtis yra versija (S.14) be reakcijos nario.

Pradinės-kraštinės sąlygos yra panašios kaip (S.16):

$$\begin{aligned} C|_{t=0} &= 0, \quad 0 \leq r \leq R, \\ C|_{r=R} &= 10,4 \mu\text{M}, \quad t > 0, \\ \frac{\partial C}{\partial t} \Big|_{r=0} &= 0, \quad t > 0. \end{aligned} \quad (\text{S.18})$$

Rodamino judėjimas naudojant ląstelių ir tarpląstelinės medžiagos žiedų modelį

Sferoidai buvo modeliuojami kaip koncentriniai ląstelių ir tarpląstelinės medžiagos žiedai, kaip parodyta S.8C pav., kur ląstelių žiedai žymi suvidurkintas ląsteles, o tarpląstelinis sluoksnis – medžiagą tarp ląstelių. R6G difuzijos procesas išreiškiamas lygtimi:

$$\frac{\partial C}{\partial t} = \frac{1}{r^2} \frac{\partial}{\partial r} \left(r^2 D(r) \frac{\partial C}{\partial r} \right), \quad 0 < t \leq T, \quad 0 < r < R, \quad (\text{S.19})$$

kur $D(r)$ yra funkcija, rodanti difuzijos koeficientą:

$$D(r) = \begin{cases} D_{cell}, & \text{jei } r \in \text{ląstelių sluoksniui,} \\ D_{matrix}, & \text{jei } r \in \text{tarpląsteliniam sluoksniui.} \end{cases}$$

Formulėse D_{cell} yra difuzijos koeficientas ląstelėse, o D_{matrix} yra difuzijos koeficientas tarpląstelinėje medžiagoje, $d_{cell} = 12 \mu\text{m}$ yra vidutinis ląstelių skersmuo. d_m yra vidutinis atstumas tarp ląstelių, apskaičiuotas taip, kad žinomas ląstelių skaičius N tilptų į R spindulio sferoidą. Pradinės-kraštinės sąlygos tokios pačios kaip R6G modelyje (S.18).

Koeficientų skaičiavimas ir skaitinis sprendimas

R6G dažai sklinda per ląsteles difuzijos greičiu D_{cell} ir per tarpląstelinę medžiagą greičiu D_{matrix} . R6G modelio (S.17) difuzijos koeficientas buvo apskaičiuotas visoje sferoje vidurkinant pagal formulę $D = \phi D_{cell} + (1 - \phi) D_{matrix}$, kur ϕ yra bendro ląstelių tūrio ir rutulio tūrio santykis. Ląstelėms buvo pasirinktas *stratum corneum* (išorinio odos sluoksnio) ląstelių difuzijos koeficientas $D_{cell} = 3 \cdot 10^{-13} \text{ m}^2/\text{s}$ [6], nes jos labiausiai primena naudojamas ląsteles eksperimente. Difuzijos koeficientas tarpląstelinėje medžiagoje D_{matrix} buvo gautas priderinant eksperimentinius duomenis prie R6G modelio duomenų. WGA dažų difuzijos koeficientui apskaičiuoti buvo naudojamas porėtos terpės modelis [141].

Palyginimui su eksperimentiniais duomenimis buvo apskaičiuota sukauptinė koncentracija C_{acc} į tūrio vienetą, t. y. bendra koncentracija sferoje padalyta iš jos tūrio:

$$C_{acc}(t) = \frac{4\pi}{V_{sphere}} \int_0^R C(t, r) r^2 dr. \quad (\text{S.20})$$

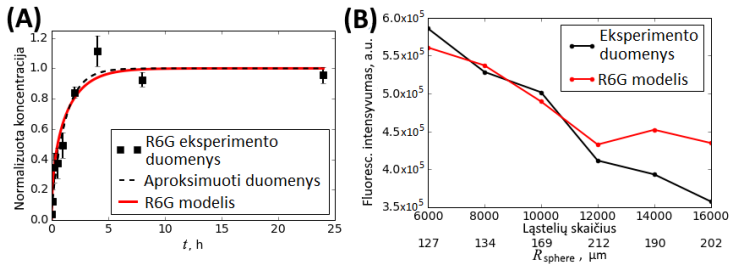
Pateiktos lygtys (S.14)–(S.19) buvo išspręstos skaitiniu būdu. Pirmiausia buvo pasirinkta 2D diskretus tinklelis, susidedantis iš 100 taškų r kryptimi ir 240 000 taškų t kryptimi. Toks didelis taškų skaičius buvo būtinas, nes modeliavimo laikas $T = 24 \text{ h}$ buvo ilgas ir reikėjo pasiekti aukštą tikslumą. Naudojant baigtinių skirtumo metodą Kranko-Nikolsono neišreikštinį algoritmą buvo išvestos skirtuminės lygtys [116], kurios buvo linearizuotos Pikardo iteraciniu metodu. Kiekvienoje iteracijoje gauta tiesinių lygčių sistema buvo sprendžiama naudojant Tomaso algoritmą. Procesas greitai konvergavo į apytikslį sprendinį ir nereikėjo daugiau nei 4 iteracijų.

Reikalingi integralai, tokie kaip (S.20), diskrečiame tinklelyje buvo apskaičiuoti pagal 1 eilės Niutono-Koteso formulę. Visi algoritmai buvo įgyvendinti Python programavimo kalba.

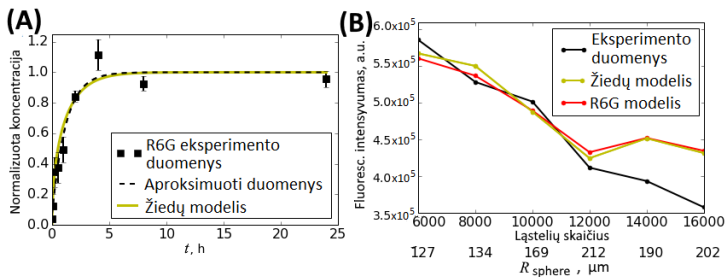
S.3.3 Modeliavimo rezultatai

Difuzijos koeficientas tarpląstelinėje medžiagoje buvo apskaičiuotas pritaikant modelio duomenis prie fizinio eksperimento duomenų mažiausių kvadratų metodu. Sukaupta R6G koncentracija, apskaičiuota

naudojant modelį (S.17)–(S.18) bei integralą (S.20), ir fluorescencijos intensyvumas iš eksperimento duomenų buvo normalizuoti į bedimensinius dydžius, kad juos būtų galima palyginti. Tiesinė priklausomybė tarp fluorescencijos intensyvumo ir šaltinio koncentracijos yra gerai žinoma, todėl prietaiso konstantą galima apskaičiuoti normalizuojant, t. y., padalijant iš maksimalios koncentracijos ir fluorescencijos intensyvumo. Nustatyta, kad $D_{matrix} = 4,2 \cdot 10^{-13} \text{ m}^2/\text{s}$ labiausiai atitinka eksperimento duomenis (S.9A pav.), o prietaiso konstanta šiam eksperimentui yra $6,4 \cdot 10^{10}$.



S.9 pav.: (A) R6G modelio dažų patekimo kreivė (raudona linija) priderinta prie eksperimento duomenų (punktyrinė linija) difuzijos koeficientui tarpląstelinėje medžiagoje rasti; (B) Sukauptas fluorescencijos intensyvumas palygintas su eksperimento duomenų intensyvumu.



S.10 pav.: (A) Dažų prasiskverbimas į sferoidą pagal laiką žiedų modelio ir eksperimento duomenims. Difuzijos koeficientas – iš R6G modelio. (B) Sukauptas fluorescencijos intensyvumas pagal žiedų modelio duomenis, R6G modelį ir eksperimentą.

R6G modelio patvirtinimui buvo naudojamas kitas eksperimento duomenų rinkinys. Sferoidams su skirtingais spinduliais ir ląstelių skaičiumi buvo apskaičiuotas fluorescencijos intensyvumas per 2 valandas (S.9B pav.). Sukauptos R6G koncentracijos buvo padaugintos iš prietaiso konstantos ir nubraižytos palyginimui su eksperimentiniais duomenimis. Vienai ląstelei apskaičiuotas intensyvumas mažėja dides-

niems sferoidams, ko ir buvo tikimasi, nes dažams vis sunkiau pasiekti vidinius sluoksnius. Buvo stebimas labai glaudus eksperimento ir modelio atitikimas, išskyrus didžiausio ląstelių skaičiaus sferoidus. Tai aiškinama taip: ląstelių sferoido dydis priklauso nuo pradinio ląstelių skaičiaus, kol pasiekiamas kritinis ląstelių kiekis. Pastebėta, kad auginant sferoidus nuo 6000 iki 10 000 ląstelių, rutulio dydis padidėjo tiesiškai, tačiau sferoidai su dideliu ląstelių skaičiumi ($N_{cell} = 14\,000$ ir $N_{cell} = 16\,000$) buvo panašaus dydžio, t. y. jų spindulys nepriklausė nuo ląstelių skaičiaus. Taigi, mūsų modelis parodė, kad sferoidai nuo 6000 iki 10 000 ląstelių yra tinkami dažų įsiskverbimo tyrimams, tačiau didesnių sferoidų negalima naudoti dėl netikslumų.

Siekiant geriau suprasti R6G įsiskverbimą į sferoidus buvo pasiūlytas alternatyvus žiedų modelis. Prasiskverbimo į sferoidą kreivė **S.10A** pav. buvo apskaičiuota naudojant R6G ląstelių ir tarpląstelinės medžiagos difuzijos koeficientus iš anksčiau analizuoto R6G modelio. Kreivė labai artima aproksimuotiems eksperimentiniams duomenims, vidutinė kvadratinė paklaida yra tik 0,04 %. Palyginimui, prasiskverbimo kreivės, apskaičiuotos naudojant R6G modelį (**S.9A** pav.), paklaida yra 0,05 %. Žiedų modelio fluorescencijos intensyvumo grafikas buvo nubraižytas (**S.10B** pav.) pagal eksperimentinius ir R6G modelio duomenis. Nors abu modeliai gana gerai atitinka eksperimento duomenimis, žiedų modelis yra šiek tiek tikslesnis su 4,9 % paklaida palyginti su 5,2 % R6G modeliu. Iš šių rezultatų darome išvadą, kad abu modeliai yra sėkmingi ir gali būti naudojami tolesnei dažų įsiskverbimo analizei.

S.3.4 Išvados

Abu R6G dažų modelio atvejai, t. y. tiesinės difuzijos modelis ir žiedų modelis, parodė gerą atitikimą eksperimento rezultatams. Naudojant R6G modelį buvo apskaičiuota, kad difuzijos koeficientas tarpląstelinėje medžiagoje yra $D = 4,2 \cdot 10^{-13} \text{ m}^2/\text{s}$, o tai yra maždaug 4 kartus daugiau nei difuzijos koeficientas ląstelėse. Buvo išanalizuota kaupimosi dinamika ir parodyta, kad nusistovėjimui pasiekti reikia maždaug 4 h, tačiau centrinė zona nėra pilnai inkubuojama iki maždaug 10 h. Ši dinamika taip pat priklauso nuo rutulio dydžio ir tankio.

Naudojant WGA modelį buvo ištirtas prisikabinimo greičio ir prisikabinimo vietų skaičiaus poveikis WGA-Alexa488 dažų skverbimosi dinamikai. Modeliavimo rezultatai parodė, kad WGA-Alexa488 dažų kaupimasis ląstelėse yra netiesinis. Tai galima paaiškinti tokiais biologiniais veiksniais kaip endocitozės (medžiagos pernešimas į ląstelę per

pūslelę membranoje) dažnis, ląstelių ir tarpląstelinė medžiagos tankis, receptorių ląstelių membranoje tipas, jų koncentracija ir kt.

Bendros disertacijos išvados

- Naujas kompiuterinis SECM modelis yra tinkama priemonė tiriant RC-SECM režimą ir nustatant reakcijos bei difuzijos koeficientus. Nustatyta, kad deguonies difuzijos koeficientas yra atvirkščiai proporcingas gliukozės koncentracijai terpėje. Buvo pasiūlyta formulė šiam koeficientui apskaičiuoti dirbant RC-SECM režimu.
- Matematinis modelis, apibūdinantis tris dažniausiai pasitaikančias nestandartines ultramikroelektrodo (UME) geometrijas, yra tinkamas būdas įvertinti paklaidai nuo elektros srovės, matuojamos standartiniu UME. Modeliuojant atrasta, kad išlindęs UME duoda didžiausias matavimo paklaidas, o įtraukto UME ir kūginio UME paklaidos yra apytiksliai 2 kartus mažesnės.
- Naudojant R6G dažų įsisavinimo į ląstelių sferoidus modelį, buvo apskaičiuotas difuzijos koeficientas tarpląstelinėje terpėje ir nustatyta, kad jis yra maždaug 4 kartus didesnis už eksperimente naudojamų ląstelių difuzijos koeficientą.
- Tiriant WGA-Alexa488 dažų modelį buvo parodyta, kad prisikabinimo greitis ir prisikabinimo vietų skaičius daro netiesinę įtaką skverbimosi dinamikai.



Rokas Astrauskas

Curriculum Vitae

ASMENINĖ INFORMACIJA

<i>Gimimo diena</i>	1987 lapkričio 14
<i>El. paštas</i>	rokas.astrauskas@mif.vu.lt
<i>Asm. el. paštas</i>	jaurokas@gmail.com

IŠSILAVINIMAS

Informatikos doktorantūra <i>Vilniaus universitetas</i> Doktorantūros gynimas 2021 m.	2014 – 2018
Matematikos magistras <i>Vilniaus universitetas</i>	2012 – 2014
Finansų ir draudimo matematikos bakalauras <i>Vilniaus universitetas</i>	2006 – 2010
Gimnazija <i>Vilniaus licejus</i>	2002 – 2006

DARBINĖ PATIRTIS

J. asistentas <i>Vilniaus universitetas, Matematikos ir informatikos fakultetas</i> Skaitinių metodų, grafų algoritmų, diskrečiosios matematikos ir kt. paskaitos	2015 – ...
Dėstytojas <i>Vilniaus verslo kolegija</i> Matematikos paskaitos	2016 – 2020
Mokslinė praktika <i>Fizinių ir technologijos mokslų centras, Megasistemų fizikos laboratorija</i> Laimėtas konkursas praktikai juodųjų skylių modeliavimui, vadovas dr. K. Zubovas	2013
Dėstytojas <i>Vilniaus Gedimino technikos universitetas</i> Statistikos su R paskaitos	2011 – 2012

Acknowledgements

I would like to express gratitude to my scientific supervisor Prof. Feliksas Ivanauskas for the support and all scientific and personal advice.

My sincere thanks go to scientific contributors of the research papers including our chemists' team Prof. Arūnas Ramanavičius and Dr. Inga Morkvėnaitė-Vilkončienė, our biophysicists' team Prof. Ričardas Rotomskis, Dr. Vitalijus Karabanovas and Greta Jarockytė. Besides the direct collaborators, I am thankful to many other researchers in the Faculty of Mathematics and Informatics of Vlnius University, who have given valuable scientific advice.

Finally, I am truly grateful for my family: my wife Vilija for continuous support, my father Dr. Arvydas Astrauskas for encouraging my studies in the field of mathematics and all the others.

Rokas Astrauskas
Vilnius
14th October 2021

Publications by the Author

1st publication

**Modelling of scanning electrochemical microscopy
at redox competition mode using diffusion and
reaction equations**

F. Ivanauskas, I. Morkvenaite-Vilkonciene, **R. Astrauskas**, and A.
Ramanavicius

Electrochimica Acta, 222: 347–354, 2016

DOI: 10.1016/j.electacta.2016.10.179

2nd publication

**Mathematical Modelling of the Influence of
Ultra-micro Electrode Geometry on Approach
Curves Registered by Scanning Electrochemical
Microscopy**

R. Astrauskas, F. Ivanauskas, I. Morkvenaite-Vilkonciene, and A.
Ramanavicius

Electroanalysis, 31(11): 2214–2223, 2019

DOI: 10.1002/elan.201900313

Copyright Wiley-VCH GmbH. Reproduced with permission.

3rd publication

Modeling the uptake of fluorescent molecules into 3D cellular spheroids

R. Astrauskas, F. Ivanauskas, G. Jarockytė, V. Karabanovas, and R.
Rotomskis

Nonlinear Analysis: Modelling and Control, 24(5): 838–852, 2019

DOI: 10.15388/NA.2019.5.9

Rokas Astrauskas

Computer Modelling of Reaction-Diffusion Processes
in Scanning Electrochemical Microscopy and in Cell Spheroids

Doctoral Dissertation

Natural Sciences

Informatics (N 009)

Thesis Editor: Zuzana Šiušaitė

Reakcijos-difuzijos procesų kompiuterinis modeliavimas
skenuojančioje mikroskopijoje ir ląstelių sferoiduose

Daktaro disertacija

Gamtos mokslai

Informatika (N 009)

Santraukos redaktorė: Vilija Astrauskienė

Vilnius University Press
9 Saulėtekio Ave., Building III, LT-10222 Vilnius
Email: info@leidykla.vu.lt, www.leidykla.vu.lt
Print run of 20 copies